

PICO: Probe of Inflation and Cosmic Origins

Thematic Area: Space Based Projects

Lead Author: Shaul Hanany (hanany@umn.edu)¹

Authors

Marcelo Alvarez ^{9,16}	Brendan P. Crill ⁶	Eric Hivon ³⁰	Levon Pogosian ⁴⁷
Emmanuel Artis ¹²	Gianfranco De Zotti ³⁵	Renée Hložek ⁴⁰	Clem Pryke ¹
Peter Ashton ^{24,16,9}	Jacques Delabrouille ^{5,12}	Johannes Hubmayr ¹⁹	Giuseppe Puglisi ^{48,49}
Jonathan Aumont ²⁵	Eleonora Di Valentino ³⁶	Bradley R. Johnson ⁴¹	Mathieu Remazeilles ³³
Ragnhild Aurlien ²⁶	Joy Didier ³⁷	William Jones ⁴	Graca Rocha ^{6,8}
Ranajoy Banerji ²⁶	Olivier Doré ^{6,8}	Terry Jones ¹	Marcel Schmittfull ¹⁸
R. Belen Barreiro ²⁷	Hans K. Eriksen ²⁶	Lloyd Knox ²⁰	Douglas Scott ⁵⁰
James G. Bartlett ^{5,6}	Josquin Errard ⁵	Al Kogut ²¹	Peter Shirron ²¹
Soumen Basak ²⁸	Tom Essinger-Hileman ²¹	Marcos López-Caniego ⁴²	Ian Stephens ⁵¹
Nick Battaglia ⁷	Stephen Feeney ¹⁷	Charles Lawrence ⁶	Brian Sutin ⁶
Jamie Bock ^{8,6}	Jeffrey Filippi ³⁸	Alex Lazarian ⁴³	Maurizio Tomasi ⁵²
Kimberly K. Boddy ²	Laura Fissel ¹⁴	Zack Li ⁴	Amy Trangsrud ⁶
Matteo Bonato ²⁹	Raphael Flauger ¹⁵	Mathew Madhavacheril ⁴	Alexander van Engelen ²³
Julian Borrill ^{9,10}	Unni Fuskeland ²⁶	Jean-Baptiste Melin ¹²	Flavien Vansyngel ⁵³
François Bouchet ³⁰	Vera Gluscevic ³⁹	Joel Meyers ⁴⁴	Ingunn K. Wehus ²⁶
François Boulanger ³¹	Krzysztof M. Gorski ⁶	Calum Murray ⁵	Qi Wen ¹
Blakesley Burkhardt ³²	Dan Green ¹⁶	Mattia Negrello ⁴⁵	Siyao Xu ⁴³
Jens Chluba ³³	Shaul Hanany ¹	Giles Novak ⁴⁶	Karl Young ¹
David Chuss ¹¹	Brandon Hensley ⁴	Roger O'Brient ^{6,8}	Andrea Zonca ⁵⁴
Susan E. Clark ^{18,34}	Diego Herranz ²⁷	Christopher Paine ⁶	
Joelle Cooperrider ⁶	J. Colin Hill ^{17,18}	Tim Pearson ⁸	

Endorsers

Maximilian Abitbol	Jeff Booth	Riccardo Gualtieri	Philip Lubin
Zeeshan Ahmed	Sean Bryan	Jon E. Gudmundsson	Juan Macias-Perez
David Alonso	Carlo Burigana	Nikhel Gupta	Nazzareno Mandolesi
Mustafa A. Amin	Giovanni Cabass	Nils Halverson	Enrique Martínez-González
Adam Anderson	Robert Caldwell	Kyle Helson	Carlos Martins
James Annis	John Carlstrom	Sophie Henrot-Versillé	Silvia Masi
Jason Austermann	Xingang Chen	Thiem Hoang	Tomotake Matsumura
Carlo Baccigalupi	Francis-Yan Cyr-Racine	Kevin M. Huffenberger	Darragh McCarthy
Darcy Barron	Paolo de Bernardis	Kent Irwin	P. Daniel Meerburg
Ritoban Basu Thakur	Tijmen de Haan	Marc Kamionkowski	Alessandro Melchiorri
Elia Battistelli	C. Darren Dowell	Reijo Keskitalo	Marius Millea
Daniel Baumann	Cora Dvorkin	Rishi Khatri	Amber Miller
Karim Benabed	Chang Feng	Chang-Goo Kim	Joseph Mohr
Bradford Benson	Ivan Soares Ferreira	Theodore Kisner	Lorenzo Moncelsi
Paolo de Bernardis	Aurelien Fraisse	Arthur Kosowsky	Pavel Motloch
Marco Bersanelli	Andrei V. Frolov	Ely Kovetz	Tony Mroczkowski
Federico Bianchini	Nicholas Galitzki	Kerstin Kunze	Suvodip Mukherjee
Daniel Bilbao-Ahedo	Silvia Galli	Guilaine Lagache	Johanna Nagy
Colin Bischoff	Ken Ganga	Daniel Lenz	Pavel Naselsky
Sebastian Bocquet	Tuhin Ghosh	François Levrier	Federico Nati
J. Richard Bond	Sunil Golwala	Marilena Loverde	

Paolo Natoli	Karwan Rostem	George Stein	Patricio Vielva
Michael Niemack	Anirban Roy	Radek Stompor	Abigail Vieregg
Elena Orlando	Jose-Alberto Rubino-	Rashid Sunyaev	Jan Vrtilek
Bruce Partridge	Martin	Aritoki Suzuki	Benjamin Wallisch
Marco Peloso	Matarrese Sabino	Eric Switzer	Benjamin Wandelt
Francesco Piacentini	Maria Salatino	Andrea Tartari	Gensheng Wang
Michel Piat	Benjamin Saliwanchik	Grant Teply	Scott Watson
Giampaolo Pisano	Neelima Sehgal	Peter Timbie	Edward J. Wollack
Nicolas Ponthieu	Sarah Shandera	Matthieu Tristram	Zhilei Xu
Giuseppe Puglisi	Erik Shirokoff	Caterina Umlit��	Siavash Yasini
Benjamin Racine	An��e Slosar	Rien van de Weygaert	
Christian Reichardt	Tarun Souradeep	Vincent Vennin	
Christophe Ringeval	Suzanne Staggs	Licia Verde	

Affiliations

1. University of Minnesota - Twin Cities.
2. Johns Hopkins University.
3. Carnegie Mellon University.
4. Princeton University.
5. APC, Univ Paris Diderot, CNRS/IN2P3, CEA/Irfu, Obs de Paris, Sorbonne Paris Cit  , France.
6. Jet Propulsion Laboratory, California Institute of Technology.
7. Cornell University.
8. California Institute of Technology.
9. Lawrence Berkeley National Laboratory.
10. Space Sciences Laboratory, University of California, Berkeley.
11. Villanova University.
12. IRFU, CEA, Universit   Paris-Saclay, France.
13. University of Pennsylvania.
14. National Radio Astronomy Observatory.
15. University of California, San Diego.
16. University of California, Berkeley.
17. Center for Computational Astrophysics, Flatiron Institute.
18. Institute for Advanced Study, Princeton.
19. National Institute of Standards and Technology.
20. University of California, Davis.
21. NASA Goddard Space Flight Center.
22. University of Michigan.
23. Canadian Institute for Theoretical Astrophysics, University of Toronto, Canada.
24. Kavli Institute for the Physics and Mathematics of the Universe (WPI).
25. IRAP, Universit   de Toulouse, France.
26. University of Oslo, Norway.
27. Instituto de F  sica de Cantabria (CSIC-Universidad de Cantabria), Spain.
28. School of Physics, Indian Institute of Science Education and Research Thiruvananthapuram, India.
29. INAF-Istituto di Radioastronomia and Italian ALMA Regional Centre, Italy.
30. Institut d'Astrophysique de Paris, CNRS and Sorbonne Universit  , France.
31. Ecole Normale Sup  rieure, Paris, France.
32. Rutgers University.
33. JBCA, University of Manchester.
34. Hubble Fellow
35. INAF-Osservatorio Astronomico di Padova, Italy.
36. University of Manchester.
37. University of Southern California.
38. University of Illinois, Urbana-Champaign.
39. University of Florida.
40. Department of Astronomy & Astrophysics and Dunlap Institute, University of Toronto, Canada.
41. Columbia University.
42. European Space Astronomy Centre.
43. University of Wisconsin - Madison.
44. Southern Methodist University.
45. Cardiff University School of Physics and Astronomy.
46. Northwestern University.
47. Simon Fraser University.
48. Stanford University.
49. Kavli Institute for Particle Astrophysics and Cosmology.
50. University of British Columbia, Canada.
51. Harvard-Smithsonian Center for Astrophysics.
52. Universit   degli studi di Milano.
53. Institut d'Astrophysique Spatiale, CNRS, Univ. Paris-Sud, Universit   Paris-Saclay, France.
54. San Diego Supercomputer Center, University of California, San Diego.

This research was funded by a NASA grant NNX17AK52G to the University of Minnesota / Twin Cities, by the Jet Propulsion Laboratory, California Institute of Technology, under a contract with the National Aeronautics and Space Administration, and by Lockheed Martin Corporation.

Substantial contributions to the development of PICO were volunteered by scientists at many institutions world-wide. They are very gratefully acknowledged.

The information presented about the PICO mission concept is pre-decisional and is provided for planning and discussion purposes only.

The cost information contained in this document is of a budgetary and planning nature and is intended for informational purposes only. It does not constitute a commitment on the part of JPL and/or Caltech.

1 Executive Summary

The Probe of Inflation and Cosmic Origins (PICO, Fig. 1.1) is an imaging polarimeter that will scan the sky for 5 years in 21 frequency bands spread between 21 and 799 GHz. It will produce full-sky surveys of intensity and polarization with a final combined-map noise level equivalent to 3300 *Planck* missions for the baseline required specifications, and according to our current best-estimate would perform as 6400 *Planck* missions. With these capabilities, unmatched by any other existing or proposed platform:

- PICO could determine the energy scale of inflation and give a first, direct probe of quantum gravity by searching for the signal that arises from gravitational waves sourced by inflation and parameterized by the tensor-to-scalar ratio r . The PICO requirement is to reach $r = 5 \times 10^{-4} (5\sigma)$, a level that is 100 times lower than current upper limits, and 5 times lower than limits forecast by any planned experiment. If the signal is not detected, PICO is the only instrument that can exclude at $5\sigma(?)$ models for which the characteristic scale in the potential is the Planck scale, a key threshold in inflation physics.
- The mission will measure the minimum expected sum of the neutrino masses with 4σ confidence, rising to 7σ if the sum is near 0.1 eV. PICO will give two additional independent and equally competitive constraints on the sum of neutrino masses.
- The measurements will either detect or strongly constrain deviations from the standard model of particle physics by counting the number of light particle species N_{eff} in the early universe with $\Delta N_{\text{eff}} < 0.06 (2\sigma)$.
- PICO will elucidate the processes affecting the evolution of cosmic structures by measuring the optical depth to reionization τ with an error $\sigma(\tau) = 0.002$, limited only by the small number of spatial modes available in the largest angular scale CMB polarization.
- Up to its resolution scale of few arcmin, the data will give a map of the projected gravitational potential due to all structures in the Universe with the highest signal-to-noise ratio (SNR) relative to any foreseeable experiment, and it will give a catalog of 150,000 clusters extending to their earliest formation redshift. Each of these datasets will be used in combination with data from LSST and from future optical and infrared surveys to independently constrain the evolution of the amplitude of linear fluctuations $\sigma_8(z)$, with sub-percent accuracy.
- PICO will determine the cosmological paradigm of the 2030s by reducing the allowed volume of uncertainty in a 12-dimensional ΛCDM parameter space by a factor of nearly a billion relative to current *Planck* constraints on only six parameters. Such exquisite scrutiny will either give strong validation or require yet-to-be discovered revisions.
- PICO’s maps of the Milky Way, which will have 3000 times more independent pixels compared to those available from *Planck*, will be used to resolve long-standing questions about our own Galaxy including the composition, temperature, and emissivities of Galactic dust, and the relative roles of gas turbulence and magnetic fields in the dynamics of the Galaxy and in the observed low star-formation efficiency.
- The data will constrain generic models of dark matter; enable a search for primordial magnetic fields with sufficient sensitivity to rule them out as the sole source for the largest observed galactic

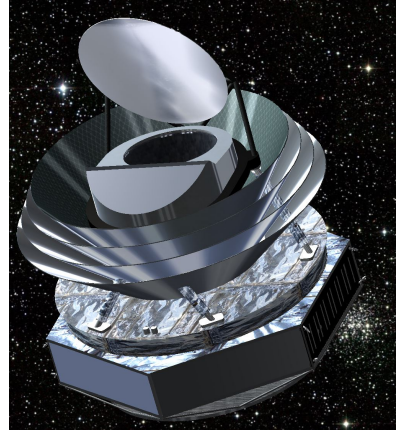


Figure 1.1: The PICO spacecraft

magnetic fields; constrain string theory motivated axions by improving by a factor of 300 constraints on polarization rotation arising from early Universe fields; and will give precise tracing of the evolution with z of thermal pressure in the universe through correlations of the thermal Sunyaev–Zeldovich effect with LSST’s gold sample of galaxies, which will exceed a signal-to-noise ratio of 1000.

PICO will give deep, full-sky legacy maps with which astrophysicists will constrain the early phases of galaxy evolution by discovering 4500 strongly lensed dusty galaxies with z up to 5; investigate the early phases of cluster evolution by discovering 50,000 proto-clusters out to $z \sim 4.5$; perform a census of cold dust in 30,000 low z galaxies; make cosmic infrared background maps of the anisotropies due to dusty star-forming galaxies; and map magnetic fields in 70 nearby galaxies. This rich harvest will be contained in maps of both intensity and polarization at 21 frequency bands, each more sensitive than any planned experiment. Six of the PICO full sky maps in bands between 321 and 800 GHz, are not accessible to ground-based instruments. Only a space mission like PICO will provide such full-sky legacy maps.

With its broad frequency coverage, PICO is better equipped than any other current or planned instrument to separate the detected signals into their original sources of emission. This capability is important for many of the science goals, and is critical for unveiling the faintest of signals, the telltale signature of inflation, which is already known to be dominated by Galactic foregrounds. PICO’s large multiplicity of independent maps and sky surveys, and its stable thermal environment will give control of systematic uncertainties unmatched by, and entirely different from, any other platform. It will conduct observations from L2, and execute ten redundant, full-sky surveys, each complete within 6 months.

The mission has a single instrument that surveys the sky with a repetitive pattern. The telescope is a 1.4 m entrance-aperture, two-reflector system, with passively cooled primary, and 4.5 K actively cooled aperture-stop and secondary. The 0.1 K cooled focal plane is based on technologies that are either already in use by sub-orbital experiments, or are simple extensions to higher or lower frequency bands.

The science PICO will deliver addresses some of the most fundamental quests of human knowl-

Table 1.1: **Mission Parameters**

Combined polarization map depth ^a :	
Baseline	0.87 μK_{CMB} arcmin equivalent to 3300 <i>Planck</i> missions
CBE ^b	0.61 μK_{CMB} arcmin equivalent to 6400 <i>Planck</i> missions
Survey duration / start	5 yrs / 2029
Orbit type	Sun-Earth L2
Launch mass	2147 kg
Total power	1320 W
Data rate	6.1 Tbits/day
Cost	\$ 958M

^a rms noise in 1×1 arcmin² pixel.

^b CBE = Current best estimate.

Table 1.2: **Frequency Bands, Resolution, and Noise Level**

Frequency [GHz]	FWHM [arcmin]	Polarization map depth	
		Baseline [μK_{CMB}] ^a	CBE [μK_{CMB}] ^a
21	38.4	23.9	16.9
25	32.0	18.4	13.0
30	28.3	12.4	8.7
36	23.6	7.9	5.6
43	22.2	7.9	5.6
52	18.4	5.7	4.0
62	12.8	5.4	3.8
75	10.7	4.2	3.0
90	9.5	2.8	2.0
108	7.9	2.3	1.6
129	7.4	2.1	1.5
155	6.2	1.8	1.3
186	4.3	4.0	2.8
223	3.6	4.5	3.2
268	3.2	3.1	2.2
321	2.6	4.2	3.0
385	2.5	4.5	3.2
462	2.1	9.1	6.4
555	1.5	45.8	32.4
666	1.3	177	125
799	1.1	1050	740

^a For units in [Jy/sr] see Hanany et al. [4].

edge. Its science advances will enrich many areas of astrophysics, and will form the basis for the cosmological paradigm of the 2030s and beyond. Many of these advances can only be achieved by a space-based mission. The design of PICO is informed by science breakthroughs made by *Planck* and sub-orbital experiments over the last decade. Further breakthroughs with CMB science require a scale-up that in terms of science per dollar invested is most optimally achieved by PICO. The mission relies on today’s technologies; no new fundamental developments are required. PICO is the only single-platform instrument with the combination of sensitivity, angular resolution, frequency bands, and control of systematic effects that can deliver the compelling, timely, and broad science. We recommend a start for the mission in the next decade.

2 Key Science Goals and Objectives

2.1 Gravitational Waves and Inflation

Measurements of the cosmic microwave background (CMB) BB angular power spectrum are the only foreseeable way to detect inflationary gravitational waves. The strength of the signal, quantified by the tensor-to-scalar ratio r , is a direct measure of the expansion rate of the Universe during inflation, and together with the Friedmann equation, it reveals the energy scale of inflation. A detection of r “would be a watershed discovery”, a quote from the 2010 decadal panel report [2].

PICO will detect primordial gravitational waves if inflation occurred at an energy scale of at least 5×10^{15} GeV, or equivalently $r = 5 \times 10^{-4} (5\sigma)$ (Fig. ??). A detection will provide evidence for a new energy scale tantalizingly close to the energy scale associated with grand unified theories, probe physics at energies far beyond the reach of terrestrial colliders, and be the first observation of a phenomenon associated with quantum gravity [3].

There are only two classes of slow-roll inflation in agreement with current data that naturally explain the observed value of the spectral index of primordial fluctuations n_s [4]. The first class is characterized by potentials of the form $V(\phi) \propto \phi^p$. The second class is characterized by potentials that approach a constant as a function of field value, either like a power law or exponentially. All models in this class, with a characteristic scale in the potential that is larger than the Planck scale, predict a tensor-to-scalar ratio of $r \gtrsim 0.001$.

With its strong constraints on r , the strongest anticipated among any proposed next decade experiment, PICO will either detect gravitational waves from either of these classes with high confidence, or it will be the only experiment to answer the challenge articulated by the recent ‘Inflationary Gravitational Waves’ community science paper: “If these thresholds are passed without a detection, most textbook models of inflation will be ruled out; and, while the possibility of an early inflationary phase would still remain viable, the data would then force a significant change in our understanding of the primordial Universe.” [?].

The BB angular power spectrum measured by PICO will have contributions from Galactic sources of emission and ‘lensing’ B -modes, created by gravitational lensing of E -modes as the CMB photons traverse the gravitational potentials throughout the Universe (Fig. ?? and § 2.3.2). In case of an r detection, there will be two additional features due to the inflationary signal. One is the ‘recombination peak’ at $\ell = 80$ and the other is the ‘reionization peak’ at multipoles of $\ell \lesssim 10$.

Uncertainty in the characterization of Galactic foregrounds already limits our ability to constrain r . These foregrounds are anticipated to be nearly 1000 times stronger than next-decade-targeted inflationary B -mode signals at $\ell = 8$. ‘Lensing’ B -modes, created by gravitational lensing of E -modes as the CMB photons traverse the gravitational potentials throughout the Universe, are

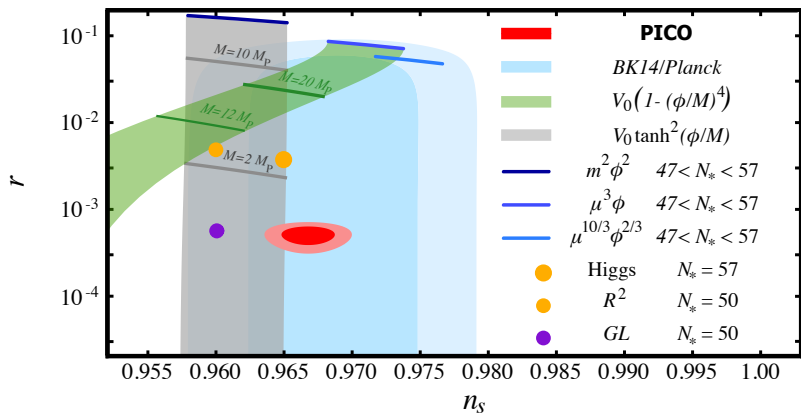


Figure 2.1: Current 1σ and 2σ limits on r and n_s (cyan) and forecasted constraints for a fiducial model with $r = 0.0005$ for PICO, together with predictions for selected models of inflation. Characteristic super-Planckian scales in the potentials are marked with darker lines. GL is the Goncharev-Linde model (see text).

an effective foreground for the inflationary BB signal at $\ell = 80$. PICO has the angular resolution to remove 73% of the lensing B -mode power, assuming strong foregrounds, and the frequency coverage to remove foregrounds to levels below the B -mode reionization peak; see Section ???. If an inflationary B -mode signal is detected, it is important to characterize its entire ℓ dependence in the predicted reionization and recombination peaks, in order to confirm – rather than assume – its expected dependence on angular scale. Furthermore, the PICO full-sky coverage will enable detection of the recombination peak in several independent patches of the sky, giving an important systematic cross-check. Only PICO can provide these important benefits.

The simplest models of inflation, in which there is a single inflaton field, predict primordial fluctuations that are very nearly Gaussian with $|f_{NL}^{\text{local}}| < 1$, where f_{NL}^{local} is a parameter quantifying the level of local non-Gaussianity [5]. A detection of $|f_{NL}^{\text{local}}| > 1$ points exclusively to models of inflation with multiple fields (Fig. ??). For $f_{NL}^{\text{local}} = 2$, 3σ evidence will be reached through correlations between the PICO lensing potential maps (§ 2.3.2) and LSST galaxies. If LSST’s auto-correlation can only be used on smaller angular scales $L \geq 20$, the 3σ evidence weakens to 2σ .

2.2 Fundamental Particles and Fields

- **Light Relics** The ‘effective number of light relic particle species’ N_{eff} gives information about particle species that are predicted to have existed in the early Universe in extensions of the Standard Model of particle physics. The canonical value with three neutrino families is $N_{\text{eff}} = 3.046$. Additional light particles contribute a change ΔN_{eff} that is a function only of the decoupling temperature of the additional species and the spin of the particle g . The PICO baseline will provide a constraint $\Delta N_{\text{eff}} < 0.06$ (95%) and will either detect new particle species, or constrain the lowest temperature T_F at which any vector particle (spin 1) could have fallen out of equilibrium to a factor of 400 higher than today’s constraint (Fig. 2.2, right).

- **Neutrino Mass** The origin and structure of the neutrino masses is one of the great outstanding questions about the nature of the Standard Model particles. Cosmology offers a measurement of the sum of the neutrino masses $\sum m_\nu$ through the gravitational influence of the non-relativistic cosmic neutrinos, specifically the suppression of power on small spatial scales, which PICO will measure via CMB lensing (§ 2.3.2).

All cosmological measurements of $\sum m_\nu$ require three ingredients: the amplitude of the primordial fluctuation power spectrum A_s , the optical depth to reionization τ , and a measure of the growth of structure. PICO is the only next-decade instrument that will self consistently provide two of the

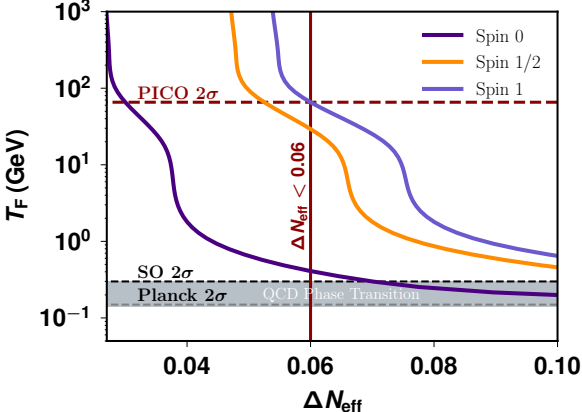


Figure 2.2: PICO will achieve a constraint $\Delta N_{\text{eff}} < 0.06$ (95%) (left, 2σ contours shown) in the baseline configuration (cross) using its cosmic-variance-limited measurement of EE for $\ell \leq 2300$, and 21 frequency bands to utilize data over 70% of the sky ($5'$ resolution assumed). This constraint translates to moving up the lowest decoupling temperature T_F for particles with spin 1, 1/2, and 0 by factors of 400, 200, and 6, respectively, relative to *Planck* (right, dashed black, only T_F for vector particles is shown). We also show the projected vector particle limit for the Simons Observatory [6].

ingredients: τ , and the growth of structure through its CMB lensing data. In combination with A_s coming from DESI or EUCLID, PICO will give $\sigma(\sum m_\nu) = 14$ meV, detecting the minimum sum of 58 meV at the 4σ level. As described later PICO will measure $\sum m_\nu$ in two additional ways, which will give equivalent constraints.

- **Dark Matter** Cosmological measurements have already confirmed the existence of one relic that lies beyond the Standard Model: dark matter. CMB experiments are effective in constraining dark matter candidates in the lower mass range, which is not available for terrestrial direct detection experiments [7–12].

PICO’s constraining power comes from making high SNR maps of the lensing-induced deflections of polarized photons, and cosmic-variance limited determinations of the TT , TE and EE spectra up to $\ell \simeq 2500$. For a spin-independent velocity-independent contact-interaction between dark matter and protons, chosen as our fiducial model, PICO will improve upon *Planck*’s dark matter cross-section constraints by a factor of 25 over a broad range of candidate dark matter masses that are largely unavailable for traditional direct detection experiments. If 2% of the total dark content is made of axions, PICO’s measurement of the TT , TE and EE spectra with additional constraints from the lensing reconstruction will detect this species at between 7 and 13σ , depending on the mass range. This is an average improvement of a factor of 10 relative to *Planck*.

- **Primordial Magnetic Fields** One of the long-standing puzzles in astrophysics is the origin of observed $1\text{--}10 \mu\text{G}$ galactic magnetic fields [13]. Producing such fields through a dynamo mechanism requires a primordial seed field [14]. Moreover, μG -strength fields have been observed in proto-galaxies that are too young to have gone through the number of revolutions necessary for the dynamo to work [15]. A primordial magnetic field (PMF), present at the time of galaxy formation, could provide the seed or even eliminate the need for the dynamo altogether. Specifically, a 0.1 nG field in the intergalactic plasma would be adiabatically compressed in the collapse to form a $\sim 1 \mu\text{G}$ galactic field [16]. PMFs could have been generated in the aftermath of phase transitions in the early Universe [17], during inflation [18, 19], or at the end of inflation [20]. A detection of PMFs with the CMB would be a major discovery because it would establish the magnetic field’s primordial origin, signal new physics beyond standard models of particle physics and cosmology,

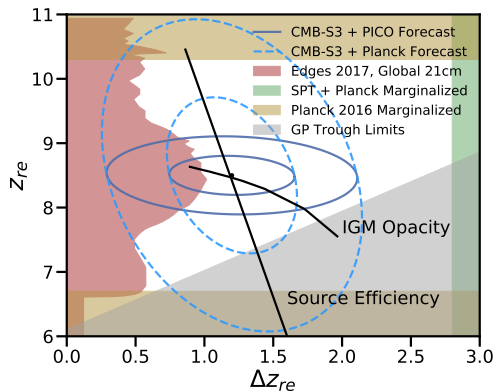


Figure 2.3: Contours of 1σ and 2σ constraints on the mean redshift and duration of reionization using PICO and CMB-S3 data (solid dark blue), and comparison with *Planck* and CMB-S3 (dash light blue). Source efficiency and IGM opacity (dark lines) are two physical parameters controlling the reionization process in current models. The PICO measurements, together with higher-resolution data of the kSZ effect, will significantly constrain the range of models allowed. Shaded regions show already existing constraints from EDGES, *Planck* + the South Pole Telescope, *Planck*, and Gunn–Peterson (GP) trough measurements [47–50].

and discriminate among different theories of the early Universe [21–23].

Using Faraday rotation measurements, PICO will probe PMFs as weak as 0.1 nG (1σ), a precision that already includes the effects of imperfect lensing subtraction, Galactic foregrounds [29–31], and other systematic effects. With this precision, which is a factor of five stronger than achievable with S3 experiments, PICO can conclusively rule out the purely primordial (i.e., no-dynamo driven) origin of the largest galactic magnetic fields.

- **Cosmic Birefringence** A number of well-motivated extensions of the Standard Model involve fields with parity-violating coupling [32–34, 34–37]. Their presence may cause cosmic birefringence – a rotation of the polarization of an electromagnetic wave as it propagates across cosmological distances [34, 38, 39]. Cosmic birefringence converts primordial E -modes into B -modes, producing TB and EB cross-correlations whose magnitude depends on the statistical properties of the rotation field in the sky [40–42]. Using the combination of five bands in the 70–156 GHz range, PICO will reduce the 95% CL bound on uniform rotation angle by a factor of 300 to $0.1'$; The 95% CL bound on the amplitude of a scale-invariant rotation spectrum will be reduced by a factor of 275 to $4 \times 10^{-4} \text{ deg}^2$. These will give constraints on extensions of the Standard Model and on string-theory-motivated axions [44, 46].

2.3 Cosmic Structure Formation and Evolution

2.3.1 The Formation of the First Luminous Sources

A few hundred million years after the Big Bang, the neutral hydrogen gas permeating the Universe was reionized by photons emitted by the first luminous sources to have formed. The nature of these sources and the exact history of this epoch are key missing links in our understanding of structure formation (SO5).

The reionization of the Universe imprints multiple signals in the temperature and polarization of the CMB. In polarization, the most important signature is an enhancement in the EE power spectrum at large angular scales $\ell \lesssim 10$ (Fig. ??). This signal gives a direct measurement of the optical depth to the reionization epoch τ and thus to the mean redshift of reionization z_{re} , with very little degeneracy with other cosmological parameters (Fig. 2.3).¹ *Planck*'s determination of the optical depth to reionization $\tau = 0.054 \pm 0.007 (1\sigma)$ has indicated that reionization concluded by $z \sim 6$, but the measurement uncertainty leaves many unanswered questions including: were the ionizing sources primarily star-forming galaxies or more exotic sources such as supermassive black holes or annihilating dark matter? What was the mean free path of ionizing photons

¹The mean redshift to reionization is defined to be the redshift when 50% of the cosmic volume was reionized.

during this epoch? What was the efficiency with which such photons were produced by ionizing sources? Did the reionization epoch extend to $z \sim 15\text{--}20$, as has been claimed recently [51]? With ten independent maps of the entire sky, multiple frequency bands and ample sensitivity to remove foregrounds, PICO is uniquely suited to make the low- ℓ EE -spectrum measurements and reach cosmic-variance-limited precision with $\sigma(\tau) = 0.002$, settling some of these questions and significantly constraining the others (SO5).

Figure 2.3 presents forecasts for reionization constraints in the $z_{\text{re}} - \Delta z_{\text{re}}$ parameter space. These are obtained from PICO’s measurement of τ in combination with S3 experiments’ measurements of the “patchy” kinematic Sunyaev–Zeldovich (kSZ) effect, due to the peculiar velocities of free-electron bubbles around ionizing sources [52]. The figure includes curves of constant efficiency of production of ionizing photons in the sources and of intergalactic-medium opacity, two parameters that quantify models of reionization. The curves shown are illustrative; families of models, that would be represented by parallel ‘source efficiency’ and ‘IGM Opacity’ lines, are allowed by current data. PICO’s data will give simultaneous constraints on these physical parameters, yielding important information on the nature of the first luminous sources. For example, models in which the first sources are quasars rather than galaxies have significantly different IGM opacities and source efficiencies.

The process of reionization leaves specific non-Gaussian signatures in the CMB. In particular, patchy reionization induces non-trivial 4-point functions in both temperature and polarization [53, 54]. The temperature 4-point function can be used to separate reionization and late-time kSZ contributions. Combinations of temperature and polarization data can be used to build quadratic estimators for reconstruction of the patchy τ field, analogous to CMB lensing reconstruction (§ 2.3.2). These estimators generally require high angular resolution, but also rely on foreground-cleaned CMB maps. Data from PICO’s high-frequency bands – which have better than 2 arcmin resolution and cover frequencies that are not optimal for observations from the ground – will enable these estimators to be robustly applied to high-resolution ground-based CMB data, a strong example of ground-space complementarity.

Decreasing the uncertainty on τ is important to break the degeneracy between this parameter and the amplitude of the primordial power spectrum A_s , a degeneracy in the CMB power spectra that hinders all cosmological observables of the growth of structure (§ 2.2). The degeneracy can only be broken through measurements of the low- ℓ EE power spectrum. PICO’s cosmic-variance-limited polarization measurements will thus improve constraints on the sum of neutrino masses, dark energy, and modified gravity coming from all low- z growth measurements, including galaxy lensing, velocity-field measurements, redshift-space distortions, and galaxy surveys.

2.3.2 Probing the Evolution of Structures via Gravitational Lensing and Cluster Counts

The particle content of the Universe, gravitational collapse, the effects of dark energy, and baryonic feedback processes that recycle energy determine the evolution of structures in the Universe. The amplitude of linear fluctuations as a function of redshift, parameterized by $\sigma_8(z)$, is thus a sensitive probe that embodies the effects of physical processes affecting growth. CMB photons are affected by, and thus probe, $\sigma_8(z)$ as they traverse the entire Universe. PICO will tightly constrain $\sigma_8(z)$ through measurements of gravitational lensing and cluster counts.

- **Gravitational Lensing** Matter between us and the last-scattering surface deflects the path of photons through gravitational lensing, imprinting the three-dimensional matter distribution across

the volume of the Universe onto the CMB maps. The specific quantity being mapped by the data is the projected gravitational potential ϕ that is lensing the photons. From the lensing map, which receives contributions from all redshifts between us and the CMB, with the peak of the distribution at $z \sim 2$, we infer the angular power spectrum $C_L^{\phi\phi}$ (Fig. 2.4). Both the temperature and polarization maps of the CMB, and by extension the angular power spectra, are affected by lensing.

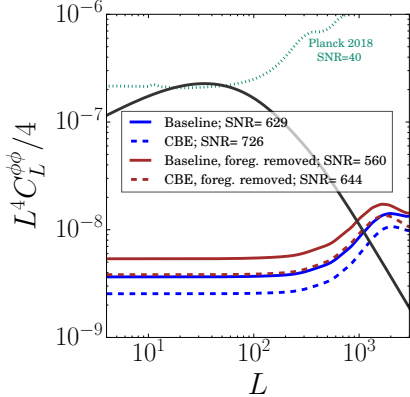


Figure 2.4: PICO will make a high SNR full-sky map of the projected gravitational potential ϕ due to all matter between us and the last scattering surface at all angular scales $2 \leq L \lesssim 1000$ (Footnote ??) for which its noise (red and blue) is below the theoretically predicted power spectrum $C_L^{\phi\phi}$ (black). Noise predictions as a function of L and anticipated SNR values for the measurement of $C_L^{\phi\phi}$ are given for the baseline (solid) and CBE (dashed) cases, both without (blue) and with (red) a process of foreground separation that degrades the SNR by $\sim 10\%$. In all cases the SNR is more than a factor 10 higher than currently available with *Planck*.

Planck's ϕ map had SNR of ~ 1 per L mode over a narrow range of scales, $30 < L < 50$. PICO will make a true map, with $\text{SNR} \gg 1$ for each mode in the range $2 \leq L \lesssim 1000$. While *Planck* had an SNR of 40 integrated across the entire $C_L^{\phi\phi}$ power spectrum [55], PICO will give SNR of 560 and 644 for the baseline and CBE configurations, respectively; both values already account for foreground separation (Fig. 2.4).

PICO's ϕ map is a key ingredient in the delensing process that improves constraints on r (§ 2.1) and in extracting neutrino mass constraints (§ 2.2). It will also be used to constrain the properties of quasars and other high-redshift astrophysical tracers of structure. For example, cross-correlations with quasar samples from DESI will yield a precise determination of the quasar bias (and hence host halo mass) as a function of the quasar properties, such as (non-)obscuration. Such studies are not possible with any other lensing techniques, due to their sensitivity to lower redshifts.

• **$\sigma_8(z)$ from Gravitational Lensing** Cross-correlations between the PICO lensing-potential map and wide-field samples of galaxies and quasars provide a powerful technique to measure the time dependence of the amplitude of matter fluctuations $\sigma_8(z)$ in tomographic redshift bins. This is achieved by overcoming the limitations of auto-correlations of these data sets. The lensing ϕ map is sensitive to the projection of all matter back to the last-scattering surface, so it cannot resolve the time dependence of fluctuations, while galaxies and quasars trace matter in an unknown biased way so that the matter amplitude cannot be determined. Cross-correlations of the two data sets, broken down to several tomographic redshift bins, will constrain how galaxies in each bin trace the dark matter, which will yield strong constraints on $\sigma_8(z)$ and thereby on structure growth and models of dark energy and modified gravity [56, 57].

In the left panel of Fig. 2.5 we show projected 1σ errors on $\sigma_8(z)$ when using cross-correlations with LSST's gold sample of galaxies [58]. Sub-percent accuracy is obtainable with PICO's resolution, which will give information extending to $L = 1000$.² This accuracy will be used to constrain dark energy or modified gravity, in the context of specific models, and to give a neutrino mass

²PICO's resolution is sufficient to give information for $L > 1000$, but at these scales structures are non-linear and will not be used to constrain $\sigma_8(z)$.

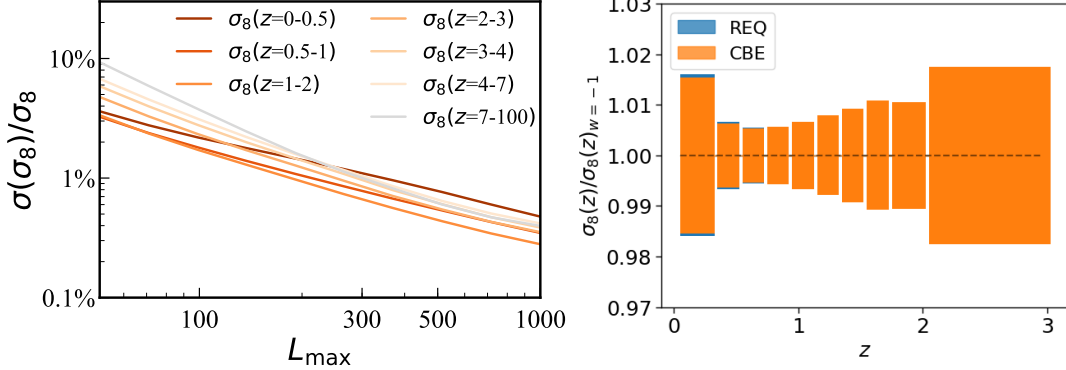


Figure 2.5: Sub-percent constraints on the evolution of σ_8 as a function of redshift will come from two independent PICO products: correlations between PICO’s deep gravitational lensing map (Fig. 2.4) and LSST’s gold sample of galaxies (left) and cluster counts (right). Fractional uncertainties in σ_8 relative to fiducial Λ CDM values are given as a function of the finest angular scale L_{\max} of the correlation analysis for seven redshift bins (left). The baseline and CBE configurations give essentially the same fractional errors of $\sigma_8(z)$ using cluster counts (right). For LSST we assume: 10 years, 50% sky fraction, 55 galaxies per arcmin² at redshift $z < 3$ with magnitude limit $i < 25.3$ [58], and dropout galaxies at $z > 3$ [60] extrapolating recent Hyper Suprime-Cam observations [61–63], with linear bias $b(z) = 1 + z$.

constraint that is independent from and competitive with that inferred from the CMB lensing auto-power spectrum (§ 2.2) [59].

- **Cluster Counts** The distribution of galaxy clusters over redshift is one consequence of the evolution of structures and is thus a sensitive measure of $\sigma_8(z)$. The observational quantity of interest is $dN/(dz dm)$, the number of observed clusters per redshift and per mean mass interval, from which constraints on $\sigma_8(z)$ can be derived. Galaxy clusters found by PICO via the thermal Sunyaev–Zeldovich (tSZ) effect (§ 2.3.3) provide a catalog with a selection function that is simple to model and thus straightforward to use for cosmological inference. PICO’s catalog will provide clusters with masses above $\sim 2 \times 10^{14} M_\odot$ out to redshifts $z \sim 3$. We forecast that PICO will find $\sim 150,000$ galaxy clusters, assuming the cosmological parameters from *Planck* and using the 70% of sky not obscured by the Milky Way. Information provided by the high frequency bands will mitigate the potential reduction in detection efficiency due to dust emission by cluster members [64], an advantage of space-based observations. Redshifts will be provided by future optical and infrared surveys, while cluster masses will be inferred by optical weak lensing for clusters with $z < 1.5$ and by PICO’s own CMB halo lensing data at higher redshifts (see next paragraph). This catalog will provide σ_8 with sub-percent precision for $0.5 < z < 2$ (Fig. 2.5, right), and a neutrino mass constraint $\sigma(\sum m_\nu) = 14$ meV that is independent from the one coming from the CMB lensing measurements (SO3, § 2.2). A significant fraction of the PICO-detected clusters will also be detected by eROSITA, giving an exceptional catalog of multi-wavelength observations for detailed studies of cluster astrophysics.

Calibrating the masses of clusters, i.e. determining $m(z)$, is the most uncertain step in inferring σ_8 and other cosmological parameters using cluster counts. PICO will provide calibration using “CMB halo lensing”, an approach that uses the small-scale effects of gravitational lensing due to dark matter halos around clusters and proto-clusters [65–67]. The technique is particularly effective for measuring halo masses out to high redshifts where gravitational lensing of background objects no longer works because there are no background sources. The approach is illustrated in Fig. 2.6, which gives the 1σ uncertainty in a halo mass measurement as a function of the object’s redshift. PICO will measure the mass of individual low-mass clusters ($\sim 10^{14} M_\odot$) over a wide

redshift range, and by stacking will determine the mean mass of smaller halos, with masses of $\sim 10^{13} M_{\odot}$, which include those hosting individual galaxies. Because the vast majority of clusters have masses that are larger than $\sim 10^{14} M_{\odot}$, the PICO data will provide mass calibration for all objects of interest. The flattening at high redshift reflects the fact that the technique is sensitive over a broad range of redshifts. The high-frequency PICO data, for which the resolution matches that of ground-based instruments at lower frequencies, will play an essential role in cleaning foregrounds, particularly those derived from the temperature-based estimator, which is most contaminated by foregrounds.

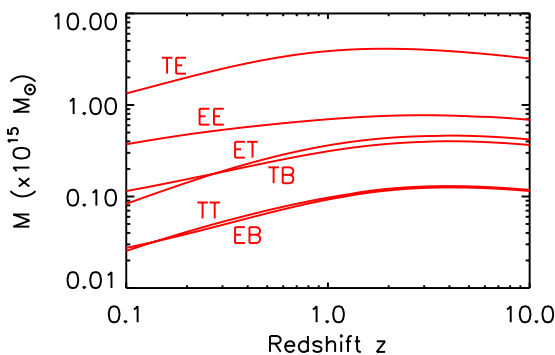


Figure 2.6: PICO will provide mass calibration for individual clusters and proto-clusters with mass as low as $10^{14} M_{\odot}$ at $z > 2$ using ‘halo lensing’. Curves for different CMB signal correlations (red) give the 1σ sensitivity of an optimal mass filter [68] as a function of z . The curves are flat at high redshift, demonstrating that the technique probes a broad range of redshifts. For PICO, the EB and TT estimators are equivalent, offering important cross-validation of measurements because the systematics are very different for temperature and polarization.

Beyond its role in calibrating masses for cluster counts, PICO’s halo lensing measurements will also be a unique tool for measuring the relation between galaxies and their dark matter halos during the key epoch of cosmic star formation at $z \geq 2$, which is not reachable by other means. This will provide valuable insight into the role of environment on galaxy formation during the rise to and fall from the peak of cosmic star formation at $z \sim 2$.

2.3.3 Constraining Feedback Processes through the Sunyaev–Zeldovich Effect

Not all CMB photons propagate through the Universe freely; about 6% are Thomson-scattered by free electrons in the intergalactic medium (IGM) and intercluster medium (ICM). These scattering events leave a measurable imprint on CMB temperature fluctuations, which thereby contain a wealth of information about the growth of structures and the thermodynamic history of baryons. A fraction of these photons are responsible for the thermal and kinetic Sunyaev–Zeldovich effects (tSZ and kSZ) [69, 70]. The amplitudes of the tSZ and kSZ signals are proportional to the integrated electron pressure and momentum along the line of sight, respectively. They thus contain information about the thermodynamic properties of the IGM and ICM, which are highly sensitive to astrophysical feedback. Feedback is the process of energy injection into the IGM and ICM from accreting supermassive black holes, supernovae, stellar winds, and other sources. Feedback processes are the most uncertain, yet crucial, ingredient in modern theories of galaxy formation; they are required in order to match observations of the stellar properties of galaxies, but the underlying details of the physical processes involved are still highly uncertain.

Multifrequency CMB data also allow the reconstruction of full-sky “Compton- y maps” of the tSZ signal. With low noise and broad frequency coverage, which is essential for separating out other signals, PICO will yield a definitive Compton- y map over the full sky, with a total SNR of 1270 for the CBE and 10% lower for the baseline configurations (Fig. 2.7). This is nearly two orders of magnitude higher SNR than *Planck*, which already gave data with much higher SNR than ground-based experiments. The tens of thousands of clusters forecast to be detected by PICO will be found in this y map (§ 2.3.2).

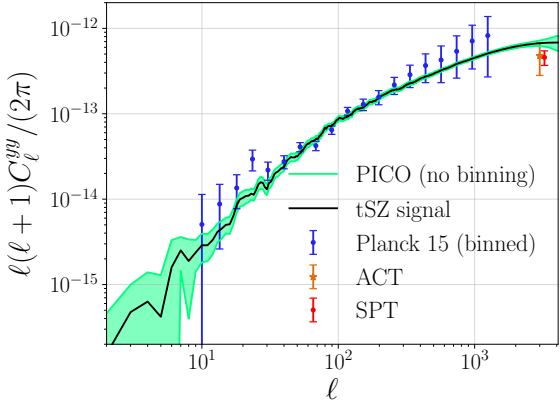


Figure 2.7: The PICO y -map will give a tSZ power spectrum with an SNR of 1270 (green, 1σ per ℓ mode), which is nearly 100 times larger than from *Planck* (blue). Binning the data (not shown), as was done for *Planck* would further increase the SNR. We also show current measurements by the ground-based SPT and ACT [71, 72]. In these forecasts we reconstruct the Compton- y field from maps that include Galactic foregrounds, CMB fluctuations, and PICO CBE noise using the needlet internal linear combination algorithm [73]. The input maps use the *Planck* sky model [74].

Strong constraints on models of astrophysical feedback will be obtained from the analysis of the PICO y -map, both from its auto-power spectrum and from cross-correlations with galaxy, group, cluster, and quasar samples. As an example, we forecast the detection of cross-correlations between the PICO y -map and galaxy weak-lensing maps constructed from LSST and WFIRST data. Considering the LSST gold weak-lensing sample, with a source density of 26 galaxies/arcmin² covering 40% of the sky, we forecast a detection of the tSZ–weak-lensing cross-correlation with SNR = 3000. Cross-correlations with the galaxies themselves will be measured at even higher SNR. At this immense significance, the signal can be broken down into dozens of tomographic redshift bins, precisely tracing the evolution of thermal pressure over cosmic time. For PICO and WFIRST (assuming 45 galaxies/arcmin² covering 5.3% of the sky), we forecast SNR = 1100 for the tSZ-weak lensing cross-correlation. The WFIRST galaxy sample extends to higher redshift, and thus this high-SNR measurement will allow the evolution of the thermal gas pressure to be probed to $z \approx 2$ (the peak of the cosmic star formation history) and beyond. These measurements will revolutionize our understanding of galaxy formation and evolution by distinguishing between models of feedback energy injection at high significance. Additional cross-correlations of the PICO y -map with quasar samples, filament catalogs, and other large-scale structure tracers will provide valuable information on baryonic physics that is complementary to inferences from the lensing cross-correlations described earlier.

2.4 Testing Λ CDM

The current cosmological model, as encoded by Λ CDM, provides a good fit to most current data. A host of cosmological observations including the CMB fit within the model that consists of only six parameters [75]. But the model is phenomenological and it leaves fundamental questions open. Premier among them is the unknown content of the majority of the Universe. Approximately 95% of the Universe appears to be composed of dark matter and dark energy of unknown nature, both of which are necessary to explain observations at scales ranging from that of a galaxy to that of the Hubble volume. Yet, there are no detection of dark matter particles, and as for dark energy, it even lacks a compelling theoretical motivation.

In this context, tension between measurements of any Λ CDM parameter obtained by different probes compel additional stringent tests and investigation of alternatives to the prevailing paradigm. Examples of emerging tensions are: the 3.6σ discrepancy between the CMB- and local-Universe-anchored supernovae-based measurements of the Hubble constant [4, 76]; the identification of lack of correlations at large angles in the TT power spectrum that has an apparent probability of less than 10^{-3} of occurrence in standard Λ CDM [77]; and the $\sim 2\sigma$ tension in

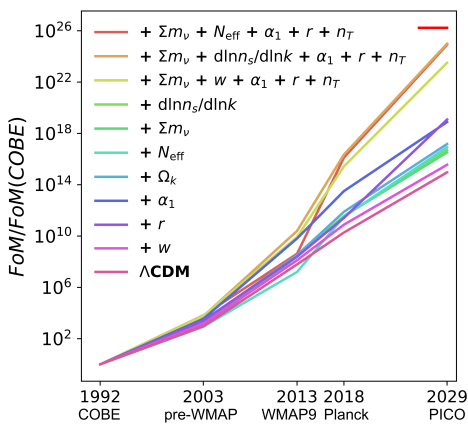


Figure 2.8: The increase in the FOM using data from CMB experiments since *COBE* for the ΛCDM six-parameter model (dark purple) and when adding other cosmological parameters. Increase in value represents increase in information content. PICO data will continue the average trend (blue line, $\Lambda\text{CDM} + \alpha_1$) of doubling the FOM every 10 months since 1992. For an 11-parameter set that includes N_{eff} (red increasing line) PICO will improve the FOM by a factor of 0.5×10^9 relative to *Planck*, and will extract nearly the same information as that attainable by a mission with double the resolution and nine times lower baseline noise (top right red horizontal bar). The 11-parameter set includes: w -dark energy; r -the tensor to scalar ratio; α_1 -amplitude of correlated CDM isocurvature perturbations; Ω_k -curvature; N_{eff} -effective number of light relics; Σm_ν -sum of neutrino masses; and $d\ln n_s/d\ln k$ -running of the spectral index.

measurements of the amplitude of late time perturbations σ_8 between the *Planck* CMB *TT*, *TE*, and *EE* power spectra and those from cosmic shear surveys [78–81]. A similar level of tension for σ_8 ($\sim 2\sigma$) arises when comparing *Planck* CMB spectra and cluster counts from *Planck* and other surveys [82, 83]. Such tensions, while perhaps only indicating the presence of systematic effects in the measurements, may in fact point toward new physics. One way to search for new physics is to better constrain the current measurements and the known extensions beyond the base six-parameter set.

Given an experiment’s baseline noise and angular resolution, and an input set of N parameters, it is straightforward to calculate the uncertainty with which it will constrain the set [84]. A figure of merit (FOM) that quantifies the strength of the constraint is the volume of the uncertainty region in the N -dimensional parameter space. We use the same analytical approach and FOM that have also been used in other studies [84–87].³ This FOM is defined such that a larger value linearly corresponds to *smaller* volume and thus to smaller parameter errors.

Fig. 2.8 shows the increase in the FOM since *COBE* for the six-parameter ΛCDM model, as well as for additional cosmological parameters.⁴ The Figure only includes data from CMB experiments. The FOM for ΛCDM improved by a factor of 100 between *WMAP* and *Planck*, and will further improve by a factor of 10^5 with PICO. For the 11-parameter set that includes N_{eff} shown in the Figure PICO will improve upon *Planck* by a factor of 0.5×10^9 . Having achieved this improvement, there would be only little information left to extract with this parameter set even by a mission with double the resolution and nearly ten times lower noise (Fig. 2.8). Even stronger FOM improvements are obtained when a 12-parameter set is considered [88], and when the PICO CMB data will be combined with data sets available in the next decade, including weak lensing, BAO, and cluster of galaxies.

These improvements will test ΛCDM so stringently that it is hard to imagine it surviving such a scrutiny if it is not fundamentally correct. If tensions deepen to become discrepancies, it would

³The FOM is determined by the covariance of the Fisher information matrix, $\text{FOM} = (\det[\text{cov}(p_i)])^{-1/2}$, $i = 1, \dots, N$, where p is the parameter set.

⁴The six-parameter ΛCDM model includes: the baryon density; the dark matter density; the amplitude and spectral index of a power-law spectrum of initial perturbations; the angular scale of acoustic oscillations; and the optical depth to reionization.

be even more exciting if a new cosmological model emerged.

2.5 Galactic Structure and Star Formation

Planck enabled an immense step forward in Galactic astrophysics [89]. With seven full-sky polarization maps at frequencies between 30 and 353 GHz and a highest resolution of $5'$, *Planck* provided entirely new and surprising data about the structure of the interstellar medium (ISM); the data have a lasting legacy for the foreseeable future. PICO will provide an even greater leap forward. It will produce 21 polarization maps of Galactic emission, and in the bands already probed by *Planck* they will be much deeper; for example, PICO’s map at 321 GHz will be 105 times deeper than *Planck*’s mean map depth at 353 GHz, and PICO’s map at 30 GHz will be 17 times deeper than *Planck*’s. At 799 GHz PICO will have five times the resolution of *Planck*’s highest resolution map (Fig. 2.9). Such a data set can only be obtained from space. These data will complement a rich array of other polarization observations forthcoming in the next decade, including stellar polarization surveys to be combined with Gaia astrometry, and Faraday rotation measurements from observations at radio wavelengths with the Square Kilometer Array (SKA) and its precursors.

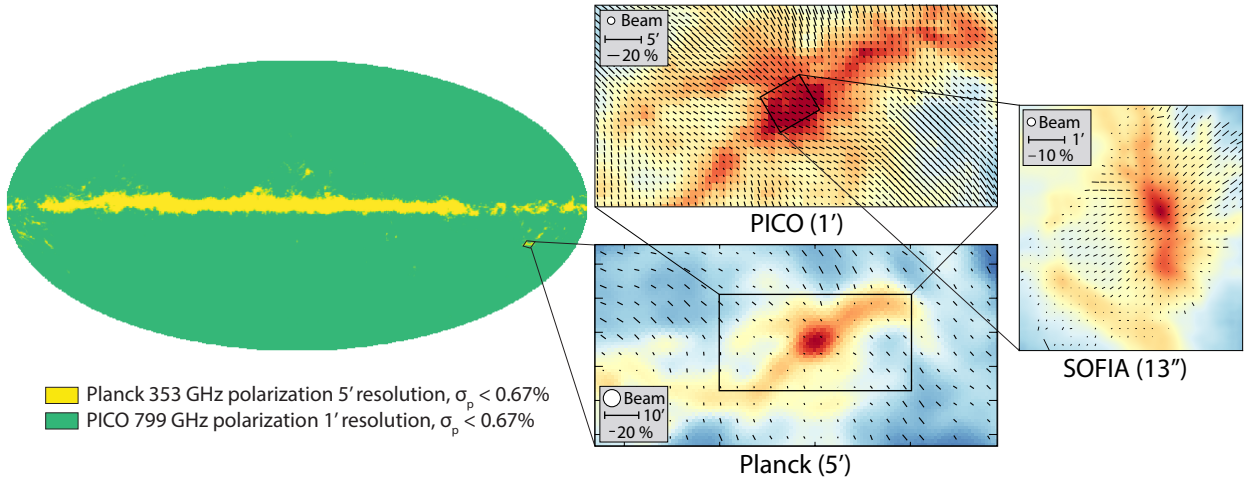


Figure 2.9: *Planck*’s 353 GHz polarization map gave a resolution of $5'$ and sensitivity to polarization intensity of $\sigma_p < 0.67\%$ over a small portion of the sky (left, yellow). At 799 GHz, the PICO baseline mission will give a polarization map of the *entire* sky and with 5 times higher resolution (left, green). In the middle panels, the *Planck* map of the Orion region overlaid with vectors that are aligned with the inferred magnetic field (lower panel), and a simulated PICO observation (upper panel) illustrate the leap in information content (vector lengths are proportional to polarization fraction). With this map, and maps at other frequencies, PICO will characterize Galactic magnetized turbulence at scales spanning the diffuse ISM down to dense star-forming cores, which will be mapped with high-resolution polarimetry by instruments such as HAWC+/SOFIA [90] (right panel) and ALMA [91].

While the PICO data will likely provide many new insights and surprises, we focus here on two particularly important science objectives that are integral to NASA’s science goal to explore how the Universe evolved; they relate to the structure and evolution of the Milky Way. These science objectives can only be achieved using the PICO dataset.

(1) *Test models of the composition of interstellar dust:* Less than $1\text{ }\mu\text{m}$ in size, dust grains are intermediate in the evolution from atoms and molecules to large solid bodies such as comets, asteroids, and planets. Encoded in the composition of dust are the pathways through which grains formed and grew. Dust grains also participate directly in interstellar chemistry, for example by catalyzing the formation of H_2 and organic molecules on their surfaces, in ways that depend upon

their chemical makeup. Thus, the composition of dust grains is an essential aspect of the chemical evolution of interstellar matter, from the formation of complex molecules in space to the growth of planets. Through vastly improved spectral characterization of Galactic polarization, the PICO data will discriminate among models of Galactic dust composition to elucidate the chemical evolution of the Galaxy (SO6, § 2.5.1). The data will also guide the construction of methods for separating diffuse dust emission from cosmological signals of interest, particularly the inflationary signal.

(2) *Determine how magnetic fields affect molecular cloud and star formation:* Stars are formed through interactions between gravitational and magnetic fields, turbulence, and gas over more than four orders of magnitude of spatial scales, which span the diffuse ISM (kpc scale), molecular clouds (10 pc), and molecular cloud cores (0.1 pc). However, the role magnetic fields play in the large-scale structure of the diffuse ISM and in the observed low star-formation efficiency has been elusive, owing to the dearth of data. By virtue of the strong dynamical coupling of dust and gas and the systematic alignment of dust grains with magnetic fields, PICO’s dust polarization measurements will for the first time probe the large-scale Galactic magnetic field with enough resolution to trace the role of magnetic fields through the entirety of the star-formation process (SO7, § 2.5.2).

2.5.1 Test Models of the Composition of Interstellar Dust

Strong extinction features at $9.7\text{ }\mu\text{m}$ and $18\text{ }\mu\text{m}$ indicate that much of interstellar dust is in the form of amorphous silicates, while features at 217.5 nm , $3.3\text{ }\mu\text{m}$, and $3.4\text{ }\mu\text{m}$ attest to abundant hydrocarbons. It is unknown, however, whether the silicate and carbonaceous materials coexist on the same grains or whether grains of each composition grow through distinct, parallel pathways dictated by their surface chemistry.

Some data suggest that the populations are distinct. Spectropolarimetry of dust extinction reveals robust polarization in the $9.7\text{ }\mu\text{m}$ silicate feature [92], indicating that the silicate grains are aligned with the local magnetic field. In contrast, searches for polarization in the $3.4\text{ }\mu\text{m}$ carbonaceous feature have yielded only upper limits, even along sightlines where silicate polarization is observed [93, 94]. These data are consistent with silicate and carbonaceous materials existing on separate grains with different alignment properties.

At odds with the spectropolarimetric evidence from dust extinction are current measurements of the polarization fraction of the far-infrared dust emission with *Planck* [95] and BLASTPol [96]. They show little to no frequency dependence, whereas substantial frequency dependence would be expected if two components with distinct polarization properties were contributing to the total emission.

With excellent polarization sensitivity, even in diffuse regions, PICO will provide a definitive test of the two-component paradigm [97]. In this case, the PICO baseline mission will determine the intrinsic polarization fractions of each of the two components to a precision of 3%. With this level of precision the data will validate or reject state-of-the-art dust models [e.g. 98, 99], test for the presence of additional grain species with distinct polarization signatures, such as magnetic nanoparticles [100], and will be used as a crucial input for the foreground separation necessary to extract cosmological *E*- and *B*-mode science.

Anomalous microwave emission (AME) is a component of Galactic emission peaking in the 20–30 GHz range that has been tentatively identified with small, rapidly-spinning dust grains [101]. As only upper limits have been placed on its polarization, its role as a foreground for cosmological *B*-mode science remains unclear; even small levels of polarization could prove challenging for

determining r (§ 2.7). PICO will finely sample the AME SED with its bands at 21, 25, 30, 36, and 43 GHz. Combined with ground-based maps at lower frequencies, for example C-BASS at 5 GHz [102], PICO will be used to efficiently separate the AME from synchrotron and free-free emission and either detect or place stringent upper limits on its polarization. Further, the enhanced frequency coverage will allow changes in the AME SED with interstellar environment to be characterized and thus elucidate its underlying physics.

2.5.2 Determine How Magnetic Fields Affect Molecular Cloud and Star Formation

Stars form out of dense, gravitationally unstable regions within molecular gas clouds, which themselves form through the flow of diffuse, atomic-phase gas to denser regions. Magnetic fields play an important role throughout this process.

On the largest scales, magnetized turbulence mediates the flow of the gaseous ISM from the atomic to the denser, molecular phase. Recent observations suggest that the structure of the diffuse medium is highly anisotropic, and strongly coupled to the local magnetic field [103–106]. As molecular gas clouds collapse to form stars, magnetic fields can slow the process of star formation by inhibiting movement of gas in the direction perpendicular to the field lines. Observations to date suggest that the outer envelopes of clouds can be supported against gravity by magnetic fields and turbulence, but in dense cores gravity tends to dominate, and so these dense structures can collapse to form stars [107]. The degree to which magnetic fields affect the formation of molecular clouds, as well as stars within these clouds, is poorly constrained, in large part due to the difficulty of making detailed maps of magnetic fields in the ISM.

- **Formation of Magnetized Molecular Clouds from the Diffuse Interstellar Medium** A comprehensive understanding of the magnetized diffuse ISM is challenging because of its diverse composition, its sheer expanse, and the multi-scale nature of the physics that shapes it. To understand how matter and energy are exchanged between the diffuse and dense media, it is essential to measure the properties of the magnetic field over more than four orders of magnitude in column density. PICO is unique in its ability to provide the necessary data. *Planck* achieved measurements of the diffuse sky at 60' resolution, resulting in $\sim 30,000$ independent measurements of the magnetic field direction. With 1.1' resolution PICO will expand the number of independent polarization measurements to 86,000,000 (Fig. 2.9). The data will thus robustly characterize turbulent properties like the Alfvén Mach number, M_A , across a previously unexplored regime of parameter space.

PICO’s observations will complement recently completed high-dynamic-range neutral hydrogen surveys, such as HI4PI [108] and GALFA-HI [109], as well as planned surveys of interstellar gas, most prominently with the SKA and its pathfinders. One of the open questions in diffuse structure formation is how gas flows within and between phases of the ISM. A planned all-sky absorption line survey with the forthcoming SKA-1 will increase the number of measurements of the ISM gas temperature by several orders of magnitude [110]. Quantitative comparisons of the ISM temperature distribution from SKA-1 and estimates of the magnetic field strength and coherence length scale from PICO will elucidate the role of magnetized turbulence in the flow of matter in the ISM from diffuse regions to regions of denser molecular gas.

- **Formation of Stars within Magnetized Molecular Clouds** The role of the magnetic field in star formation is quantified by the ratio of the energies stored in magnetic and gravitational fields, and the ratio of the energy stored in the magnetic field to that stored in gas turbulence. The first ratio is parameterized through a mass-to-flux ratio μ , and the second through M_A .

With full-sky coverage and a resolution of $1.1'$, PICO will map all the molecular clouds out to a distance of 3.4 kpc with better than 1 pc resolution. Extrapolating from the Bolocam Galactic Plane Survey [BGPS, 111], PICO is expected to make highly detailed magnetic field maps of over 2,000 molecular clouds, with 10^3 – 10^5 independent polarization measurements per cloud. These are the *only foreseeable* measurements that will give μ and M_A over a statistically significant sample of molecular clouds. *Planck*, for example, mapped only ten nearby clouds to a similar level of detail [112]. A large sample of clouds is crucial because: (1) dust polarization observations are sensitive only to the magnetic field projected on the plane of the sky, and therefore polarization maps will look very different for molecular clouds observed at different viewing angles; and (2) the relative importance of the magnetic field will likely be a function of cloud age and mass. By observing thousands of molecular clouds PICO will determine μ and M_A for different sub-classes of cloud age and mass.

2.5.3 Galactic Legacy Science

PICO will also produce legacy datasets that will revolutionize our understanding of how magnetic fields influence physical processes ranging from planet formation to galaxy evolution. For ten clouds closer than 500 pc, PICO will resolve magnetic fields on scales of 0.1 pc. This is the scale of dense cores and filaments for these clouds, and thus the observations will constrain how magnetic fields on these scales influence the formation of cloud cores. Currently no experiment has the sensitivity and resolution to observe both the the large-scale (few parsec) and core-scale magnetic fields. By comparing the orientation of the core-scale magnetic fields with the orientation and sizes of proto-planetary disks, PICO will probe whether magnetic braking influences the growth of such disks [113, 114] and provide complementarity to higher angular resolution instruments such as ALMA and SOFIA [91, 115] (Fig. 2.9).

Key processes in the diffuse ISM, including heat transport, streaming of cosmic rays, and magnetic reconnection depend strongly on the level of the environment’s magnetization [116–118]. PICO will give information about these processes with tens of millions of independent measurements of magnetic field orientation over the entire Galaxy. The measurements will also enable studies of the physical processes that generate magnetic fields through a combination of turbulence and large-scale gas motions [119].

Finally, PICO observations will create detailed magnetic field maps of about 70 nearby galaxies, with 100 or more measurements of magnetic field directions per galaxy. Currently, polarized dust emission has only been observed in M82 and NGC 253 using SOFIA [120]. The PICO observations will determine how interaction between large-scale magnetic fields, turbulence, and feedback from previous generations of star formation affect galaxy evolution and star-formation efficiency.

2.6 Legacy Surveys

PICO was designed to respond to requirements posed by the seven science objectives (SOs) listed in Table ???. It will also generate a rich catalog of hundreds of thousands of new sources, consisting of proto-clusters, strongly lensed galaxies, and polarized radio and dusty galaxies. An abundance of information about galaxy and cluster evolution, dark matter, the physics of jets of active galactic nuclei, and magnetic fields of dusty galaxies will be stored in this catalog (Table 2.1). The catalog will be mined in future years through subsequent analysis and follow-up observations.

Table 2.1: Legacy Surveys

Catalog	Impact	Science
Strongly lensed galaxies	<p>Discover 4500^a strongly lensed and highly magnified dusty galaxies across redshift.</p> <p>Current knowledge: 13 sources confirmed in <i>Planck</i> data; a few hundred candidates in <i>Herschel</i>, SPT and ACT data.</p>	Gain information about the physics governing early, $z \simeq 5$, galaxy evolution, taking advantage of magnification and extra resolution enabled by gravitational lensing; learn about dark matter sub-structure in the lensing galaxies.
Proto-clusters	<p>Discover 50,000^a mm/sub-mm proto-clusters distributed over the sky out to $z \sim 4.5$.</p> <p>Current knowledge: <i>Planck</i> + ACT/SPT data expected to yield a few tens.</p>	Probe the earliest phases of cluster evolution, well beyond the reach of other instruments; test the formation history of the most massive virialized halos; investigate galaxy evolution in dense environments.
Nearby galaxies	<p>Detect 30,000 galaxies at $z \lesssim 0.1$ at frequencies above 300 GHz.</p> <p>Current knowledge: 3400 (280) source candidates in the <i>Planck</i> 857 (353) GHz band.</p>	Using frequencies that match cold (15 – 25 K) dust emission, give its spectral energy distribution as a function of galaxy properties to enable correlations with star-formation activity.
Polarized point sources	<p>Detect 2000^b radio and several thousand dusty galaxies in polarization.</p> <p>Current knowledge: about 200 radio sources up to 100 GHz; one polarization measurement of a dusty galaxy.</p>	Study the physics of jets of extragalactic sources, close to their active nuclei; determine the large-scale structure of magnetic fields in dusty galaxies; determine the importance of polarized sources as a foreground for CMB polarization science.
Cosmic infrared background	<p>Provide eight maps of the anisotropy from dusty star-forming galaxies for frequencies $\nu > 200$ GHz, and with 1' resolution at 800 GHz.</p> <p>Current knowledge: Three <i>Planck</i> (higher noise) maps between 300 and 900 GHz with 5' resolution.</p>	Improve constraints on the parameters describing universal star-formation history. Construct a tracer of large-scale structure for CMB de-lensing. Cross-correlate with galaxy surveys and CMB lensing map.

^a Confusion (not noise) limited

^b Noise and confusion limited

2.6.1 Early Phases of Galaxy Evolution

PICO’s catalog of high- z strongly-lensed galaxies will provide answers to major open issues in galaxy formation and evolution. What are the main physical mechanisms shaping the properties of galaxies [121, 122]: in situ processes, interactions, mergers, or cold flows from the intergalactic medium? And how do feedback processes work? To settle these issues we need direct information on the structure and dynamics of high- z galaxies. But these are compact, with typical sizes of 1–2 kpc [123], corresponding to angular sizes of 0.1–0.2'' at $z \simeq 2$ –3. Thus they are hardly resolved, even by ALMA or by HST. If they *are* resolved, high enough SNRs per resolution element are only achieved for the brightest galaxies, which are probably not representative of the general population.

Strong gravitational lensing provides a solution to these problems. Since lensing conserves the surface brightness, the effective angular size is stretched on average by a factor of $\mu^{1/2}$, where μ is the gravitational magnification, thus substantially increasing the resolving power. A spectacular example is ALMA observations of the *Planck*-discovered, strongly lensed galaxy PLCK_G244.8+54.9 at $z \simeq 3.0$ with $\mu \simeq 30$ [124]. ALMA observations with a 0.1'' resolution reached an astounding spatial resolution of 60 pc, substantially smaller than the size of Milky Way giant molecular clouds. CO spectroscopy of this object, measuring the kinematics of the molecular gas, gave

an uncertainty of $40\text{--}50 \text{ km s}^{-1}$. Such precision allows a high SNR detection of the predicted $\sim 1000 \text{ km s}^{-1}$ outflows capable of sweeping the galaxy clear of gas that would otherwise be available for star formation [125]. In this specific case, there were no clear indications that mergers or cold flows shaped the galaxy, but similar spectroscopy of another strongly lensed galaxy at $z = 5.3$ detected a fast (800 km s^{-1}) molecular outflow due to feedback [126].

PICO will detect thousands of early forming galaxies whose flux densities are boosted by large factors due to strong lensing (Fig. 2.10, right). Currently there are reports of just a few other high- z galaxies that are spatially resolved thanks to gravitational lensing, albeit with less extreme magnifications [127–129]. PICO’s catalog will be transformative as it will probe the spectral energy distribution (SED) of the lensed galaxies at their peaks. Two examples of known sources are shown in the left panel of Figure 2.10. While nearly all ground-based instruments observe at frequencies up to $\nu = 10^{11.45} \text{ Hz}$, PICO’s data will extend to the peak of the SED, up to $\nu = 10^{11.9} \text{ Hz}$.

An extrapolation of the *Herschel* counts to the 70% non-Galactic sky gives a detection of 4,500 strongly-lensed galaxies with a redshift distribution peaking at $2 \lesssim z \lesssim 3$ [130], but extending up to $z > 5$ (Fig. 2.10, left panel). If objects like the $z = 5.2$ strongly lensed galaxy HLS J091828.6+514223 exist at higher redshifts, they will be detectable by PICO out to $z > 10$. At the 600 GHz detection limit, about 25% of all detected extragalactic sources will be strongly lensed; for comparison, at optical/near-IR and radio wavelengths, where intensive searches have been carried out for many years, the yield is only about 0.1%, more than two orders of magnitude lower [131]. To add to the extraordinary sub-mm lensing bonanza, the selection of PICO-detected strongly lensed galaxies will be easy because of their unique sub-mm colors (Fig. 2.10, left), resulting in a selection efficiency close to 100% [132]. The survey will find the brightest objects over the entire sky, maximizing the efficiency of selecting sources for follow-up observations.

The intensive high spectral and spatial resolution follow-up campaign of this large sample will enable a leap forward in our understanding of the processes driving early galaxy evolution and open up other exciting prospects, both on the astrophysical and cosmological sides [e.g., 131].

2.6.2 Early Phases of Cluster Evolution

PICO will open a new window for the investigation of early phases of cluster evolution, when their member galaxies were actively star forming (and dusty), but the hot IGM was not necessarily in place. In this phase, traditional approaches to cluster detection (X-ray and SZ surveys, and searches for galaxy red sequences) work only for the more evolved clusters, which do include a hot IGM; indeed these methods have yielded only a handful of confirmed proto-clusters at $z \gtrsim 1.5$ [137].⁵ *Planck* has demonstrated the power of low-resolution surveys for the study of large-scale structure [138], but its resolution was too poor to detect individual proto-clusters [136]. Studies of the high- z two-point correlation function [136, 139] and *Herschel* images of the few sub-mm bright protoclusters detected so far, at $z \leq 4$ [140–142], all of which will be detected by PICO, indicate sizes of $\simeq 1'$ for the proto-cluster cores, nicely matching the PICO FWHM at the highest frequencies.

PICO will detect 50,000 proto-clusters as peaks in the high-frequency maps, which are not available for ground-based instruments (Table 2.1; blue line in the right-hand panel of Fig. 2.10). The redshift distribution will extend out to $z \sim 4.5$. This catalog will be augmented by 150,000

⁵More high- z proto-clusters have been found by targeting the environment of tracers of very massive halos, such as radio-galaxies, QSOs, and sub-mm galaxies. These searches are, however, obviously biased.

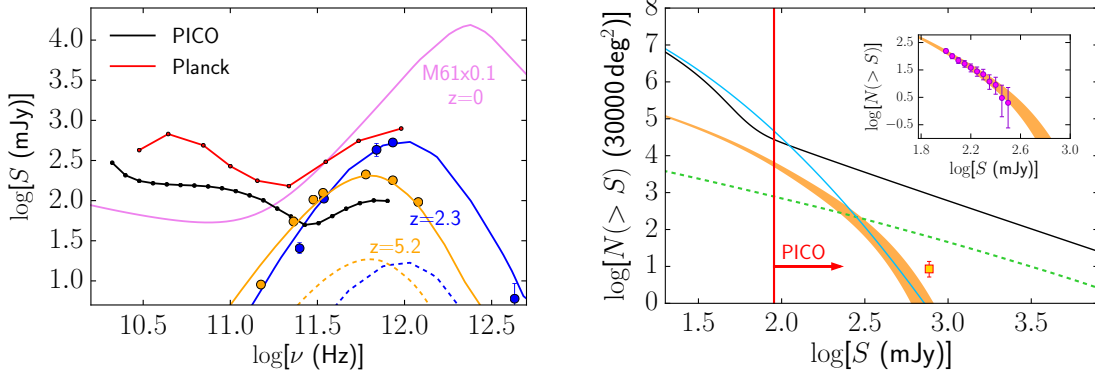


Figure 2.10: **Left:** PICO will detect thousands of new strongly lensed galaxies near the peak of their spectral energy distributions (SEDs), such as SMM J2133–0102 (blue) at $z = 2.3$ [133] and HLS J091828.6+514223 (orange) at $z = 5.2$ [134]. The dashed lines are the SEDs before magnification by lensing. PICO’s higher resolution gives point-source detection limits (black line) that are up to 10 times fainter than *Planck*’s 90% completeness limits (red line [135]). High-frequency measurements ($\nu > 300$ GHz) of 30,000 low- z galaxies, like M61 (magenta, SED was scaled down by a factor of ten), will give a census of their cold dust. **Right:** Integral counts of unlensed (black) and strongly lensed, high- z (orange) star-forming galaxies for 70% of the sky away from the Galactic plane at 600 GHz based on fits of *Herschel* counts over 1000 deg² (inset [130]). The PICO detection region (right of vertical red line) will yield a factor of 1000 increase in strongly lensed galaxies relative to *Planck* (yellow square), as well as about 50,000 proto-clusters (blue) and 2,000 radio sources (green) [136].

evolved clusters, detected by the SZ effect. This will constitute a breakthrough in the observational validation of the formation history of the most massive dark-matter halos, traced by clusters, representing a crucial test of models for structure formation. Follow-up observations will characterize the properties of member galaxies, probing galaxy evolution in dense environments and shedding light on the complex physical processes driving it.

2.6.3 Additional Products of PICO Surveys

PICO will yield a complete census of cold (15–25 K) dust, available to sustain star formation in the nearby Universe, by detecting tens of thousands of galaxies mostly at $z \lesssim 0.1$; the SED of M61 is a typical example (Fig. 2.10, left). With a statistical population, and information only available using data at frequencies above 300 GHz, we will investigate the spectral energy distribution of the dust as a function of galaxy properties, such as morphology and stellar mass.

PICO will increase by an order of magnitude the number of blazars selected at sub-mm wavelengths and will determine the SEDs of many hundreds of them up to 800 GHz and up to $z > 5$. Blazar searches are the most effective way to sample the most massive black holes at high z because of the Doppler boosting of their flux densities. PICO’s surveys of the largely unexplored mm/sub-mm spectral region will also offer the possibility to discover new transient sources or events, such as blazar outbursts [143].

PICO will make a leap forward in the determination of the polarization properties of both radio sources and dusty galaxies over a frequency range where ground-based surveys are impractical or impossible. It will find 1,200 radio sources and 350 dusty galaxies above a flux density limit of 4 mJy at 320 GHz, and 500 radio sources and 15,000 dusty galaxies above 6 mJy at 800 GHz. These data will give information on the structure and ordering of large-scale magnetic fields in dusty galaxies. In the case of radio sources, emission at higher frequencies comes from regions closer to the central engine, providing information on the innermost regions of the jets, close to the active nucleus.

The anisotropy of the cosmic infrared background (CIB), produced by dusty star-forming galaxies over a wide redshift range $0 < z \lesssim 5$, is an excellent probe of the history of star formation across time. The *Planck* collaboration derived values for parameters describing the rate of star formation out to $z \sim 4$ [144–146]. PICO’s lower noise and twice the number of frequency bands will give an order of magnitude improvement on the statistical errors for these parameters [147]. Similar improvement will be achieved in constraining M_{eff} , the galaxy halo mass that is most efficient in producing star-formation activity. PICO’s increased sensitivity to Galactic dust polarization will enhance the separation of signals coming from the largely unpolarized CIB and polarized Galactic dust; an effective separation of signals currently limits making reliable, legacy-quality CIB maps. By providing a nearly full-sky map of matter fluctuations traced by dusty star-forming galaxies, such a set of maps could be used for delensing the CMB [148], for measuring local primordial non-Gaussianity from CIB auto-correlations [149], or for cross-correlations with CMB lensing maps and with galaxy surveys [61].

2.7 Signal Separation

2.7.1 The Signal Separation Challenge

In the PICO frequency range there are Galactic and extragalactic sources of emission. Galactic emissions are due to free-free, synchrotron, and dust, which arise respectively from photon emission in free electron-proton scattering, free electrons spiraling around Galactic magnetic field lines, and from ~ 20 K elongated interstellar dust grains partially aligned with the local magnetic field. Free-free emission is expected to have negligible polarization. The emission from synchrotron and dust are linearly polarized, and has both E and B components (Fig. 2.11). Extragalactic sources of emission include the CMB, which has both E and B modes, and point sources whose polarization level and type are not well constrained. The task of ‘separating the signal to its components’ (sometimes shortened to ‘component separation’) is to decompose the detected signal to its constituent sources. The required precision of signal separation is determined by the requirement to detect or set an upper limit on the inflationary B -mode, which is the faintest among PICO’s targeted signals. In that context, the terms ‘foreground separation’ and ‘foreground cleaning’ are used as equivalents to ‘signal separation’.

Galactic emission dominates the sky’s polarized intensity on large angular scales ($\ell \lesssim 10$), it dominates the cosmological B -modes signals for $\ell \lesssim 150$ for all allowed levels of r , and it is expected to be significant even at $\ell \simeq 1000$, posing challenge for reconstructing the B -mode signal from lensing. This is illustrated in Figs. ?? and 2.11, which show Galactic emission power spectra calculated for the cleanest – that is, the least Galactic-emission-contaminated – 60% of the sky. But even in small patches of the sky, far from the Galactic plane and with the least foreground contamination, Galactic emission levels are substantial relative to an inflationary signal of $r \sim 0.01$ and overwhelm it for $r \lesssim 0.001$ [150]. Separating the cosmological and Galactic emission signals is one of two primary challenges facing any next-decade experiment attempting to reach these levels of constraints on r (the second is control of systematic uncertainties).

Foreground separation is challenging because the spatial power spectra and frequency spectra of the foregrounds are not known to sufficient accuracy anywhere across the sky. To a first approximation, the spectrum of synchrotron emission is a power law $I_{\text{sync}} \propto \nu^\alpha$, with $\alpha \simeq -1$. The spectrum of dust emission is $I_{\text{dust}} \propto \nu^\beta B_\nu(T_{\text{dust}})$, where $\beta \simeq 1.6$, $T_{\text{dust}} \simeq 20$ K, and $B_\nu(T)$ is the Planck function; this is referred to as ‘modified blackbody emission’. If those models exactly reflected

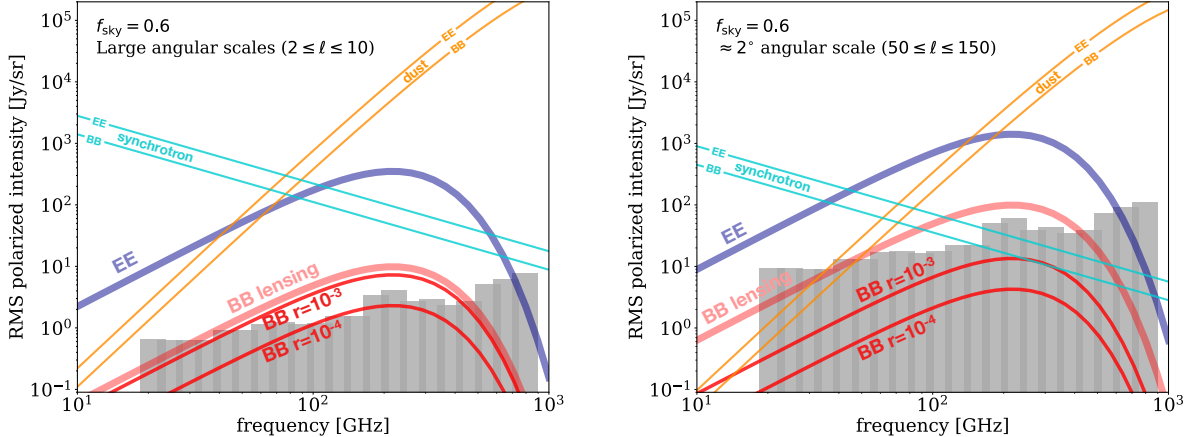


Figure 2.11: Polarization BB spectra of Galactic synchrotron and dust, compared to CMB polarization EE and BB spectra of different origins for two values of r and for two ranges of angular scales: large-scale, $\ell \leq 10$, corresponding to the reionization peak (left panel); and intermediate scales $50 \leq \ell \leq 150$, corresponding to the recombination peak (right panel). Data from *Planck* indicate that for Galactic emission the level of the E -mode is approximately twice that of B [150]. The PICO baseline noise (grey bands) is low compared to the Galactic emission components, and thus they will be measured with high SNR in many frequency bands.

the properties of emitting sources, then in principle an experiment that had six frequency bands could determine the three emission parameters, as well as the three amplitudes for the dust, synchrotron, and CMB components. However, recent observations have shown that neither emission law is universal, that spectral parameters are not necessarily the same for intensity and polarization and that they vary across the sky [151–153], and thus that the analytic forms and parameter values given above are only approximately valid for averages across the sky [154]. Also, while both emission laws are well-motivated phenomenological descriptions, the fundamental physics of emissions from grains of different materials, sizes, and temperatures, and of electrons spiraling around magnetic fields, implies that these laws are expected to be neither exact, nor universal.

At the low levels of r targeted by PICO and by other next-decade experiments, even small inaccuracies in foreground modeling and characterization lead to biases and false detections. Several publications have demonstrated that fitting complicated dust temperature profiles using a simple one- or two-temperature model will bias the fitted CMB signal at levels $\delta r \approx 10^{-3}$, which is significant compared to PICO’s goal [155–159].

Further complicating the foreground-separation challenge is the fact that additional polarized foregrounds may exist. Anomalous microwave emission (AME), dust-correlated emission peaking in intensity near 30 GHz, is an important low-frequency foreground in total intensity. It has been tentatively attributed to small, rapidly-spinning dust grains [160]. Current 1σ upper limits on AME polarization are at the level of 1% [160]. If it is 1% polarized, left uncorrected it would give rise to a bias of $\delta r \simeq 5 \times 10^{-4}$ [161]. Astrophysical emission from CO lines at mm wavelengths is expected to be 0.1–1 % polarized [162, 163]. Extragalactic radio sources show a median polarization of 2% [164–166], and there is significant uncertainty about the polarization of dusty galaxies emitting in the PICO wavebands. Initial quantitative estimates show that ignoring radio sources and dusty galaxies may each lead to a bias $\delta r > 3 \times 10^{-3}$ [164, 167, 168] at low and high frequencies, respectively, and ignoring the $CO J = 1 \rightarrow 0$ line could lead to a bias $\delta r > 2 \times 10^{-3}$ [163] at 115 GHz. These levels are appreciable compared to the goals of PICO and other next-decade

experiments.

2.7.2 Foreground Separation Assessment and Methodology

To investigate the efficacy of PICO in addressing the foreground-separation challenge, we used both an analytic forecast and map-domain simulations.

• **Analytic Forecast** The analytic forecast relies on an established, documented, publicly available, cosmological parameters forecasting code [169]. The code uses *Planck*-reported Galactic emissions; it assumes that the foreground spectral indices are constant across patch sizes of $\sim 15^\circ$ on a side; it employs a parametric maximum-likelihood approach⁶ to remove the foregrounds and to forecast $\sigma(r)$; and it uses the cleanest 60% of the sky. Lensing *B*-modes are included in the input spectra (and are partially removed via delensing, taking into account both noise and foregrounds), but the input for the inflationary signal is $r = 0$.

• **Map-Domain Simulations** Map-domain simulations have become the ‘gold standard’ in the community. In this approach, we simulate sky maps that are constrained by available data, but otherwise have a mixture of foreground properties. We ‘observe’ these maps just like a realistic experiment would do, and then apply foreground separation techniques – both parametric and non-parametric⁷ – to separate the Galactic and CMB emissions.

To test the results we constructed a variety of full-sky models [175]. All the models were broadly consistent with available data and with uncertainties from *WMAP* and *Planck*, but they differed in their degrees of Galactic emission complexity. Models included spectral parameters varying spatially and along the line of sight, anomalous microwave emission up to 2% polarized, dust polarization that rotates slightly as a function of frequency because of projection effects, or dust SEDs that depart from a simple modified blackbody. All the foreground maps were generated at native resolution of 7' pixels [176], with widely-used and thoroughly-tested map-generation codes [74, 177].

For each of the models, we added CMB signals in both intensity and polarization, matching a Λ CDM universe. The input inflationary signal was $r = 0$, i.e., no signal, and the *BB*-lensing matched the level after 85% delensing as forecast for PICO. Each of these sky models had 50 realizations of the PICO noise level. The sky models were analyzed with a variety of foreground separation techniques. Because of limited resources for this study not all models were analyzed with all techniques, and not all realizations were used.

2.7.3 Results and Discussion

When using the PICO baseline noise levels with the analytic forecasts we find that $\sigma(r) = 2 \times 10^{-5}$, a level that is five times lower than required ($\sigma(r) = 1 \times 10^{-4}$, see SO1). We consider this forecast optimistic because it assumes strictly white noise, a specific model for the underlying foregrounds that has only eight parameters⁸ per $15 \times 15 \text{ deg}^2$ pixel, and Gaussian parameter likelihood functions. The foregrounds may be more complex, requiring more parameters (for example, spatially

⁶In a parametric approach, foregrounds are assumed to follow emission laws described by a number of free parameters. Parametric models use the frequency dependence of the data along each line of sight to determine the values of the parameters [170].

⁷Non-parametric techniques rely on the fact that CMB emission is uncorrelated with the foregrounds and thus a correlations analysis within a given spatial/frequency data-cube can be used to separate the two sources of emission [73, 171–174].

⁸Six amplitudes for the *Q* and *U* Stokes parameters of the CMB, dust, and synchrotron emission, and two spectral indices, for dust and synchrotron.

varying temperature for the dust, or more than a single spectral index per source of emission), and may have stronger spatial variations. Additionally, the parameter likelihoods may not be Gaussian.

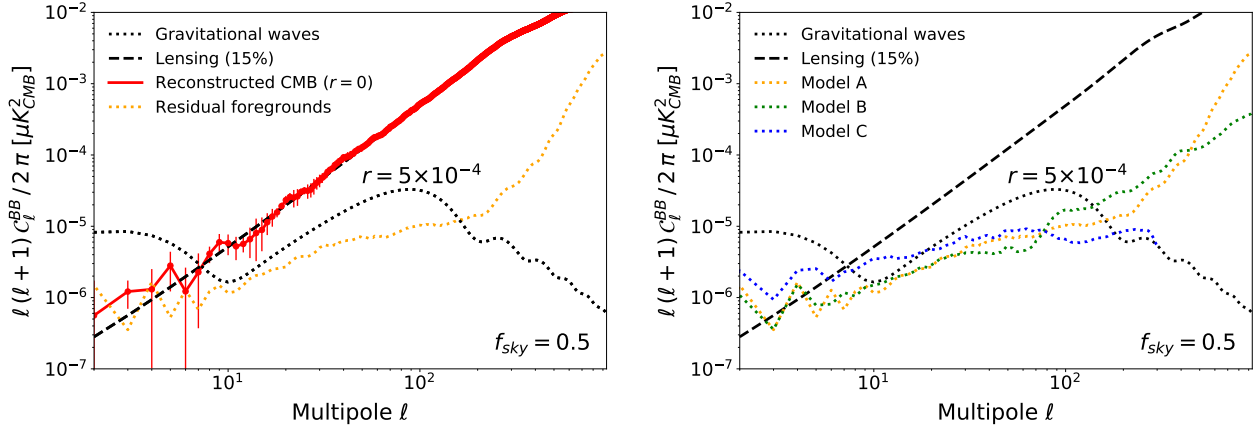


Figure 2.12: Angular power spectra of BB due to the CMB and of residual foregrounds after an end-to-end map-based foreground-separation exercise. The PICO low noise levels and breadth in frequency coverage enable separation of model A foregrounds such that the residual foreground spectrum (left, yellow dotted) is a factor of ten (four) below a BB inflationary signal with $r = 5 \times 10^{-4}$ (black dotted) at $\ell = 5(80)$. Within errors, the recovered CMB (red) matches the input CMB, which consists of only lensing BB (dashed black), over all angular scales $\ell \gtrsim 6$. The results for model B are similar (right, green dots), while model C has somewhat higher residuals at low ℓ . In this exercise we used 50% of the sky. Lower foreground residual levels are obtainable with smaller, cleaner patches of $\sim 5\%$ of sky, which would reduce the residual foregrounds at $\ell \simeq 80$.

The ‘gold-standard’ map-based simulations give initial evidence that the combination of PICO’s sensitivity and broad frequency coverage are effective in foreground removal and that PICO will reach the requirement of $r = 5 \times 10^{-4}$ (5σ). Figure 2.12 shows the results of a foreground-separation exercise over 50% of the sky, with three representative models of Galactic emissions, labeled A, B, and C [175]. This exercise used GNILC, a non-parametric technique⁸ [174], tuned to give low foregrounds on the largest angular scales, that is, the lowest ℓ modes. The input CMB BB signal, consisting of only lensing B -modes, is reconstructed within errors for all $\ell \gtrsim 5$. With models A and B, the residual foreground BB power spectrum, encoding the levels of remaining foreground emission after foreground separation is a factor of ten below an inflationary BB signal for $r = 5 \times 10^{-4}$ at $\ell \simeq 4$. These are the angular scales at which the inflationary signal is stronger than the signal from lensing. Comparing the residual foregrounds for models A and B at this ℓ range to the input BB foregrounds at 155 GHz (for example, Fig. ??) we find a strong suppression (a factor of 1000 in temperature), which is a consequence of PICO’s multiplicity of bands and high sensitivity. The residual in model C is a factor of 2 higher than for A and B at $\ell < 30$. Of all models, this model is least constrained to match existing sky measurements [175].

At intermediate angular scales, $\ell \simeq 80$, the residual foreground is a factor of four lower than the inflationary signal. We expect lower residuals when the GNILC analysis is optimized for this ℓ range. Furthermore, for reconstructing signals at this ℓ range, it is sufficient to analyze data from smaller $\sim 5\%$ regions of the sky. These will have lower mean foreground levels, making the foreground-separation exercise easier, and pushing residuals to levels lower than demonstrated for 50% of the sky. With its full-sky coverage, PICO will have access to several independent 5% sky patches, and will thus make several independent measurements of its r target.

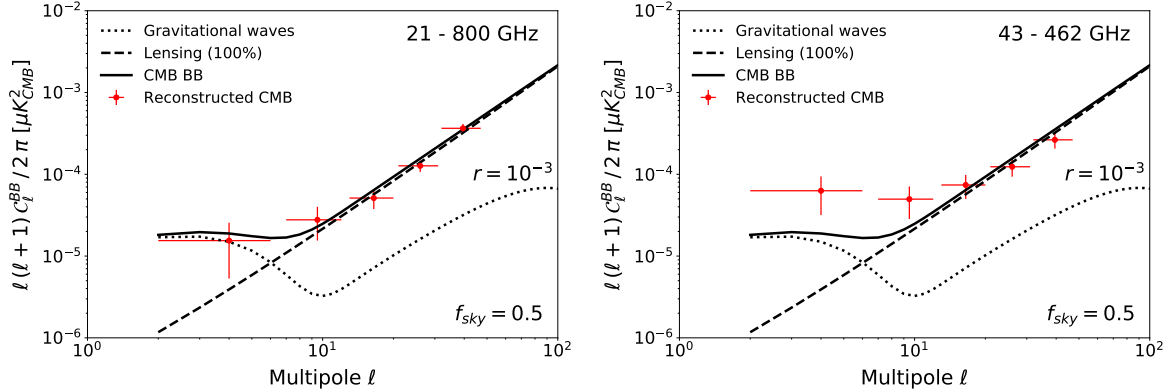


Figure 2.13: **Left:** Foreground separation with all of PICO’s 21 frequency bands recovers the input CMB *BB* power spectrum (solid black) without bias (red). The input CMB spectrum has a contribution from lensing (dashed) and an inflationary signal with $r = 0.001$ (dotted). This exercise uses a parametric approach [170] with foregrounds varying on 4° pixels, and using 50% sky fraction. **Right:** Running the same foreground separation algorithm on the same sky but using only PICO’s bands between 43 and 462 GHz produces an output spectrum (red) that is biased at low multipoles relative to the input. With real data, such a bias would be erroneously interpreted as a higher value of r .

Some of our results validate the need for a broad frequency coverage with a strong lever arm on Galactic emissions outside the primary CMB bands. Figure 2.13 shows that removing several of PICO’s frequency bands, particularly those that monitor dust at high frequencies and synchrotron at low frequencies, can significantly bias the extracted *BB* power spectrum, especially at the lowest multipoles. In this exercise the input CMB contained the lensing signal *and* an inflationary signal with $r = 0.001$, and a parametric technique was used for foreground separation [170, 175].

While these results suggest that PICO’s frequency coverage and sensitivity will be adequate for this level of r , more work should be invested to gain complete confidence. For example, some of the other sky models yield a level of residual foregrounds that would result in biased measurements, reflecting larger values of r ; and some of the foreground-separation techniques appear to give consistently higher foreground residuals than others. To make progress, it is important to continue the simulations and algorithm development program, by: running numerous realizations of different sky models and analyzing them with various approaches; optimizing sky masks; and potentially using a combination of techniques to handle large, intermediate, and small angular scale foregrounds differently. It would also be valuable to continue measurements of Galactic emissions with ground- and balloon-based experiments to further reduce the current level of Galactic emission uncertainties.

2.8 Systematic Uncertainties

Having flown the *WMAP* and *Planck* space missions and fielded numerous sub-orbital experiments to measure polarization, the mm/sub-mm wavelength community has gained extensive experience with systematic uncertainties that occur in various experimental configurations. A rich literature investigates the types of systematic errors due to the environment, the instrumentation, observation strategies, and data analysis that could confound polarization measurements by creating a bias or an increased variance [178–189].

Just as requirements on signal separation are determined by the need to reach the faint inflationary signal, so are the requirements on control of systematic uncertainties. Since an inflationary *BB* power spectrum with $r = 5 \times 10^{-4}$ has a peak signal level of 7 nK, systematic effects need to

be controlled to a level of 1 nK. It has long been recognized that exquisite control of systematic uncertainties will be required from any experiment attempting to reach levels of $r \lesssim 1 \times 10^{-3}$, and it is widely accepted that the stability provided aboard a space platform makes it best suited to control systematic uncertainties compared to other platforms. This is one of the most compelling reasons to observe from space. As *WMAP* and *Planck* demonstrated, an L2 orbit offers excellent thermal stability, as well as flexibility in the choice of scan strategy.

Sources of systematic effects and their ultimate degree of severity are a function of the instrument implementation, the spacecraft scan strategy, and mitigation methods developed during the data analysis phase. Thus, a proper assessment requires end-to-end simulation of the mission. Such a simulation should include realistic non-idealities of the spacecraft, telescope, and instrument, and fold in data post-processing and analysis techniques. Developing such a simulation is a significant undertaking, which took years for the *Planck* mission, and was beyond the scope of this study. We have instead opted to: (1) implement design features within PICO that would provide strong data redundancy and enable cross-checks during the data analysis (§ 2.8.5); and (2) enumerate the sources of possible systematic errors, assess their effects, and investigate three that were deemed the highest priority (§ 2.8.1–§ 2.8.4).

2.8.1 Potential Systematic Effects

The systematic effects faced by PICO can be grouped into three broad categories: (1) coupling between signals; (2) stability; and (3) stray light. For the first category, the most important are the intensity coupling into polarization (both E and B) and E coupling into B . This is because T (denoting intensity) is approximately ten times stronger than E , which is approximately ten times stronger than B . The systematic effects are listed in Table 2.2 and were prioritized for further study using a priority level incorporating a PICO Systematics Working Group’s assessment of how mission-limiting the effect is, how well these effects are understood by the community, and whether mitigation techniques exist.

We used simulations to investigate the following three effects that had the highest priority: error in the absolute calibration of polarization angle; error in the relative calibration between orthogonally oriented detectors; and the effect of the telescope sidelobes. We adapted tools developed for *Planck* [190] and in the context of a European-led mission concept [191]. To understand the severity of the effects, we analyzed each in isolation, and in most cases without complicating effects such as inclusion of foreground-separation steps. More detailed studies of the combination of effects and the inclusion of a foreground-separation step are important but are left to the future.

2.8.2 Absolute Polarization Angle Calibration

In PICO, each of the Stokes Q and U parameters along any line of sight is evaluated through having sensitivity to two orthogonal polarization states. The relative designation of Q and U is derived from having sensitivity to pairs of polarization orientations that are 45° apart (§ 3.2.3). A systematic error in the implementation (or estimation) of these angles by an amount α causes signals in Q and U , and thus in E and B , to mix. Because the CMB E -mode is much larger than B , mixing between E and B leads to the generation of a spurious BB angular power spectrum that mirrors the shape of the EE spectrum (Fig. 2.14). The level of spurious BB is proportional to $\alpha^2 \times EE$. At angular multipoles $\ell \lesssim 100$ a systematic error $\alpha \approx 10'$ will result in a spurious BB level that is approximately equivalent to $r = 1 \times 10^{-4}$ [179, 192]. The mixing of E and B also leads to spurious cross-spectra EB and TB , which respectively mimic the EE and TE spectra.

This systematic error is most usefully split into two contributions: an overall ‘absolute’ error in

Table 2.2: Enumeration of potential systematic errors anticipated in PICO’s measurements, their assessed priority level, their effects on the measurements, and subsections with further discussion for effects with priority level 5.

Name	Priority ^a	Effect ^b	Name	Priority ^a	Effect ^b
Coupling of Signals					
Polarization angle calibration	5	$E \rightarrow B$ § 2.8.2	Gain stability	5	$T \rightarrow P, E \rightarrow B$ § 2.8.3
Bandpass mismatch	4	$T \rightarrow P, E \rightarrow B$	Pointing jitter	3	$T \rightarrow P, E \rightarrow B$
Beam mismatch	4	$T \rightarrow P, E \rightarrow B$	Straylight		
Time response accuracy, stability ...	4	$T \rightarrow P, E \rightarrow B$	Far sidelobes	5	spurious P § 2.8.4
Readout cross-talk	4	spurious P	Other		
Chromatic beam shape	4	spurious P	Residual correlated noise	3	increased
Gain mismatch	3	$T \rightarrow P$	($1/f$, cosmic ray hits)		variance
Cross-polarization	3	$E \rightarrow B$			

^a Level 5 indicates a highly significant, design-driving effect; it may have limited past measurements, or is not well understood. Level 4 is an effect that is either known to be large but is understood reasonably well, or is a smaller effect that requires precise modeling. In Level 3 we expect the effect to be small, but it is not sufficiently well understood and detailed modeling will be done during a Phase A study. Level 2 indicates a well-understood or minimal effect that may not need modeling, and Level 1 is for an effect that is not significant and does not need modeling. ^b $T \rightarrow P$ denotes coupling of the intensity signal (labeled as T to denote temperature) into polarization, which would generally be both E and B . Similar meaning holds for $E \rightarrow B$.

the assumed instrument’s sensitivity to polarization orientations relative to fixed sky coordinates; and a ‘relative’ rotation error between various pairs of detectors. For PICO, the relative rotation of the detectors will be measured to $0.1'$ by comparing the measured polarization signals between many independent detectors and pairs. However, directly measuring the overall rotation in flight – which is the process of calibrating the polarization angles – is challenging, since there are no sufficiently well calibrated polarized astronomical sources. For example, Aumont et al. [192] showed that for the best characterized source – the Crab Nebula – the current uncertainty of 0.33° on the polarization orientation limits measurements to $r \sim 0.01$.

PICO will overcome this potential source of error in data analysis. Yadav et al. [180] showed that because the T and E signals are much stronger than B , an experiment that searches for a specific level of cosmological BB will have high SNR for detecting spurious EB and TB cross-spectra arising from error in the calibration of the polarization angle. Applying their method to the PICO baseline specifications we find a constraint of $\alpha < 0.2'$ and $0.6'$ (3σ) using the EB and TB spectra, respectively, and thus a suppression of this systematic effect to negligible levels (Fig. 2.14). The constraints quoted include a delensing level of 73%, which is the PICO forecast including foreground separation.

2.8.3 Differential Gain

Photometric calibration is the process of converting the raw output of each detector – typically given in digital readout units – to physical units via a calibration factor $C(t)$, which is a function of time. One straightforward way for PICO to derive Q and U is through differencing detectors that are sensitive to two orthogonal polarization states A and B . A systematic error in the determination of either A or B calibration factors will translate to a biased Q or U . We investigated whether the anticipated error on $C_{A,B}(t)$ is adequate for PICO’s requirements on measuring the inflationary signal.

We assume that the inflationary signal will be extracted from data in the primary CMB bands between 60 and 300 GHz. Detectors in these bands will be calibrated using measurements of the CMB dipole, a signal that will be measured once per minute as the telescope scans the sky (§ 4.1.2). We evaluated the combined impact of the scan strategy and white- and $1/f$ noise in the estimation

of $C(\ell)$. The simulation included signals from the anisotropy of the CMB, including the dipole and BB lensing. Full details of the simulation pipeline are available in the PICO website [193]. Figure 2.14 demonstrates that the power spectrum due to error in $C_{A,B}(T)$ is much lower than the PICO requirement of $\sigma(r) = 1 \times 10^{-4}$.

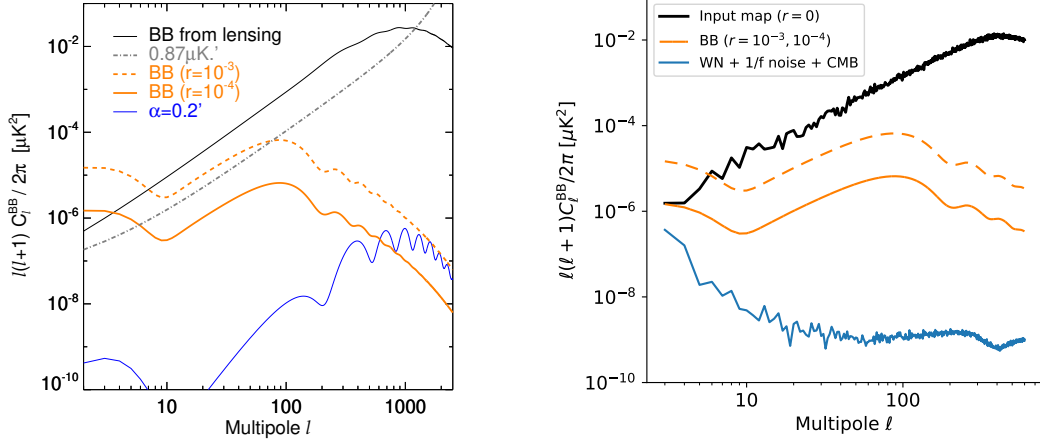


Figure 2.14: Two of the initially-estimated highest priority systematic effects for PICO can be suppressed to low levels relative to requirements; here we show inflationary signals with $r = 1 \times 10^{-4}$ and 1×10^{-3} (solid and dash orange, respectively), and BB lensing (black, theory on the left; realization on right). **Left:** The residual spurious BB spectrum due to $0.2'$ mis-calibration of PICO’s angles of polarization sensitivity (solid blue) has the shape of the EE spectrum, and is small compared to the requirement for $\ell < 200$ and compared to the baseline statistical noise level (grey dash). **Right:** Simulated residual BB power after accounting for calibration drifts (solid blue).

2.8.4 Far Sidelobes

Differences between the assumed and actual antenna pattern of the detectors will give rise to systematic errors. Such differences are particularly hard to detect in the ‘far-sidelobes’ where the antenna pattern is below the noise level. Unknown far-sidelobe response can couple to bright Galactic signals when the telescope points tens of degrees away from the Galactic plane, and cause spurious signals. To evaluate PICO’s susceptibility to this systematic effect we computed PICO’s 4π sr antenna response for four 155 GHz detectors located at the center of the focal plane. We simulated the time domain response of the detectors as they scan the sky over a year of PICO observations. We convolved their antenna response with a full-sky Galactic emission model [177], reconstructed maps of I , Q , and U , and calculated the resulting BB angular power spectrum when using a *Planck* Galactic mask excluding 60% of the sky [194].

The largest sidelobe in the antenna response is at a level of -80 dB from the main lobe. We find that if that sidelobe is known to a level of -95 dB ($SNR > 20$), or further suppressed to that level, the contamination from the sidelobe is a factor of ten below the requirement of $\sigma(r) = 5 \times 10^{-4}$. This suppression can be achieved by adding baffles and through ground-based measurements. *Planck*’s ground-based measurements mapped the antenna response to levels between -90 and -100 dB from the main lobe [195]. The combination of measurements and modeling will be used to remove sidelobe pickup during data analysis.

2.8.5 Additional Key Findings

Properly modeling, engineering for, and controlling systematic effects are key for the success of any experimental endeavor striving to achieve $\sigma(r) \lesssim 1 \times 10^{-3}$. Based on extensive community

experience with both hardware and analysis of data we make the following points.

- Relative to other platforms, a space-based mission provides the most thermally stable platform, and thus the prerequisite for improved control of systematic effects. PICO’s orbit at L2 is among the most thermally stable of possible orbits.
- PICO’s sky scan pattern gives strong data redundancy, which enables numerous cross-checks. Each of the 12,996 detectors makes independent maps of the I , Q , and U Stokes parameters enabling many comparisons within and across frequency bands, within and across sections of the focal plane, and within and across bolometers that have either the same or different polarization sensitivities. Half the sky is scanned every two weeks, and the entire sky is scanned in 6 months. Thus combinations of maps constructed at different times during of the mission will be differenced to search for residual time-dependent systematic effects.
- The scan pattern gives almost continuous scans of planets and large amplitude (≥ 4 mK) CMB dipole signals [193]. These features result in continuous, high SNR calibration and antenna-pattern characterization. In comparison, *Planck* observed each of the planets with only a 6 month cadence and had nearly 100 days/year during which the dipole calibration signals were below 4 mK, at times dipping below 1 mK.
- We showed that two of the highest priority systematic effects can be controlled to levels that are small compared to requirements. More analysis and planning is required to address systematic uncertainties arising from the far-sidelobe response of the telescope.

We strongly recommend that further support be provided for further analysis of systematic effects, their combinations, and their coupling with foreground separation. Specifically, support for suborbital efforts is essential to continue the development of means to identify systematic effects, and to develop new techniques to mitigate them. We also endorse support for the development of a complete end-to-end software simulation facility, which is the most robust way to quantify mission trade-offs under the influence of a combination of systematic effects that are coupled to the task of signal separation.

2.9 Complementarity with Sub-Orbital Measurements

Since the first CMB measurements, more than 50 years ago, important observations have been made from the ground, from balloons, and from space. Each of the CMB satellites flown to date – *COBE*, *WMAP*, and *Planck* – has relied on technologies and experience that were the result of sub-orbital efforts. PICO is no different. Examples include: the arrays of micro-fabricated, multi-color pixels and the multiplexed readout that are baselined for the PICO focal plane are a consequence of this decade’s technical developments (§ 3.2, § 3.3); and the recent results from *Planck* and ground-based experiments that established the need for a multitude of frequency bands to characterize and control foregrounds. A healthy sub-orbital program is essential for the success of PICO.

The phenomenal success and the immense science outcomes of past space missions are a direct consequence of their relative advantages (Table 2.3). In every respect, with the exception of repairability and upgradeability, space has the advantage. When the entire sky is needed, as for measurements on the largest angular scales, space is by far the most suitable platform. When broad frequency coverage is needed, space will be required to reach the ultimate limits set by astronomical foregrounds because ground-based observations are limited to a handful of atmospheric windows, mostly below 300 GHz. Balloons can provide useful information at higher frequencies, but their limited observing time limits SNR. The stability offered in space can not be matched on any other platform, and it translates to superb control of systematic uncertainties.

Table 2.3: Relative characteristics of ground, balloon, and space platforms for experiments in the CMB bands.

Characteristic	Ground	Balloon	Space
Sky coverage	Partial from single site	Partial from single flight	Full
Frequency coverage	70 GHz inaccessible, ^a $v \geq 300$ GHz unusable, limited atmospheric windows	70 GHz inaccessible, ^a otherwise, almost unlimited	Unrestricted
Angular resolution at 150 GHz ^b	1. ⁵ with 6 m telescope	6' with 1.5 m telescope	6' with 1.5 m telescope
Detector noise ^c	$265 \mu\text{K}_{\text{CMB}} \sqrt{\text{s}}$	$162 \mu\text{K}_{\text{CMB}} \sqrt{\text{s}}$	$38 \mu\text{K}_{\text{CMB}} \sqrt{\text{s}}$
Integration time	Unlimited, with interruptions	Weeks, continuous	Several years, continuous
Repairability, Upgradeability ...	Good	None; multiple flights possible	None

^a 70 GHz is the frequency at which large angular scale B -mode Galactic emissions have a minimum (Fig. 2.11).

^b We give representative telescope apertures. Significantly larger apertures for balloons and in space result in higher mass, volume, and cost.

^c The noise-equivalent temperatures given are illustrative of general capabilities. Detailed comparisons depend on detector heat-sink temperatures, bandwidths, and other factors that differ among specific implementations. Ground – median detector noise at 95 GHz from BICEP3 [196]; balloon – median detector noise at 94 GHz from SPIDER [197]; space – 90 GHz from PICO CBE.

The relative advantages of a space mission used to come with higher costs relative to sub-orbital experiments. However, this balance now shifts. To make further advances in CMB science it is now required to mount massive ground-based efforts. By the early 2020s, S3 experiments plan to implement more than 100,000 detectors in 9 receivers in Chile and the South Pole. The total cost is in the vicinity of \$100M. The cost for a subsequent scale-up, a \sim 500,000-detector ground-based CMB experiment planned for the next decade, is squarely within the cost window of this Probe. Even at that cost, the PICO goal of reaching $r = 5 \times 10^{-4}$ (5σ) is beyond the reach of sub-orbital observations in the foreseeable future.

For measuring r and for achieving the other PICO SOs, a space-based platform is either necessary or has strong advantages. For science requiring higher angular resolution, such as observations of galaxy clusters with 1 arcmin resolution at 150 GHz, the ground has an advantage. An appropriately large aperture on the ground will also provide high-resolution information at lower frequencies, which may be important for separating Galactic emissions at high ℓ . We therefore recommend to pursue a space mission in the next decade, and to complement it with a ground-based program that will overlap in ℓ space, and will add science at the highest angular resolution, beyond the reach of a space mission.

Balloon observations have been exceedingly valuable in the past, and will continue to play an important role through making measurements at frequency bands above 280 GHz. Because balloon observations are largely free from the noise induced by atmospheric turbulence, they are suited for probing the low ℓ multipoles. The balloon environment is the best available for elevating the TRL of relevant technologies.

2.10 Measurement Requirements

The set of physical parameters and observables that derive from the PICO SOs place requirements on the depth of the mission, the fraction of sky the instrument scans, the frequency range the instrument probes and the number of frequency bands, the angular resolution provided by the reflectors, and the specific pattern with which PICO will observe the sky.

- **Depth** We quantify survey depth in terms of the RMS fluctuations that would give an SNR ratio of 1 in $1' \times 1'$ sky pixel. The science objective driving the depth requirement is SO1, the search for the inflationary signal, which requires a combined depth of $0.87 \mu\text{K} \cdot \text{arcmin}$. This requirement is a combination of the low level of the signal, the need to separate the various signals detected in each band, and the need to detect and subtract systematic effects to anticipated levels. The map depth requirement flows to instrument sensitivity requirements (Table ??) and to the mission duration requirement (5 years), assuming 95% survey efficiency.

- **Sky Coverage** There are several SOs driving a full-sky survey for PICO. The term ‘full-sky’ refers to the entire area of sky available after separating astrophysical sources of confusion. In practice this implies an area of 50–70% of the sky for probing non-Galactic signals, and 100% of sky for achieving the Galactic science goals.

(1) Probing the optical depth to the epoch of reionization (SO5) requires full sky coverage as the signal peaks in the EE power spectrum on angular scales of 20° to 90° ($2 \leq \ell \leq 10$). Measuring this optical depth to limits imposed by cosmic variance?? is key for minimizing the error on the neutrino-mass measurement.

(2) The inflationary BB power spectrum (SO1) has local maxima in the ‘reionization peak’ ($2 \leq \ell \leq 10$), and in the ‘recombination peak’ ($\ell \simeq 80$) (Fig. ??). A detection would strongly benefit from confirmation at *both* angular scales. Measurements of the reionization peak are currently beyond the capabilities of ground-based instruments. A detection would also strongly benefit from confirmation *in several independent patches of the sky*. This is achievable with PICO through observing the recombination peak in several small (3–5% sky fraction) patches of the sky. No similar capability is currently planned for any next-decade instrument.

(3) The PICO constraint on N_{eff} (SO4) requires determination of the TT , TE , and EE power spectra, limited by cosmic variance at $\ell = 3500$ (2500) for TT (EE). To achieve this, full sky coverage is required.

(4) Achieving the targeted neutrino mass limits (SO3), giving two independent 4σ constraints on the minimal sum of 58 meV, requires a lensing map and cluster counts from as large a sky fraction as possible.

(5) PICO’s survey of the Galactic plane and regions outside of it is essential to achieving its Galactic structure and star-formation science goals (SO6, 7).

- **Frequency Bands** The multitude of astrophysical signals that PICO will characterize determine the frequency range and number of bands that the mission requires. The Galactic and cosmological signals are separable using their spectral signatures. The cosmological signals peak in the frequency range between 60 and 300 GHz. Galactic signals, specifically the make-up of Galactic dust (SO6), require spectral characterization at frequencies between 100 and 800 GHz. Simulations indicate that 21 bands, each with 25% bandwidth, that are spread across the range 20–800 GHz can achieve the separation between Galactic and cosmological signals at the level of fidelity required by PICO (§ 2.7).

- **Resolution** Several SOs require the resolution per frequency listed in Table 1.1. To reach $\sigma(r) = 1 \times 10^{-4}$ we will need to ‘delens’ the B -mode map, as described in § ?? and § 2.3.2. De-lensing efficacy is a function of noise and resolution. For PICO, the combination of the two gives between 73 and 85% delensing, which is adequate for achieving our SOs. The process of delensing may be affected by contamination from Galactic dust. It is thus required to map Galactic dust to at least the same resolution as in the main CMB bands. Higher resolution is mandated by SO6 and 7, which require resolution of $1'$ at 800 GHz.

The constraints on the number of light relics (SO4) will be extracted from the TT , TE and EE power spectra at $\ell \lesssim 4000$, which requires the resolution specified in Table 1.1.

- **Sky Scan Pattern** Control of polarization systematics uncertainties at anticipated levels is enabled by: (1) making I , Q , and U Stokes-parameter maps of the entire sky from each independent detector; (2) by enabling sub-percent absolute gain calibration of the detectors through observations of the CMB dipole; and (3) by enabling cross-checks on the results through comparing multiple cuts of the data, a process known as ‘jack-knife test’. With these requirements we chose a sky scan pattern (§ 4.1.2) that enables each detector to scan a given pixel of the sky in a multitude of directions, satisfying requirement (1). The scan gives large amplitude CMB dipole signals in spacecraft rotations throughout the lifetime of the mission, satisfying requirement (2). With PICO’s sky scan pattern, more than 50% of the sky is scanned within two weeks of the start of the survey. The entire sky is surveyed within 6 months, and then this pattern repeats. Thus the PICO scan pattern gives 10 independent maps and multiple ways to perform data jack-knives, satisfying requirement (3).

3 Instrument

PICO meets all of its science-derived instrument requirements (§ 2.10) with a single instrument: an imaging polarimeter with 21 logarithmically spaced frequency bands centered between 21 and 799 GHz (Table ??). The instrument has a two-reflector Dragone-style telescope (§ 3.1 and Fig. 3.1). The focal plane is populated by 12,996 transition-edge-sensor (TES) bolometers (§ 3.2) and read out using a time-domain multiplexing scheme (§ 3.3). PICO employs a single science observing mode: fixed rate imaging while scanning the sky (§ 4.1.2).

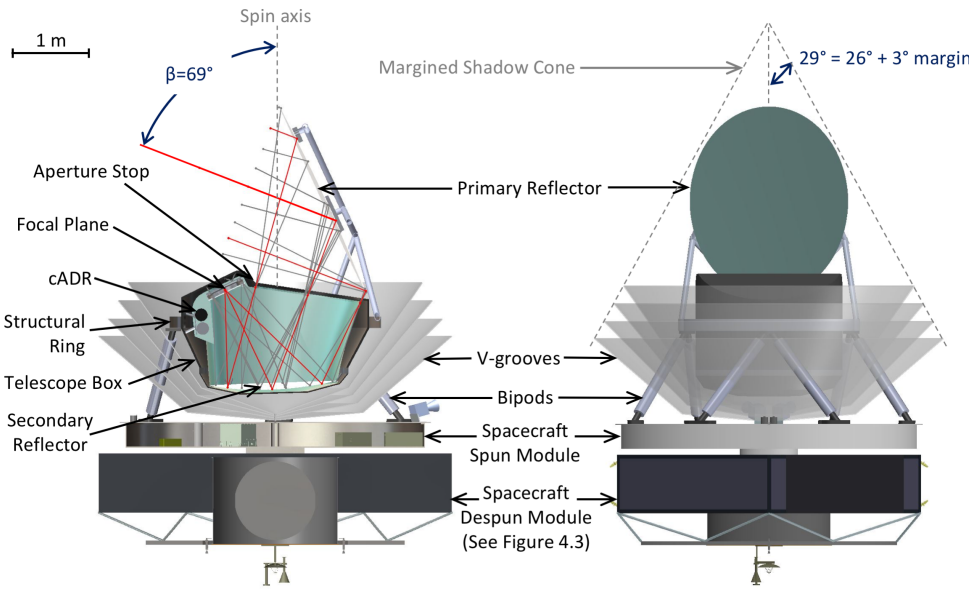


Figure 3.1: PICO overall configuration in side view and cross section (left), and front view with V-Groove assembly shown semi-transparent (right). The mission consists of a single science instrument mounted on a structural ring. The ring is supported by bipods on a stage spinning at constant speed relative to a despun module. Figure 3.2 shows the functions hosted by each of the modules.

The instrument is configured inside the shadow of a V-groove assembly that thermally and optically shields it from the Sun (Fig. 3.1 and § 3.4.3). The Sun shadow cone depicted in Fig. 3.1 is 29° . The angle to the Sun during the survey, $\alpha = 26^\circ$ (§ 4.1.2 and Fig. 4.2), is supplemented with

a margin of 3° to account for the radius of the Sun ($0^\circ 25$), pointing control error, design margin, and alignment tolerances.

The V-groove assembly is attached to the bipod struts that support the instrument structural ring. The ring supports the primary reflector and telescope box. The telescope box contains the actively cooled components (§ 3.4.1, § 3.4.2), including the secondary reflector, the focal plane and sub-kelvin refrigerator structures. Just inside the box, a thermal liner serves as a cold optical baffle and aperture stop. Instrument integration and test are described in § 3.5.

During the survey, the instrument is spun at 1 rpm and the spin axis is made to precess about the anti-Sun direction (§ 4.1.2). Spacecraft control is simplified by mounting the instrument on a spinning spacecraft module, while a larger non-spinning module houses most spacecraft subsystems (§ 4.3). Instrument elements that act as heat sources are accommodated on the spinning module of the spacecraft. Only power and digital data lines cross between the spinning and non-spinning modules. A functional block diagram of the instrument is shown in Figure 3.2.

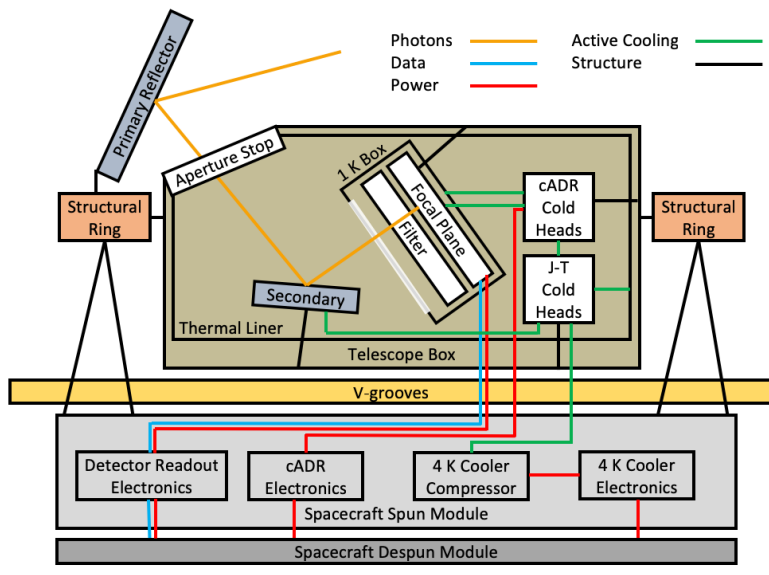


Figure 3.2: PICO instrument block diagram. Active coolers provide cooling to the 100 mK focal plane, the surrounding 1 K box, the 4.5 K secondary reflector, and the 4.5 K thermal liner that acts as a cold aperture stop. V-grooves provide passive cooling. The instrument, V-grooves, and spacecraft spun module spin together at a rate of 1 RPM. The spacecraft spun module hosts the 4 K cooler compressor and drive electronics, the sub-K cooler drive electronics, and the detector warm readout electronics. Only power and digital data lines cross to the spacecraft despun module, which hosts the spacecraft power, telemetry, attitude control, and communication systems (§ 4.3).

3.1 Telescope

The PICO telescope design is driven by a combination of science requirements and physical volume limits. The science requirements are: a large diffraction-limited field of view (DLFOV) sufficient to support approximately 10^4 detectors; arcminute resolution at 800 GHz; low spurious polarization; and low sidelobe response. All requirements are met with PICO’s 1.4 m aperture modified open-Dragone design. There are no moving parts in the PICO optical system.

The PICO optical design was selected following a trade study examining cross-Dragone, Gregorian Dragone, and open-Dragone designs [198]. The open-Dragone and crossed-Dragone systems offer more diffraction-limited focal-plane area than the Gregorian Dragone one [199] and are able to support enough detectors to provide the required sensitivity. The open-Dragone design does not require the more massive and voluminous baffles that the cross-Dragone does, and hence can satisfy the aperture size requirement within the shadow cone.

PICO's initial open-Dragone design [200, 201] has been modified with the addition of an aperture stop and adding corrections to the primary and secondary reflectors to enlarge the DLFOV. The detailed geometric parameterization of the PICO optical design is described by Young et al. [198]. The primary reflector ($270\text{ cm} \times 205\text{ cm}$) is passively cooled and the secondary reflector ($160\text{ cm} \times 158\text{ cm}$) is actively cooled. The highest frequency (900 GHz) sets the surface accuracy requirement of the reflectors at $\lambda/14 = 24\text{ }\mu\text{m}$. The focal ratio is 1.42. The slightly concave focal surface, which has a radius of curvature of 4.55 m, is telecentric to within $0^\circ 12$ across the entire FOV.

An actively cooled circular aperture stop between the primary and secondary reflectors reduces detector noise and shields the focal plane from stray radiation. Stray-light analysis of the PICO open-Dragone design using GRASP confirms that the focal plane is protected from direct view of the sky, and that spillover past the primary is suppressed by 80 dB relative to the main lobe for both co-pol and cross-pol beams. Detailed baffle design will be performed during mission formulation.

3.2 Focal Plane

PICO's focal plane is populated by an array of TES bolometers operating in 21 frequency bands, each with 25% fractional bandwidth, and band centers ranging from 21 to 799 GHz. The layout of the PICO focal plane is shown in Fig. 3.3 and detailed in Table 3.1.

Bolometers operating in the mm/sub-mm wave band are photon-noise limited. Therefore, increase in sensitivity is achieved through an increase in detector count. The PICO focal plane has 12,996 detectors, 175 times the number flown aboard *Planck*, thereby providing a breakthrough increase in sensitivity with a comparably sized telescope. This breakthrough is enabled by development and demonstration in suborbital projects, which now commonly operate arrays of $10^3\text{--}10^4$ detectors (§ 5). Further technology maturation required for PICO is described in Section § 5.

3.2.1 21–462 GHz Bands

Several optical-coupling technologies have matured over the past ten years to efficiently use focal-plane area: horns with ortho-mode transducers (OMTs) [202]; lithographed antenna arrays [203]; and sinuous antennas under lenslets [204]. Horn-coupling and sinuous antenna/lenslet-coupling deliver quantum efficiency $> 70\%$ over more than an octave of bandwidth, which have been partitioned into two or three colors per pixel. Only single-color pixels have been demonstrated to date with antenna-arrays, but this coupling enables smaller pixels and therefore they can be more densely packed.

The PICO baseline focal plane employs three-color sinuous antenna/lenslet pixels [205] for the 21–462 GHz bands. Niobium microstrips mediate the signals between the antenna and detectors, and

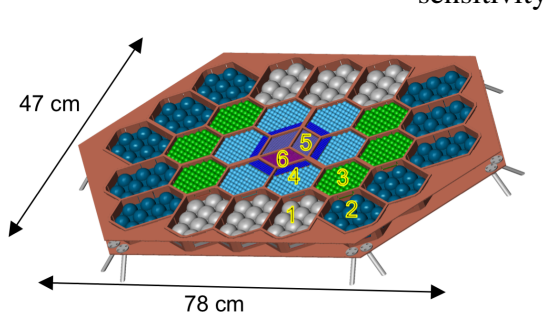


Figure 3.3: PICO focal plane. Detectors are fabricated on six types of tiles (shown numbered and colored as in Table 3.1). The wafers are located on the focal plane such that higher frequency bands, which require better optical performance, are placed nearer to the center. All detectors are within the diffraction-limited performance for their respective frequency bands.

therefore they can be more densely packed.

Table 3.1: PICO makes efficient use of the focal area with multichroic pixels (three bands per pixel, § 3.2.1). The sampling rate is based on the smallest beam (Table 3.2), with 3 samples per FWHM at a scan speed ($360^\circ/\text{min}$) $\sin(\beta = 69^\circ) = 336^\circ/\text{min}$. Scaling from suborbital experience, we anticipate that TES bolometers can support these sampling rates with $\sim 4\times$ margin.

Tile type	N_{tile}	Pixels/tile	Pixel type	Band centers [GHz]	Sampling rate [Hz]
-----------	-------------------	-------------	------------	--------------------	--------------------

partition the wide continuous bandwidth into three narrow channels using integrated, on-wafer, micro-machined filter circuits [206]. Six transition edge sensor bolometers per pixel detect the radiation in two orthogonal polarization states.

3.2.2 555–799 GHz Bands

PICO’s highest three frequency channels are beyond the niobium superconducting band-gap, rendering on-wafer, microstrip filters a poor solution for defining the optical passband. For these bands we use feedhorns to couple the radiation to two single-color polarization-sensitive TES bolometers. The waveguide cut-off defines the lower edge of the band, and quasi-optical metal-mesh filters define the upper edge. Numerous experiments have successfully used similar approaches [207–209].

3.2.3 Polarimetry

Polarimetry is achieved by differencing the signals from pairs of two co-pointed bolometers within a pixel that are sensitive to two orthogonal polarization states. Half the pixels in the focal plane are sensitive to the Q and half to the U Stokes parameters of the incident radiation. Two layouts for the distribution of the Q and U pixels on the focal plane have been investigated [210]; both would satisfy mission requirements. Stokes I is obtained from the sum of the signals of orthogonal detectors.

3.2.4 Sensitivity

PICO’s Current Best Estimate (CBE) sensitivity meets the requirements of the baseline mission with $> 40\%$ margin (Table 3.2).

We developed an end-to-end noise model of the PICO instrument to predict mission sensitivity and provide a metric by which to evaluate mission design trades. The model includes four noise sources per bolometer: photon, phonon, Johnson, and readout (from both cold and warm readout electronics). To validate our calculations, we compared two independent software packages that have been validated with several operating CMB instruments. The calculations agreed within 1% both for individual noise terms and for overall mission noise. A detailed description of the PICO noise model and its inputs is available in Young et al. [198]; small differences between that publication and Table 3.2 are due to refinements of the primary mirror and stop temperatures.

Laboratory experiments have demonstrated that TES bolometers can be made background-limited in the low loading environment they would experience at L2 [211]. For PICO, the primary contributor to noise is the optical load. The sources of optical load are the CMB, reflectors, aperture stop, and low-pass filters. The CMB and stop account for at least 50% of the optical load at all frequencies up to and including 555 GHz. At higher bands emission from the primary mirror dominates.

The sensitivity model assumes white noise at all frequencies. Sub-orbital submillimeter experiments have demonstrated TES detectors that are stable to at least as low as 20 mHz [212], meeting the requirements for PICO’s scan strategy (§ 4.1.2).

Table 3.2: PICO has 21 partially overlapping frequency bands with band centers (v_c) from 21 GHz to 799 GHz and each with bandwidth $\Delta v/v_c = 25\%$. The beams are single mode, with FWHM sizes of $6.2' \times (155\text{GHz}/v_c)$. The CBE per-bolometer sensitivity is photon-noise limited (§ 3.2.4). The total number of bolometers for each band is equal to (number of tiles) \times (pixels per tile) \times (2 polarizations per pixel), from Table 3.1. Array sensitivity assumes 90% detector operability. The map depth assumes 5 yr of full sky survey at 95% survey efficiency, except the 25 and 30 GHz frequency bands, which are conservatively excluded during 4 hr/day Ka-band (26 GHz) telecom periods (§ 4.2).

Band center [GHz]	Beam FWHM [arcmin]	CBE bolo NET [$\mu\text{K}_{\text{CMB}} \text{s}^{1/2}$]	N_{bolo}	CBE array NET [$\mu\text{K}_{\text{CMB}} \text{s}^{1/2}$]	Baseline array NET [$\mu\text{K}_{\text{CMB}} \text{s}^{1/2}$]	Baseline polarization map depth	
				[$\mu\text{K}_{\text{CMB}} \text{s}^{1/2}$]	[$\mu\text{K}_{\text{CMB}} \text{s}^{1/2}$]	[$\mu\text{K}_{\text{CMB}} \text{arcmin}$]	[Jy sr $^{-1}$]
21.....	38.4	112	120	12.0	17.0	23.9	8.3
25.....	32.0	103	200	8.4	11.9	18.4	10.9
30.....	28.3	59.4	120	5.7	8.0	12.4	11.8
36.....	23.6	54.4	200	4.0	5.7	7.9	12.9
43.....	22.2	41.7	120	4.0	5.6	7.9	19.5
52.....	18.4	38.4	200	2.8	4.0	5.7	23.8
62.....	12.8	69.2	732	2.7	3.8	5.4	45.4
75.....	10.7	65.4	1020	2.1	3.0	4.2	58.3
90.....	9.5	37.7	732	1.4	2.0	2.8	59.3
108.....	7.9	36.2	1020	1.1	1.6	2.3	77.3
129.....	7.4	27.8	732	1.1	1.5	2.1	96.0
155.....	6.2	27.5	1020	0.9	1.3	1.8	119
186.....	4.3	70.8	960	2.0	2.8	4.0	433
223.....	3.6	84.2	900	2.3	3.3	4.5	604
268.....	3.2	54.8	960	1.5	2.2	3.1	433
321.....	2.6	77.6	900	2.1	3.0	4.2	578
385.....	2.5	69.1	960	2.3	3.2	4.5	429
462.....	2.1	133	900	4.5	6.4	9.1	551
555.....	1.5	658	440	23.0	32.5	45.8	1580
666.....	1.3	2210	400	89.0	126	177	2080
799.....	1.1	10400	360	526	744	1050	2880
Total		12 996		0.43	0.61	0.87	

3.3 Detector Readout

Suborbital experiment teams over the past ten years have chosen to use voltage-biased TESs because their current readout scheme lends itself to superconducting quantum interface device (SQUID)-based multiplexing. Multiplexing reduces the number of wires to the cryogenic stages and thus the total thermal load that the cryocoolers must dissipate. This approach also simplifies the instrument design.

In the multiplexing circuitry, SQUIDs function as low-noise amplifiers and cryogenic switches. The current baseline for PICO is to use a time-domain multiplexer (TDM), which assigns each detector's address in a square matrix of simultaneously read columns, and sequentially cycles through each row of the array [213]. The PICO baseline architecture uses a matrix of 128 rows and 102 columns. The thermal loading on the cold stages from the wire harnesses is subdominant to conductive loading through the mechanical support structures.

Because SQUIDs are sensitive magnetometers, suborbital experiments have developed techniques to shield them from Earth's magnetic field using highly permeable or superconducting materials [214]. Total suppression factors better than 10^7 have been demonstrated for dynamic

Table 3.3: Projected cooler heat lift capabilities offer more than 100 % heat lift margin, complying with cooler technology best practices [222].

Component	Temperature [K]		Active heat lift [mW]		
	Required	CBE	Required per model ^a	Capability today	Projected capability
Primary reflector	< 40	17	N/A (radiatively cooled)		
Secondary reflector	< 8	4.5			
Aperture stop	4.5	4.5	42 at 4.5 K	> 55 at 6.2 K ^b	> 100 at 4.5 K ^c
cADR heat rejection ^d	4.5	4.5			
Focal plane enclosure and filter	1.0	1.0	0.36	1.0	N/A ^e
Focal plane	0.1	0.1	5.7×10^{-3}	32×10^{-3}	N/A ^e

^a The required loads were calculated using Thermal Desktop. Reference [223] was used to estimate the thermal conductive loads through mechanical supports. In addition to the listed components, the total 4.5 K heat load includes the intercept on the focal plane mechanical supports. ^b Reference [224]. ^c Both NGAS and Ball project >

100 mW lift capability at 4.5 K using higher compression-ratio compressors currently in development (§ 3.4.2 and Fig. 3.4). ^d The cADR lift capability at 1 K and 0.1 K is from a GSFC quote. ^e Capability today already exceeds requirement.

magnetic fields [215]. PICO will use these demonstrated techniques to shield SQUID readout chips from the ambient magnetic environment, which is 20,000 times smaller than near Earth, as well as from fields generated by on-board components, including the 0.1 K cooler (§ 3.4.1). This cooler is delivered with its own magnetic shielding, which reduces the field at the distance of the SQUIDs to less than 0.1 G, which is less than Earth’s field experienced by SQUIDs aboard suborbital experiments. SQUIDs are also sensitive to radio-frequency interference (RFI). Several suborbital experiments have demonstrated RFI shielding using aluminized mylar wrapped at cryogenic stages to form a Faraday cage around the SQUIDs [216–218]. Cable shielding extends the Faraday cage to the detector warm readout electronics.

Redundant warm electronics boxes perform detector readout and instrument housekeeping using commercially available radiation-hardened analog-to-digital converters, requiring 75 W total. The readout electronics compress the data before delivering them to the spacecraft, requiring an additional 15 W. PICO detectors produce a total of 6.1 Tbits/day assuming 16 bits/sample, sampling rates from Table 3.1, and bolometer counts from Table 3.2. *Planck* HFI had a typical 4.7× compression in flight, with information loss increasing noise by only about 10% [219, 220]. Suborbital work has demonstrated 6.2× lossless compression [221]. PICO assumes 4× lossless compression.

3.4 Thermal

Like the *Planck*-HFI instrument, PICO’s focal plane is maintained at 0.1 K to ensure low detector noise while implementing readily available technology (§ 3.4.1). To minimize detector noise due to instrument thermal radiation, the aperture stop and reflectors are cooled using both active and radiative cooling (§ 3.4.2, § 3.4.3, Fig. 3.2). All thermal requirements are met with robust margins (Table 3.3).

3.4.1 cADR Sub-Kelvin Cooling

A multi-stage continuous adiabatic demagnetization refrigerator (cADR) maintains the PICO focal plane at 0.1 K and the surrounding enclosure, filter, and readout components at 1 K. The cADR

employs three refrigerant assemblies operating sequentially to absorb heat from the focal plane at 0.1 K and reject it to 1 K. Two additional assemblies, also operating sequentially, absorb this rejected heat at 1 K, cool other components to 1 K, and reject heat at 4.5 K. This configuration provides continuous cooling with small temperature variations at both the 0.1 K and 1 K. Heat straps connect the two cADR cold sinks to multiple points on the focal-plane assembly, which has high thermal conductance paths built in, to provide spatial temperature uniformity and stability during operation. The detector arrays are thermally sunk to the mounting frame. Heat loads in the range of $30 \mu\text{W}$ at 0.1 K and 1 mW at 1 K (time-average) are within the capabilities of current cADRs developed by GSFC (§ 6.3) [225, 226]. The PICO sub-kelvin heat loads are estimated at less than half of this capability (Table 3.3).

3.4.2 The 4.5 K Cooler

A cryocooler system similar to that used on JWST to cool the MIRI detectors [227, 228] removes the heat rejected from the cADR and cools the aperture stop and secondary reflector to 4.5 K. Both NGAS (which provided the MIRI coolers) and Ball Aerospace have developed such coolers under the NASA-sponsored Advanced Cryocooler Technology Development Program [229]. NGAS and Ball use slightly different but functionally-equivalent hardware approaches. A 3-stage precooler provides 16 K precooling to a separate circulated-gas loop. The circulated-gas loop utilizes Joule–Thomson (J-T) expansion, further cooling the gas to 4.5 K. The J-T expansion point is located close to the cADR heat rejection point and provides to it the lowest temperature. Subsequently, the gas flow intercepts heat conducted to the focal-plane enclosure, then cools the aperture stop and the secondary reflector before returning to the circulation compressor.

NGAS and Ball are actively working on increasing the flow rate and compression ratio of the J-T compressor, which should result in higher system efficiency and greater heat-lift relative to the current MIRI cooler. NGAS uses ^4He as the circulating gas, as was used for MIRI. Ball uses a somewhat larger compressor and ^3He as the circulating gas. Both employ re-optimized heat exchangers. The NGAS project has completed PDR-level development, and is expected to reach CDR well before PICO begins Phase-A. The projected performance of this cooler is shown in Fig. 3.4; it gives 100 mW at 250 W input power, which is more than 100 % heat lift margin relative to PICO’s requirements (Table 3.3). For PICO we have assumed an input power of 350 W.

The entire precooler assembly and the J-T circulator compressor are located on the warm spacecraft spun module (Fig. 3.2). All waste heat rejected by the cooler compressors and drive electronics is transferred to the spacecraft heat-rejection system. Unlike JWST, the PICO cooler does not require deployment of the remote cold head.

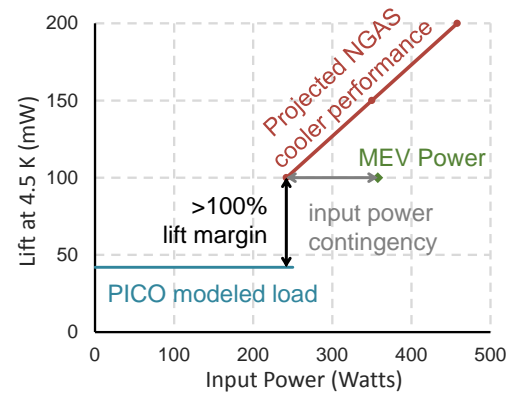


Figure 3.4: Projected performance of the NGAS cooler using a multi-stage compressor and ^4He circulating gas [227] meets PICO’s requirements with $> 100\%$ margin. PICO requires heat lift of 42 mW at 4.5 K (Table 3.3). With 250 W of input power the NGAS cooler is projected to provide 100 mW of heat lift. We conservatively specify a maximum expected value (MEV) of 350 W as the compressor’s input power, giving 100 W of additional input power contingency.

3.4.3 Radiative Cooling

An assembly of four nested V-groove radiators, acting as radiation shields, provides passive cooling (Fig. 3.1). This is standard, 30-years old technology (§ 6.3). The outermost shield shadows the interior ones from the Sun. The V-grooves radiate to space, each reaching successively cooler temperatures. The assembly provides a cold radiative environment to the primary reflector, structural ring, and telescope box. As a consequence radiative loads on those elements are smaller than the conductive loads through the mechanical support structures.

3.5 Instrument Integration and Test

The PICO instrument integration and testing plan benefits from heritage and experience with the *Planck* HFI instrument [230].

We screen detector wafers prior to selection of flight wafers and focal-plane integration. The cADR and 4 K cryocooler vendors will qualify them prior to delivery. We will determine the relative alignment of the two reflectors under in-flight thermal conditions using a thermal vacuum (TVAC) chamber and photogrammetry. We integrate the flight focal-plane assembly and flight cADR in a dedicated sub-kelvin cryogenic testbed. We characterize noise, responsivity, and focal-plane temperature stability using a representative optical load for each frequency band (temperature-controlled blackbody), and we perform polarimetric and spectroscopic calibration.

The focal plane is integrated with the reflectors and structures, and alignment verified with photogrammetry at cold temperatures in a TVAC chamber. The completely integrated observatory (instrument and spacecraft bus) is tested in TVAC to measure parasitic optical loading from the instrument, noise, microphonics, and RFI. The observatory is 4.5 m in diameter and 6.1 m tall. There are no deployables.

4 Design Reference Mission

The PICO design reference mission is summarized in Table 4.1.

Table 4.1: PICO carries margin on key mission parameters. Maximum Expected Value (MEV) includes contingency.

4.1 Concept of Operations

The PICO concept of operations is similar to that of the successful *WMAP* [231] and *Planck* [232] missions. After launch, PICO cruises to a quasi-halo orbit around the Earth–Sun L2 Lagrange point (§ 4.1.1). A two-week decontamination period is followed by instrument cooldown, lasting about two months. After in-orbit checkout is complete, PICO begins its science survey.

PICO has a single science observing mode, surveying the sky continuously for 5 years using a pre-planned repetitive survey pattern (§ 4.1.2). Instrument data are compressed and stored on-board, then returned to Earth in daily 4-hr Ka-band science downlink passes (concurrent with science observations). Because PICO is observing relatively static Galactic, extragalactic, and cosmological targets, there are no requirements for time-critical observations or data latency. Presently, there are no plans for targets of opportunity or guest observer programs during the prime mis-

Orbit type	Sun-Earth L2 Quasi-Halo
Mission class	Class B
Mission duration	5 years
Propellant (hydrazine).....	213 kg (77 % tank fill)
Launch mass (MEV)	2147 kg (3195 kg capability)
Max power (MEV)	1320 W (with 125 % margin on available solar array area)
Onboard data storage	4.6 Tb (3 days of compressed data, enabling retransmission)

Survey implementation Instrument on spin table

Surveying the sky continuously for 5 years using stabilized

sion. The PICO instrument does not require cryogenic consumables (as the *Planck* mission did), permitting consideration of significant mission extension beyond the prime mission.

4.1.1 Mission Design and Launch

The science survey is conducted from a quasi-halo orbit around the Earth–Sun L2 Lagrange point. *Planck* and *WMAP* also operated in L2 orbits. L2 orbits provide favorable survey geometry relative to Earth orbits by mitigating viewing restrictions imposed by terrestrial and lunar stray light. The PICO orbit around L2 is small enough to ensure that the Sun–Probe–Earth (SPE) angle is less than 15° . This maintains the telescope boresight $> 70^\circ$ away from the Earth (Fig. 4.2, $70^\circ = 180^\circ - \alpha - \beta - \text{SPE}$).

High data-rate downlink to the Deep Space Network (DSN) is available from L2 using near-Earth Ka bands. L2 provides a stable thermal environment, simplifying thermal control. The PICO orbit exhibits no post-launch eclipses.

NASA requires that Probes be compatible with an Evolved Expendable Launch Vehicle (EELV). For the purpose of this study, the Falcon 9 [233] is used as the reference vehicle. Figure 4.1 shows PICO configured for launch in a Falcon 9 fairing. The Falcon 9 launch capability for ocean recovery exceeds PICO’s 2147 kg total launch mass (including contingency) by a 50 % margin.

Insertion to the halo manifold and associated trajectory correction maneuvers require 150 m s^{-1} of total ΔV by the spacecraft. Orbit maintenance requires minimal propellant (statistical $\Delta V \sim 2 \text{ m s}^{-1} \text{ year}^{-1}$). The orbital period is ~ 6 months. There are no disposal requirements for L2 orbits, but spacecraft are customarily decommissioned to heliocentric orbit.

4.1.2 Survey Design

PICO employs a highly repetitive scan strategy to map the full sky. During the survey, PICO spins with a period $T_{\text{spin}} = 1 \text{ min}$ about a spin axis oriented $\alpha = 26^\circ$ from the anti-solar direction (Fig. 4.2). This spin axis is forced to precess about the anti-solar direction with a period $T_{\text{prec}} = 10 \text{ hr}$. The telescope boresight is oriented at an angle $\beta = 69^\circ$ away from the spin axis (Fig. 3.1). This β angle is chosen such that $\alpha + \beta > 90^\circ$, enabling mapping of all ecliptic latitudes. The precession axis tracks along with the Earth in its yearly orbit around the Sun, so this scan strategy maps the full sky (all ecliptic longitudes) within 6 months.

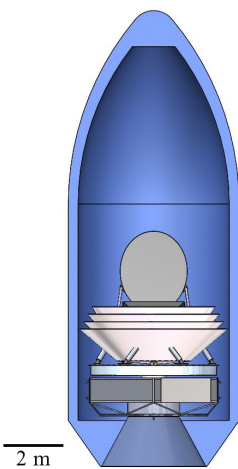


Figure 4.1: PICO is compatible with the Falcon 9.

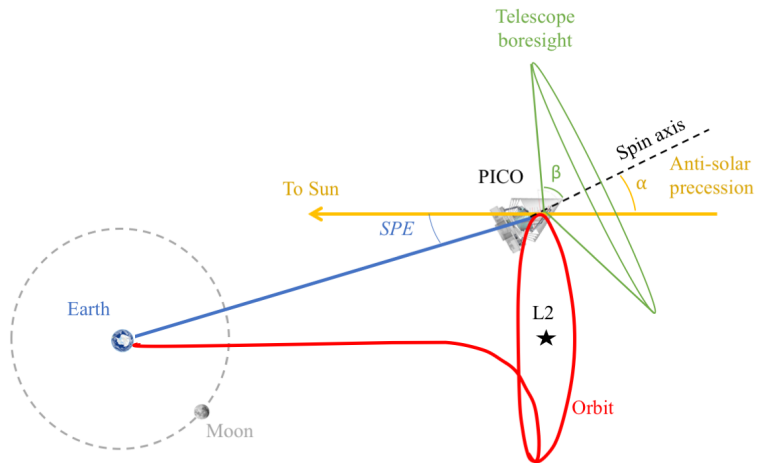


Figure 4.2: PICO surveys by continuously spinning the instrument about a precessing axis.

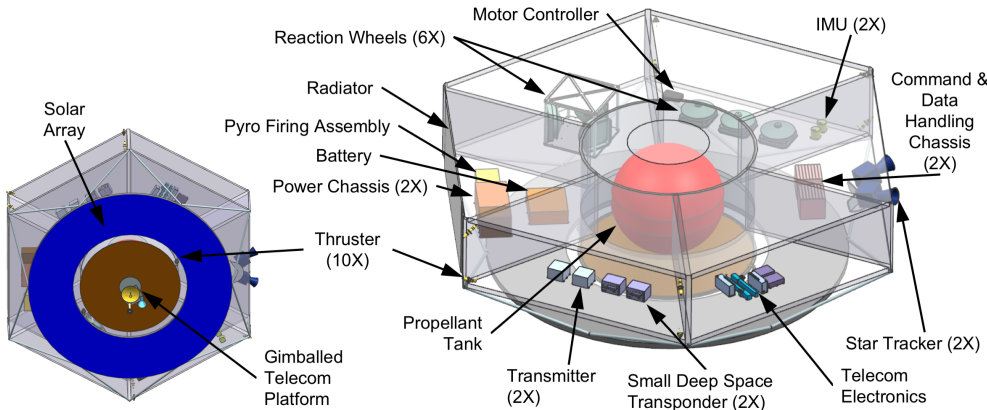


Figure 4.3: Modular equipment bays provide easy access to all components in the spacecraft de-spun module and enable parallel integration of spacecraft subsystems.

PICO’s $\alpha = 26^\circ$ value is chosen to be substantially larger than the *Planck* mission’s α angle (7.5°) to mitigate systematic effects by scanning across each sky pixel with a greater diversity of orientations [234]. Increasing α further would decrease the Sun-shadowed volume available for the optics and consequently reduce the telescope aperture size. A deployable Sunshade was considered, but found not to be required, and was thus excluded in favor of a more conservative and less costly approach.

The instrument spin rate, selected through a trade study, matches that of the *Planck* mission. The study balanced low-frequency ($1/f$) noise subtraction (improves with spin rate) against implementation cost and heritage, pointing reconstruction ability (anti-correlated with spin rate), and data volume (linearly correlated with spin rate). The CMB dipole appears in the PICO data timestream at the spin frequency (1 rpm = 16.7 mHz). Higher multipole signals appear at harmonics of the spin frequency, starting at 33 mHz, above the knee in the detector low-frequency noise (§ 3.2.4). A destriping mapmaker applied in data post-processing effectively operates as a high-pass filter, as demonstrated by *Planck* [235]. PICO’s spin-axis precession frequency is more than 400 times faster than that of *Planck*, greatly reducing the effects of any residual $1/f$ noise by spreading the effects more isotropically across pixels.

4.2 Ground Segment

The PICO Mission Operations System (MOS) and Ground Data System (GDS) can be built with extensive reuse of standard tools. The PICO concept of operations is described in § 4.1. All space-ground communications, ranging, and tracking are performed by the DSN 34 m Beam Wave Guide (BWG). X-band is used to transmit spacecraft commanding, return engineering data, and provide navigation information (S-band is a viable alternative, and could be considered in a future trade). Ka-band is used for high-rate return of science data. The baseline 150 Mb/s transfer rate (130 Mb/s information rate after CCSDS encoding) is an existing DSN catalog service [236]. The instrument produces 6.1 Tb/day, which is compressed to 1.5 Tb/day (§ 3.3). Daily 4 hr DSN passes return PICO data in 3.1 hr, with the remaining 0.9 hr available as needed for retransmission or missed-pass recovery.

4.3 Spacecraft

The PICO spacecraft bus is Class B and designed for a minimum lifetime of 5 years in the L2 environment. Mission-critical elements are redundant. Flight spares, engineering models, and prototypes appropriate to Class B are budgeted.

The aft end of the spacecraft (the “de-spun module”) is comprised of six equipment bays that house standard components (Fig. 4.3). The instrument and V-grooves are mounted on bipods from the spacecraft “spun module,” which contains hosted instrument elements (Fig. 3.1). A motor drives the spun module at 1 rpm to support the science survey requirements (§ 4.1.2). Reaction wheels on the despun module cancel the angular momentum of the spun module and provide three-axis control (§ 4.3.1).

The bipods that mechanically support the instrument are thermally insulating. The passively radiating V-groove assembly thermally isolates the instrument from solar radiation and from the bus (§ 3.4.3). Like *Planck* [232], the V-grooves are manufactured using honeycomb material. Additional radiators on the spun and despun spacecraft modules ($\sim 1 \text{ m}^2$ each) reject heat dissipated by spacecraft subsystems and hosted instrument elements.

PICO’s avionics are dual-string with standard interfaces. Solid-state recorders provide three days of science data storage (4.6 Tbit, § 6.3), enabling retransmission of missed data (§ 4.2).

PICO employs a fully redundant Ka- and X-band telecommunications architecture. The Ka-band system uses a 0.3 m high-gain antenna to support a science data downlink information rate of 130 Mb/s to a 34 m BWG DSN ground station with a link margin of 4.8 dB. The X-band system provides command and engineering telemetry communication through all mission phases using medium- and low-gain antennas. Amplifiers, switches, and all three antennas are on a gimballed platform, enabling Ka and X-band downlink concurrent with science observations.

The heritage power electronics are dual-string. A 74 A-hr Li-ion battery is sized for a 3 hr launch phase with 44 % depth of discharge. After the launch phase, the driving mode is telecom concurrent with science survey (1320 W including 43 % contingency). Solar cells on the aft side of the bus (5.8 m^2 array, $\alpha = 26^\circ$ off-Sun) support this mode with positive power, and unused area in the solar array plane (7.4 m^2 more area by growing to 4.5 m diameter) affords 125 % margin (Fig. 4.3).

The propulsion design is a simple mono-propellant blow-down hydrazine system with standard redundancy. Two aft-pointed 22 N thrusters provide ΔV and attitude control for orbit insertion and maintenance (§ 4.1.1), requiring 140 kg of propellant. Eight 4 N thrusters provide reaction-wheel momentum management and backup attitude-control authority (60 kg of propellant). Accounting for ullage (14 kg), the baseline propellant tank fill fraction is 77 %.

4.3.1 Attitude Determination and Control

PICO uses a zero net angular momentum control architecture with heritage from the SMAP mission (§ 6.3). PICO’s instrument spin rate (1 rpm) matches that of the *Planck* mission, but the precession of the spin axis is faster (10 hr vs 6 months), and the precession angle larger (26° vs 7.5°). These differences make the spin-stabilized *Planck* control architecture impractical.

The PICO instrument spin rate is achieved and maintained using a spin motor. The spin motor drive electronics provide the coarse spin rate knowledge used for controlling the spin rate to meet the ± 0.1 rpm requirement. Data and power are passed across the interface using slip rings.

PICO requires 220 N m s to cancel the angular momentum of the instrument and spacecraft spun module at 1 RPM. This value includes mass contingency and is based on the CAD model. Three Honeywell HR-16 reaction wheel assemblies (RWAs), each capable of 150 N m s, are mounted on the despun module parallel to the instrument spin axis, and spin opposite to the instrument to achieve zero net angular momentum. The despun module is three-axis stabilized. The spin axis is precessed using three RWAs mounted normal to the spin axis in a triangle configuration. Each set

of three RWAs is sized such that two could perform the required function with margin, providing single fault tolerance.

Spin-axis pointing and spin-rate knowledge are achieved and maintained using star tracker and inertial measurement unit (IMU) data. The attitude determination system is single-fault tolerant, with two IMUs each on the spun and despun modules, and two star trackers each on the spun and despun modules. Two Sun sensors on the despun module are used for safe-mode contingencies and instrument Sun avoidance. All attitude control and reconstruction requirements are met, including spin axis control < 60 arcmin with < 1 arcmin/min stability, and reconstructed pointing knowledge < 10 arcsec (each axis, 3σ).

Additional pointing reconstruction is performed in post-processing using the science data. The PICO instrument will observe planets (compact, bright sources) nearly every day. By fitting the telescope pointing to the known planetary ephemerides, the knowledge of the telescope boresight pointing and the relative pointing of each detector will improve to better than 1 arcsec (each axis, 3σ). *Planck*, with fewer detectors, making lower SNR measurements of the planets, and observing with a scan strategy that acquired measurements of each planet only once every 6 months, demonstrated 0.8 arcsec (1σ) pointing reconstruction uncertainty in-scan and 1.9 arcsec (1σ) cross-scan [237].

5 Technology Maturation

PICO builds off of the heritage of *Planck-HFI* and *Herschel*. Since the time of *Planck* and *Herschel*, suborbital experiments have used monolithically fabricated TES bolometers and multiplexing schemes to field instruments with thousands of TES bolometers per camera (Fig. 5.1). By the time PICO enters Phase A, S3 experiments plan to be operating nearly 100,000

TES bolometers in several independent cameras [239–241].

The remaining technology developments required to enable the PICO baseline design are:

1. extension of three-color antenna-coupled bolometers down to 21 GHz and up to 462 GHz (§ 5.1);
2. construction of high-frequency direct absorbing arrays and laboratory testing (§ 5.2);
3. beam line and 100 mK testing to simulate the cosmic ray environment at L2 (§ 5.3);
4. expansion of time-division multiplexing to support 128 switched rows per readout column (§ 5.4).

All of these developments are straightforward extensions of technologies already available today. We recommend APRA and SAT support to complete development of these technologies through the milestones described in Table 5.1.

5.1 21–462 GHz Bands

Suborbital teams have successfully demonstrated a variety of optical-coupling schemes, including horns with ortho-mode transducers (OMTs), lithographed antenna arrays, and sinuous antennas under lenslets (Table 5.2). All have achieved background-limited performance with sufficient margin on design parameters to achieve this performance in the lower background environment at L2. All have been packaged into modules and focal-plane units in working cameras representative of the PICO integration. Experiments have already used a number of PICO’s observing bands between 27 GHz and 270 GHz (Table 5.2). To date, statistical map depths of $3 \mu\text{K}_{\text{CMB}}$ arcmin have been achieved over small sky areas, which is within a factor of five of PICO’s CBE over the entire sky (Table 3.2).

The baseline PICO instrument requires three-color dual-polarized antenna-coupled bolometers covering bands from 21 to 462 GHz (§ 3.2.1). The sinuous antenna has the bandwidth to service three bands per pixel, whereas horns and antenna arrays have only been used for two. Our baseline is to use a three-band sinuous antenna, although we have designs that use two- or one-band per pixel and have the same or similar baseline noise as PICO (§ 5.5). SPT-3G has used the PICO-baselined three-color pixel design to deploy 16,000 detectors covering 90/150/220 GHz [238].

The extension to lower frequencies requires larger antennas and therefore control of film properties and lithography over larger areas. Scaling to higher frequencies requires tighter fabrication tolerances and electromagnetic wave transmission losses tend to increase due to material properties. Current anti-reflection technologies for the lenslets need to be extended with thicker and thinner layers to cover the lowest and highest frequency channels. These developments will require



Figure 5.1: SPT-3G operates a focal plane with sinuous antenna-coupled, three-band pixels with 16,000 bolometers [238]. Each pixel couples radiation to bands at 95, 150, and 220 GHz.

Table 5.1: PICO technologies can be developed to TRL 5 prior to a 2023 Phase A start using the APRA and SAT programs, requiring a total of about \$ 13M. Per NASA guidance, these costs are outside the mission cost (§ 6.5).

Task	Current status	Milestone A	Milestone B	Milestone C	Current funding	Required funding	Date TRL5 achieved
1a. Three-color arrays $\nu < 90 \text{ GHz}$	2-color lab demos $\nu > 30 \text{ GHz}$	Field demo of 30–40 GHz (2020)	Lab demos 20–90 GHz (2022)	—	APRA & SAT	\$2.5M over 4 yr (1 APRA + 1 SAT)	2022
1b. Three-color arrays $\nu > 220 \text{ GHz}$	2-color lab demos $\nu < 300 \text{ GHz}$	Field demo of 150–270 GHz (2021)	Lab demos 150–460 GHz (2022)	—	APRA & SAT	\$3.5M over 4 yr (2 SATs)	2022
2. Direct absorbing arrays $\nu > 50 \text{ GHz}$	0.1–5 THz unpolarized	Design & prototype of arrays (2021)	Lab demo of 555 GHz (2022)	Lab demo of 799 GHz (2023)	None	\$2M over 5 yr (1 SAT)	2023
3. Cosmic ray studies	250 mK w/ sources	100 mK tests with sources (2021)	Beamline tests (2023)	—	APRA & SAT	\$0.5–1M over 5 yr (part of 1 SAT)	—
4a. Fast readout electronics	MUX66 demo	Engineering and Fab of electronics (2020)	Lab demo (2021)	Field demo (2023)	No direct funds	\$4M over 5 yr (1 SAT)	2023
4b. System engineering; 128× MUX demo	MUX66 demo	Design of cables (2020)	Lab demo (2021)	Field demo (2023)	No direct funds	—	—

Table 5.2: Multiple active suborbital efforts are advancing technologies relevant to PICO.

Project	Type	Optical Coupling	ν_c [GHz]	Colors per pixel	N_{bolo}	Significance	Reference
PICO baseline	Flight		21 – 462	Three	11,796		§ 3.2.1
SPT-3G	Ground	Sinuous	90 – 220	Three	16,260	Trichroic	[238]
Advanced ACT-pol .	Ground	Horns	27 – 230	Two	3,072	Dichroic	[242]
BICEP/Keck	Ground	Antenna arrays	90 – 270	One	5,120	50 nK-deg	[243]
Berkeley, Caltech, NIST Lab		Various	30 – 270	Various	–	Band coverage	[214, 244, 245]
SPIDER	Balloon	Antenna arrays	90 – 150	One	2,400	Stable to 10 mHz	[212]

control of cleanliness and understanding of process parameters. Changes to elements in the light path will require characterization of beam properties.

The direction of polarization sensitivity of the sinuous antenna varies with frequency, thus presenting a potential source of systematic error. Over 25% bandwidth, the variation is approximately $\pm 5 \text{ deg}$ [246]. There are solutions to this in the focal-plane design, measurements, data analysis, and free parameters of the sinuous antenna geometry. A recent study found that pre-flight characterization of the effect through measurements can readily mitigate it as a source of systematic uncertainty [247]. Studies with current field demonstrations, such as with the data of SPT-3G, will be particularly important. The PICO concept is robust to any challenges in developing three-color

Table 5.3: PICO high-frequency detectors leverage development and demonstration by *Planck*, *Herschel*, and SPT.

Project	Type	Polarized	Mono-lithic	v_c [GHz]	Colors per pixel	N_{bolo}	Significance	Reference
PICO baseline	Flight	Yes	Yes	555 – 799	One	1,200		§ 3.2.2
<i>Planck</i> HFI	Flight	143–343 GHz	No	143 – 857	One	48	TRL 9 polarized	[209]
<i>Herschel</i>	Flight	No	Yes	570 – 1200	One	270	TRL 9 monolithic	[249]
SPT-SZ	Ground	No	Yes	90 – 220	One	840	Monolithic array TESs	[207]
SPT-pol-90	Ground	Yes	No	90	One	180	Dual pol absorbing TESs	[250]

pixels; § 5.5 describes options to descope to two- and one-color pixels, technologies for which the polarization sensitivity is constant as a function of frequency.

5.2 555–799 GHz bands

The baseline PICO instrument requires single-color, horn-coupled, dual-polarization, direct-absorbing bolometers from 555 to 799 GHz (§ 3.2.2). *Planck* and *Herschel* demonstrated the architecture of horns coupled to direct absorbing bolometers. Ground experiments with similar designs have deployed focal planes with hundreds of horn-coupled spiderweb bolometers, replacing the *Planck* and *Herschel* NTD-Ge thermistors with TESs, and adjusting time constants as necessary (Table 5.3). *Planck*-HFI, SPT-pol, and BICEP demonstrated dual-polarized detectors. *Herschel* and SPT-SZ demonstrated monolithic unpolarized detectors. PICO will require detectors that merge these two designs in monolithic dual-polarized arrays. Since all the components of the technology already exist, the remaining necessary development is the packaging. Filled arrays of detectors such as Backshort Under Ground (BUG) bolometers are also an option [248].

5.3 Environmental Testing

Laboratory tests and in-flight data from balloons suggest that TES bolometer arrays may be more naturally robust against cosmic rays than the individual NTD-Ge bolometers used in *Planck*. PICO will leverage lessons learned from *Planck* and ensure robust thermal sinking of detector array substrates. Cosmic-ray glitches have fast recovery times and low coincidence rates [251, 252]. Residual risk can be retired with 100 mK testing where the array heat sinking may be weaker, and beam-line tests to simulate the expected flight environment.

5.4 Multiplexing

More than ten experiments have used time-domain multiplexer (TDM) readout. SCUBA2 on JCMT has 10,000 pixels, nearly as many detectors as planned for PICO [253]. Most of these experiments have used 32-row multiplexing. Recently ACT has expanded this to 64-row multiplexing [213].

PICO’s sensitivity requirements dictate the use of 13,000 transition-edge-sensor bolometers and a multiplexed system. Our baseline design is to use TDM readout with 128 switched rows per readout column (TDM-128×). The leap to TDM-128× requires:

- development of fast-switched room temperature electronics; and
- system engineering of room temperature to cryogenic row-select cabling to ensure sufficiently fast row-switch settling times.

The historical row revisit rate for bolometric instruments using 32× TDM has been 25 kHz [e.g.,

[203](#). However, X-ray instruments using TDM routinely switch between rows at 6.25 MHz [\[254\]](#). The PICO baseline assumes a 6.25 MHz switch rate and TDM- $128\times$, which dictates a row-revisit rate of 48.8 kHz. To limit aliased noise, PICO implements low-pass filters in each readout channel with a bandwidth of 6 kHz, dictated by detector stability considerations and the required ~ 1 kHz signal bandwidth. With these parameters and using the same TDM multiplexer SQUID design, the increased total noise due to aliasing is less than 15 % and is included in our detector noise budget. The system engineering study will culminate in a demonstration of TDM- $128\times$ SQUID aliased noise below PICO detector sensitivity requirements.

5.5 Technology Desscopes

A descope from three-color sinuous antenna/lenslet-coupled pixels to two-color horn-coupled, or to single color antenna-array pixels remains a viable alternative should the three-color technology not mature as planned. In both alternative options, bands above 555 GHz are the same as the baseline. For the lower frequencies, the two-color horn-coupled pixel option contains 8,840 detectors and has 19 colors. Because horns have a 2.3 : 1 bandwidth, each of the two bands in a pixel has 35 % bandwidth (compared to the baseline 25 %), which compensates for pixel count, resulting in $0.61 \mu\text{K}_{\text{CMB}}$ arcmin aggregate CBE map depth. This is the same as the three-color CBE map depth, and affords the same 40 % margin relative to the $0.87 \mu\text{K}_{\text{CMB}}$ arcmin baseline requirement (Table [3.2](#)). Detailed analysis would be performed to assess the impact of the coarser spectral resolution on signal component separation. Single color antenna-array pixels can have higher packing density than the other two architectures. This option has 6,540 detectors, 21 colors, each with 30 % bandwidth, and a noise level of $0.74 \mu\text{K}_{\text{CMB}}$ arcmin, leaving only 17% noise margin relative to the requirement.

5.6 Enhancing Technologies

The following technologies are neither required nor assumed by the PICO baseline concept. However, they represent opportunities to extend scientific capabilities or simplify engineering.

PICO baselines TDM readout because of its relative maturity and demonstrated sensitivity and stability in relevant science missions. Lab tests of frequency-domain multiplexing (FDM) give comparable performance with higher multiplexing factors and lower thermal loads on cryogenic stages relative to TDM, but with higher ambient temperature power consumption. Suborbital experiments such as SPT-3G are using FDM to read out focal planes comparable in size to PICO.

Microwave frequency SQUID multiplexing can increase the multiplexing density and reduce the number of wires between the 4 K and ambient temperature stages [\[255, 256\]](#). Kinetic inductance detectors and Thermal KIDs can further reduce the wire count, obviate the need for SQUID-based amplifiers, and simplify integration by integrating the multiplexing function on the same substrate as the detectors [\[257–259\]](#). The cost to develop these technologies is \$3–4M/year, with a high chance of reaching TRL-5 before Phase A.

6 Project Management, Heritage, Risk, and Cost

6.1 PICO Study Participants

The PICO study was open to the entire mm/sub-mm science community. Seven working groups were led by members of PICO’s Executive Committee, which had a telephone conference weekly under the leadership of PI Shaul Hanany. Several of the working groups also had weekly telecon

conferences. More than 60 people participated in-person in each of two community workshops (November 2017 and May 2018). This report has contributions from 82 authors, and it has been endorsed by additional 131 members of the community. The full list of authors and endorsers is on page i.

The PICO engineering concept definition package was generated by Team X.⁹ The Team X study was supported by inputs from a JPL engineering team and Lockheed Martin.

6.2 Project Management Plan

PICO benefits from the experience of predecessor missions such as *Planck* and *WMAP*, as well as many years of investment in technology development and a multitude of suborbital experiments. In addition to demonstrated science and engineering capabilities, this heritage has developed a community of people with the expertise required to field a successful mission.

This study assumes mission management by JPL with a Principal Investigator leading a single science team. A Project Manager provides project oversight for schedule, budget, and deliverables. A Project Systems Engineer leads systems engineering activities and serves as the Engineering Technical Authority. A Mission Assurance Manager serves as the Independent Technical Authority. The PICO mission development schedule is shown in Fig. 6.1.

	FY24	FY25	FY26	FY27	FY28	FY29	FY30	FY31	FY32	FY33	FY34	FY35
CY 2023	CY 2024	CY 2025	CY 2026	CY 2027	CY 2028	CY 2029	CY 30	CY 31	CY 32	CY 33	CY 34	
PH A (12 mths)	PH B (12 mths)	PHASE C (22 mths)	PHASE D(18 mths)		PHASE E (5 yrs)							F 4 mths
♦ 10/23 KDP-A	♦ 10/24 KDP-B	♦10/25 KDP-C		♦ 8/27 KDP-D		♦ 2/29 PLAR (Start of Ph E)						KDP-F 2/34 ♦
Reviews	10/25 PDR ♦		♦ 7/26 CDR	♦ 7/27 ARR		Launch 1/29★						

Figure 6.1: The PICO baseline schedule is based on historical actuals from similarly-sized missions such as Juno and SMAP. Per NASA direction, Probe studies assume a Phase A start in October 2023.

Probes are medium-class missions, similar in cost scope to NASA’s New Frontiers missions, which are Category 1 and Risk Classification A or B, with Phase A–D costs capped at ~ \$850M (not including the launch vehicle). JPL is well-prepared to manage Probe missions, having managed the Juno New Frontiers mission (launched 2011) and also the development of the medium-class *Spitzer* Space Telescope (launched 2003). JPL delivered the bolometric detectors for the *Planck* HFI instrument (launched 2009). Presently, JPL is managing NEOCam, a Discovery class infrared space telescope.

The PICO spacecraft provider will be selected during mission formulation. Multiple organizations are capable of providing a spacecraft bus to meet PICO’s requirements. Lockheed Martin contributed to the PICO concept study, leveraging their experience with New Frontiers missions Juno and OSIRIS-REx.

6.3 Heritage

The technical heritage for PICO traces to multiple missions. Because PICO observes in the mm/sub-mm regime, the surface accuracy requirement for the reflectors is relatively easy to meet. PICO’s reflectors are similar to *Planck*’s, but somewhat larger (270 cm × 205 cm primary versus 189 cm × 155 cm) [260]. *Herschel* observed at shorter wavelengths that required higher surface accuracy and had a larger reflector (350 cm diameter primary) [261].

⁹ Team X is JPL’s concurrent design facility.

The heritage of the PICO detectors and readout electronics (which are described in § 3.2, § 3.3) is described in § 5.

PICO’s detectors are cooled by a cADR (§ 3.4.1) with requirements that are within the capabilities of current ADRs developed by Goddard Space Flight Center. These systems have been applied to several JAXA missions, including *Hitomi* [226]. PICO’s 4 K cryocooler (§ 3.4.2) is a direct extension of the JWST MIRI design [227, 228]. PICO benefits from a simpler and more reliable implementation of the J-T system than was required for MIRI, in that no deployment of cooling lines is required, and all flow valving is performed on the warm spacecraft. Cooling multiple independent points with a J-T loop has been demonstrated on *Planck* with the JPL-supplied 18 K cooler [262]. Structures similar to PICO’s V-groove radiator assembly (§ 3.4.3) are a standard approach for passive cooling, and were first described more than thirty years ago [263]. We baselined a simple honeycomb material construction like that successfully flown by *Planck* [262, 264].

Most requirements on the PICO spacecraft are well within typical ranges and can be met with standard high heritage systems (§ 4.3). PICO’s spin architecture and data volume requirements are less typical, and are discussed below.

The spin system is less demanding than the successful SMAP spin system. The PICO spin rate is 1 rpm, and the mission requires $\sim 220 \text{ N m s}$ of spin angular momentum cancellation (§ 4.3.1). Only data and power lines pass across the spin interface between the spinning and non-spinning modules (Fig. 3.2). With SMAP, a 6-m instrument antenna is spun at 14.6 rpm, and it requires 359 N m s of spin angular momentum cancellation [265]. Data and power successfully pass across the spin interface.

Though PICO’s data volume is notable by current standards, it is already surpassed by missions in development. The mission produces 6.1 Tb/day of raw data which is compressed to 1.5 Tb/day (§ 3.3). Data downlinks occur daily, but we baseline storage of 3 days of (compressed) data to mitigate missed telecom passes. This requires 4.5 Tb of onboard storage, in family with the 3.14 Tb solid-state recorder currently in use by Landsat 8 and much smaller than the 12 Tb flash memory planned for NISAR [266]. The baseline 150 Mb/s Ka-band data downlink is an existing DSN catalog service [236]. The baseline mission generates 2,200 Tb of raw (uncompressed) data per year, less than the 6,800 Tb/year currently returned by Landsat 8 and 9,300 Tb/yr planned by NISAR [266].

6.4 Risk Assessment

6.4.1 Pre-Mission Risks

Technology development (§ 5) is performed prior to the beginning of mission development, and is outside of the mission cost (per NASA direction), so associated risks do not represent threats to the cost of mission development. Rather, these technology development risks affect the availability of components for the baseline mission. A technology-related mission descope is described in § 5.5.

6.4.2 Development Risks

PICO’s healthy contingencies, margins, and reserves provide flexibility to address risks realized during mission development. PICO carries $> 40\%$ instrument sensitivity margin (Table 3.2), $> 100\%$ heat lift margin (Table 3.3), 43% system power contingency, 31% payload mass contingency, and 25% spacecraft mass contingency. The Falcon 9 launch capability (assuming ocean recovery) exceeds PICO’s total launch mass (including contingency) by a 50% margin. The PICO budget includes 30% cost reserves for Phases A–D (§ 6.5).

Mitigations for the risks identified during this study are described below.

- Thermal risk can be mitigated through extensive thermal modeling and review in Phase A, and design for early test verification.
- Risks associated with the instrument spin architecture can be mitigated by engaging JPL engineers who were involved in the SMAP mission.
- Detector delivery schedule risk can be mitigated by beginning fabrication early in the project life cycle and fabricating a generous number of detector wafers to ensure adequate yield. Multiple institutions (including, for example, JPL, GSFC, NIST, and ANL) would be capable of producing the PICO detectors.
- Risks associated with the integration and test of a cryogenic instrument can be mitigated through advanced planning and allocation of appropriate schedule and schedule margin.

6.4.3 Operations Risks

The PICO design meets the requirements associated with the NASA Class B risk classification. For Class B missions, essential spacecraft and instrument functions are typically fully redundant. This increases mission cost, but significantly reduces the risk of mission failure.

The PICO mission utilizes a single instrument with a single observing mode mapping the sky using a repetitive survey pattern. The mission does not require any time-critical activities. The observatory fits into the launch vehicle fairing in its operational configuration, therefore no hardware deployments are required. Because PICO observes at long wavelengths, the telescope does not require a dust cover (nor the mission-critical cover release).

The spacecraft incorporates a fault protection system for anomaly detection and resolution. The Sun-pointed, command receptive, thermally stable safe-mode attitude allows ground intervention for fault resolution without time constraints. PICO’s high degree of hardware redundancy and onboard fault protection ensure spacecraft safety in the event of unforeseen failures and faults.

As described in § 2.7 and § 2.8, pre-Phase A simulation software maturation is recommended to mitigate the challenges associated with foreground separation and systematics control.

Table 6.1: Detailed breakdown of Team X and PICO Team cost estimates (in FY18\$). Costs are based on the schedule in Fig. 6.1, which includes 5 years of operations.

Work Breakdown Structure (WBS) elements	Team X	PICO
Development Cost (Phases A–D)	\$ 724M	\$ 634–677M
1.0, 2.0, 3.0 Management, Systems Engineering, and Mission Assurance	\$ 54M	\$ 47– 50M
4.0 Science		\$ 19M
5.0 Payload System		\$ 168M
6.0 Flight System	\$ 248M	\$ 210–240M
10.0 Assembly, Test, and Launch Operations (ATLO)	\$ 24M	
7.0 Mission Operations Preparation		\$ 16M
9.0 Ground Data Systems		\$ 21M
12.0 Mission and Navigation Design		\$ 7M
Development Reserves (30%)	\$167M	\$ 146–156M
Operations Cost (Phase E)		\$ 84M
1.0 Management		\$ 6M
4.0 Science		\$ 20M
7.0 Mission Operations		\$ 34M
9.0 Ground Data Systems		\$ 14M
Operations Reserves (13%)		\$ 10M
Launch Vehicle Cost to mitigate the challenges associated with fore- ground separation and systematics control		\$ 150M
Total Cost	\$ 958M	\$ 868–911M

6.5 Mission Cost

We estimate PICO’s total Phase A–E lifecycle cost between \$870M and \$960M, including the \$150M allocation for the Launch Vehicle (per NASA direction). These cost estimates include 30 %

reserves for development (Phases A–D) and 13 % reserves for operations (Phase E). Pre-Phase-A technology maturation will be accomplished through the normal APRA and SAT processes, and is not included in the mission cost.

Table 6.1 shows the mission cost breakdown, including the JPL Team X¹⁰ cost estimate, as well as the PICO team cost estimate. Team X estimates are generally model-based, and were generated after a series of instrument and mission-level studies. Their accuracy is commensurate with the level of understanding typical to Pre-Phase-A concept development. They do not constitute an implementation or cost commitment on the part of JPL or Caltech.

The PICO team has adopted the Team X estimates, but also obtained a parametrically estimated cost range for the Flight System (WBS 6) and Assembly, Test, and Launch Operations (ATLO, WBS 7) from Lockheed Martin Corporation to represent the cost benefits that might be realized by working with an industry partner. After adding estimated JPL overhead and Team X estimated V-groove assembly costs (not included in the Lockheed estimate), the PICO team cost is in-family with but lower than the Team X cost.

Management, Systems Engineering, and Mission Assurance (WBS 1–3) development costs scale linearly with the WBS 4–12 development costs in the Team X model, and are adjusted accordingly in the PICO team estimate. Science team (WBS 4) costs are assessed by Team X based on PICO science team estimates of the numbers and types of contributors and meetings required for each year of PICO mission development and operations. These workforce estimates are informed by recent experience with the *Planck* mission.

Payload system (WBS 5) costs are discussed in detail in § 6.5.1. PICO’s spacecraft (WBS 6) cost reflects a robust Class B architecture (§ 4.3). Mission-critical elements are redundant. Appropriate flight spares, engineering models and prototypes are budgeted. The V-groove assembly (§ 3.4.3) is costed in WBS 6. Mission operations (WBS 7), Ground Data Systems (WBS 9), and Mission Navigation and Design (WBS 12) costs reflect a relatively simple concept of operations (§ 4.1). PICO has a single instrument and a single science observing mode. It surveys the sky continuously using a pre-planned repetitive survey pattern. Orbit maintenance activities are simple and infrequent.

6.5.1 Payload Cost

The PICO payload consists of a single instrument: an imaging polarimeter. Payload costs are tabulated in Table 6.2.

The superconducting detectors require sub-kelvin cooling to operate. The active cooling system (the 0.1 K cADR and 4 K cryocooler, § 3.4.1 and § 3.4.2) comprises nearly half of the payload cost. The cADR cost for this study is an estimate from Goddard Space Flight Center, and assumes the provision of both a flight model and an engineering model. GSFC has produced ADRs for multiple spaceflight missions. The 4 K cryocooler cost for this study is based on the NASA Instrument Cost Model (NICM) VIII CER Cryocooler model [267], assuming a commercial build. PICO benefits greatly from recent and ongoing investment by commercial suppliers of 4 K coolers (as described in § 3.4.2). Team X used NICM VIII to model the cost of the focal plane and dual string readout electronics (§ 3.2, § 3.3). Team X estimated the telescope cost using the Stahl model [268].

Table 6.2: Detailed breakdown of PICO instrument costs.

Instrument Elements	Cost
Management, Systems Eng., Assurance	\$ 18M
4 K Cooler and 0.1 K cADR	\$ 71M
Focal plane and electronics	\$ 27M
Mechanical, Thermal, Software	\$ 17M
Telescope	\$ 6M
Instrument integration and test	\$ 29M
Total Instrument Cost	\$ 168M

This study is based on the NASA Instrument Cost Model (NICM) VIII CER Cryocooler model [267], assuming a commercial build. PICO benefits greatly from recent and ongoing investment by commercial suppliers of 4 K coolers (as described in § 3.4.2). Team X used NICM VIII to model the cost of the focal plane and dual string readout electronics (§ 3.2, § 3.3). Team X estimated the telescope cost using the Stahl model [268].

The telescope is not a major cost driver, primarily because the reflectors only need to be diffraction limited at 330 μm (900 GHz) (§ 3.1).

Based on JPL experience, 18 % of the instrument cost is allocated for integration and testing (I&T). This includes I&T of the flight focal-plane assembly with the flight cADR and then I&T of the complete instrument including the focal-plane assembly, reflectors, structures, and coolers (§ 3.5). I&T of the instrument with the spacecraft is costed in WBS 10 (ATLO).

NASA Standard Template Cost Table

2020 Astrophysical Decadal Survey - Probe Mission Preparatory Study Master Equipment List Based Parametric Total Lifecycle Cost Estimate

Mission Name / Acronym: PICO
Cost Estimator: JPL Team X
Date of Cost Estimate: October 9, 2018
Cost Estimate Based On: Final Master Equipment List

<u>PROJECT PHASE</u>	<u>COST [FY18 \$M]</u>
Phase A	(see Note 1)
Phases B-D	Mgmt, SE, MA \$54
	Science \$19
	Telescope \$6
	Instrument \$162
	Spacecraft, including ATLO \$272
	MOS/GDS \$44
	Launch Vehicle and Services \$150
	Reserves \$167
Total Cost Phases B-D \$874	
Phase E-F	Operations \$74
	Reserves \$10
	Total Cost Phases E-F \$84
TOTAL LIFECYCLE COST \$958	

Notes:

- Team X estimates costs for Phase A-D. A break out of Phase A cost is not available. In this table, Phase A costs are included in Phase B-D.
- This parametric cost estimate is based on the Probe's Master Equipment List derived from the Final Engineering Concept Definition Package that accurately reflects the mission described in the Probe's Final Report. This estimate is to be used only for non-binding rough order of magnitude planning purposes.
- Team X estimates are generally model-based, and were generated after a series of instrument and mission level studies. Their accuracy is commensurate with the level of understanding typical to Pre-Phase-A concept development. They do not constitute an implementation or cost commitment on the part of JPL or Caltech.

References

- [1] S. Hanany, M. Alvarez, E. Artis *et al.*, “PICO: Probe of Inflation and Cosmic Origins,” *arXiv e-prints*, Feb. 2019. <https://ui.adsabs.harvard.edu/abs/2019arXiv190210541H>
- [2] National Research Council, *New Worlds, New Horizons in Astronomy and Astrophysics*. Washington, DC: The National Academies Press, 2010. <https://www.nap.edu/catalog/12951/new-worlds-new-horizons-in-astronomy-and-astrophysics>
- [3] L. M. Krauss and F. Wilczek, “Using cosmology to establish the quantization of gravity,” *Phys. Rev. D.*, vol. 89, no. 4, p. 047501, Feb. 2014. <http://adsabs.harvard.edu/abs/2014PhRvD..89d7501K>
- [4] Planck Collaboration, N. Aghanim, Y. Akrami *et al.*, “Planck 2018 results. VI. Cosmological parameters,” *arXiv e-prints*, Jul. 2018. <http://adsabs.harvard.edu/abs/2018arXiv180706209P>
- [5] Planck Collaboration, P. A. R. Ade, N. Aghanim *et al.*, “Planck 2015 results. XVII. Constraints on primordial non-Gaussianity,” *Astron. Astrophys.*, vol. 594, p. A17, Sep. 2016. <https://ui.adsabs.harvard.edu/#abs/2016A&A...594A..17P>
- [6] The Simons Observatory Collaboration, P. Ade, J. Aguirre *et al.*, “The Simons Observatory: Science goals and forecasts,” *ArXiv e-prints*, Aug. 2018. <http://adsabs.harvard.edu/abs/2018arXiv180807445T>
- [7] T. R. Slatyer, N. Padmanabhan, and D. P. Finkbeiner, “Cmb constraints on wimp annihilation: Energy absorption during the recombination epoch,” *Physical Review D (Particles, Fields, Gravitation, and Cosmology)*, vol. 80, no. 4, p. 043526, 2009. <http://link.aps.org/abstract/PRD/v80/e043526>
- [8] S. Galli, F. Iocco, G. Bertone, and A. Melchiorri, “CMB constraints on dark matter models with large annihilation cross section,” *Phys. Rev. D.*, vol. 80, no. 2, pp. 023505–+, Jul. 2009. <http://adsabs.harvard.edu/abs/2009PhRvD..80b3505G>
- [9] G. Hütsi, A. Hektor, and M. Raidal, “Constraints on leptonically annihilating dark matter from reionization and extragalactic gamma background,” *Astron. Astrophys.*, vol. 505, pp. 999–1005, Oct. 2009. <http://adsabs.harvard.edu/abs/2009A%26A...505..999H>
- [10] G. Hütsi, J. Chluba, A. Hektor, and M. Raidal, “WMAP7 and future CMB constraints on annihilating dark matter: implications for GeV-scale WIMPs,” *Astron. Astrophys.*, vol. 535, p. A26, Nov. 2011. <http://adsabs.harvard.edu/abs/2011A%26A...535A..26H>
- [11] M. S. Madhavacheril, N. Sehgal, and T. R. Slatyer, “Current dark matter annihilation constraints from CMB and low-redshift data,” *Phys. Rev. D.*, vol. 89, no. 10, p. 103508, May 2014. <http://adsabs.harvard.edu/abs/2014PhRvD..89j3508M>
- [12] D. Green, P. D. Meerburg, and J. Meyers, “Aspects of Dark Matter Annihilation in Cosmology,” *ArXiv e-prints*, Apr. 2018. <http://adsabs.harvard.edu/abs/2018arXiv180401055G>
- [13] L. M. Widrow, “Origin of galactic and extragalactic magnetic fields,” *Reviews of Modern Physics*, vol. 74, pp. 775–823, 2002. <http://adsabs.harvard.edu/abs/2002RvMP..74..775W>
- [14] L. M. Widrow, D. Ryu, D. R. G. Schleicher, K. Subramanian, C. G. Tsagas, and R. A. Treumann, “The First Magnetic Fields,” *Space Science Reviews*, vol. 166, pp. 37–70, May 2012. <http://adsabs.harvard.edu/abs/2012SSRv..166..37W>
- [15] R. M. Athreya, V. K. Kapahi, P. J. McCarthy, and W. van Breugel, “Large rotation measures in radio galaxies at $Z > 2$,” *Astron. Astrophys.*, vol. 329, pp. 809–820, Jan. 1998. <http://adsabs.harvard.edu/abs/1998A%26A...329..809A>
- [16] D. Grasso and H. R. Rubinstein, “Magnetic fields in the early Universe,” *Physics Reports*, vol. 348, pp. 163–266, Jul. 2001. <http://adsabs.harvard.edu/abs/2001PhR...348..163G>
- [17] T. Vachaspati, “Magnetic fields from cosmological phase transitions,” *Physics Letters B*, vol. 265, pp. 258–261, Aug. 1991. <http://adsabs.harvard.edu/abs/1991PhLB..265..258V>
- [18] M. S. Turner and L. M. Widrow, “Inflation-produced, large-scale magnetic fields,” *Phys. Rev. D.*, vol. 37, pp. 2743–2754, May 1988. <http://adsabs.harvard.edu/abs/1988PhRvD..37.2743T>
- [19] B. Ratra, “Cosmological ‘seed’ magnetic field from inflation,” *Ap. J. Lett.*, vol. 391, pp. L1–L4, May 1992. <http://adsabs.harvard.edu/abs/1992ApJ...391L...1R>
- [20] A. Díaz-Gil, J. García-Bellido, M. García Pérez, and A. González-Arroyo, “Magnetic Field Production during Preheating at the Electroweak Scale,” *Physical Review Letters*, vol. 100, no. 24, p. 241301, Jun. 2008. <http://adsabs.harvard.edu/abs/2008PhRvL..100x1301D>

- [21] N. Barnaby, R. Namba, and M. Peloso, “Observable non-Gaussianity from gauge field production in slow roll inflation, and a challenging connection with magnetogenesis,” *Phys. Rev. D.*, vol. 85, no. 12, p. 123523, Jun. 2012. <http://adsabs.harvard.edu/abs/2012PhRvD..85l3523B>
- [22] A. J. Long, E. Sabancilar, and T. Vachaspati, “Leptogenesis and primordial magnetic fields,” *JCAP*, vol. 2, p. 036, Feb. 2014. <http://adsabs.harvard.edu/abs/2014JCAP..02..036L>
- [23] R. Durrer and A. Neronov, “Cosmological magnetic fields: their generation, evolution and observation,” *Astronomy and Astrophysics Review*, vol. 21, p. 62, Jun. 2013. <http://adsabs.harvard.edu/abs/2013A%26ARv..21...62D>
- [24] Planck Collaboration, P. A. R. Ade, N. Aghanim *et al.*, “Planck 2015 results. XIX. Constraints on primordial magnetic fields,” *Astron. Astrophys.*, vol. 594, p. A19, Sep. 2016. <http://adsabs.harvard.edu/abs/2016A%26A...594A..19P>
- [25] K. E. Kunze and E. Komatsu, “Constraints on primordial magnetic fields from the optical depth of the cosmic microwave background,” *ArXiv:1501.00142*, Dec. 2015. <http://adsabs.harvard.edu/abs/2015arXiv150100142K>
- [26] J. Chluba, D. Paoletti, F. Finelli, and J.-A. Rubino-Martin, “Effect of primordial magnetic fields on the ionization history,” *ArXiv:1503.04827*, Mar. 2015. <http://adsabs.harvard.edu/abs/2015arXiv150304827C>
- [27] A. Zucca, Y. Li, and L. Pogosian, “Constraints on primordial magnetic fields from Planck data combined with the South Pole Telescope CMB B -mode polarization measurements,” *Phys. Rev. D.*, vol. 95, no. 6, p. 063506, Mar. 2017. <http://adsabs.harvard.edu/abs/2017PhRvD..95f3506Z>
- [28] A. Kosowsky and A. Loeb, “Faraday Rotation of Microwave Background Polarization by a Primordial Magnetic Field,” *Ap. J.*, vol. 469, pp. 1–+, Sep. 1996. <http://adsabs.harvard.edu/abs/1996ApJ...469....1K>
- [29] N. Oppermann, H. Junklewitz, G. Robbers *et al.*, “An improved map of the Galactic Faraday sky,” *Astron. Astrophys.*, vol. 542, p. A93, Jun. 2012. <http://adsabs.harvard.edu/abs/2012A%26A...542A..93O>
- [30] S. De, L. Pogosian, and T. Vachaspati, “CMB Faraday rotation as seen through the Milky Way,” *Phys. Rev. D.*, vol. 88, no. 6, p. 063527, Sep. 2013. <http://adsabs.harvard.edu/abs/2013PhRvD..88f3527D>
- [31] L. Pogosian, “Searching for primordial magnetism with multifrequency cosmic microwave background experiments,” *MNRAS*, vol. 438, pp. 2508–2512, Mar. 2014. <http://adsabs.harvard.edu/abs/2014MNRAS.438.2508P>
- [32] K. Freese, J. A. Frieman, and A. V. Olinto, “Natural inflation with pseudo Nambu-Goldstone bosons,” *Physical Review Letters*, vol. 65, pp. 3233–3236, Dec. 1990. <http://adsabs.harvard.edu/abs/1990PhRvL..65.3233F>
- [33] J. A. Frieman, C. T. Hill, A. Stebbins, and I. Waga, “Cosmology with Ultralight Pseudo Nambu-Goldstone Bosons,” *Physical Review Letters*, vol. 75, pp. 2077–2080, Sep. 1995. <http://adsabs.harvard.edu/abs/1995PhRvL..75.2077F>
- [34] S. M. Carroll, “Quintessence and the Rest of the World: Suppressing Long-Range Interactions,” *Physical Review Letters*, vol. 81, pp. 3067–3070, Oct. 1998. <http://adsabs.harvard.edu/abs/1998PhRvL..81.3067C>
- [35] N. Kaloper and L. Sorbo, “Of pNGB quiScript Ntessence,” *JCAP*, vol. 4, p. 007, Apr. 2006. <http://adsabs.harvard.edu/abs/2006JCAP..04..007K>
- [36] C. R. Contaldi, J. Magueijo, and L. Smolin, “Anomalous Cosmic-Microwave-Background Polarization and Gravitational Chirality,” *Phys. Rev. Lett.*, vol. 101, p. 141101, Oct. 2008. <https://ui.adsabs.harvard.edu/#abs/2008PhRvL.101n1101C>
- [37] V. Gluscevic and M. Kamionkowski, “Testing parity-violating mechanisms with cosmic microwave background experiments,” *Phys. Rev. D.*, vol. 81, no. 12, p. 123529, Jun. 2010. <http://adsabs.harvard.edu/abs/2010PhRvD..81l3529G>
- [38] D. Harari and P. Sikivie, “Effects of a Nambu-Goldstone boson on the polarization of radio galaxies and the cosmic microwave background,” *Physics Letters B*, vol. 289, pp. 67–72, Sep. 1992. <http://adsabs.harvard.edu/abs/1992PhLB..289...67H>
- [39] S. M. Carroll, G. B. Field, and R. Jackiw, “Limits on a Lorentz- and parity-violating modification of electrodynamics,” *Phys. Rev. D.*, vol. 41, pp. 1231–1240, Feb. 1990. <http://adsabs.harvard.edu/abs/1990PhRvD..41.1231C>
- [40] M. Kamionkowski, “How to Derotate the Cosmic Microwave Background Polarization,” *Physical Review Letters*, vol. 102, no. 11, p. 111302, Mar. 2009. <http://adsabs.harvard.edu/abs/2009PhRvL.102k1302K>
- [41] V. Gluscevic, M. Kamionkowski, and A. Cooray, “Derotation of the cosmic microwave background polarization: Full-sky formalism,” *Phys. Rev. D.*, vol. 80, no. 2, p. 023510, Jul. 2009. <http://adsabs.harvard.edu/abs/2009PhRvD..80...23510G>

- //adsabs.harvard.edu/abs/2009PhRvD..80b3510G
- [42] V. Gluscevic, D. Hanson, M. Kamionkowski, and C. M. Hirata, “First CMB constraints on direction-dependent cosmological birefringence from WMAP-7,” *Phys. Rev. D.*, vol. 86, no. 10, p. 103529, Nov. 2012. <http://adsabs.harvard.edu/abs/2012PhRvD..86j3529G>
- [43] Planck Collaboration, N. Aghanim, M. Ashdown *et al.*, “Planck intermediate results. XLIX. Parity-violation constraints from polarization data,” *Astron. Astrophys.*, vol. 596, p. A110, Dec. 2016. <http://adsabs.harvard.edu/abs/2016A%26A...596A.110P>
- [44] M. Pospelov, A. Ritz, and C. Skordis, “Pseudoscalar Perturbations and Polarization of the Cosmic Microwave Background,” *Physical Review Letters*, vol. 103, no. 5, p. 051302, Jul. 2009. <http://adsabs.harvard.edu/abs/2009PhRvL.103e1302P>
- [45] BICEP2 and Keck Array Collaboration, P. A. R. Ade, Z. Ahmed *et al.*, “BICEP2 / Keck Array IX: New bounds on anisotropies of CMB polarization rotation and implications for axionlike particles and primordial magnetic fields,” *Phys. Rev. D.*, vol. 96, no. 10, p. 102003, Nov. 2017. <http://adsabs.harvard.edu/abs/2017PhRvD..96j2003B>
- [46] P. Svrcek and E. Witten, “Axions in string theory,” *Journal of High Energy Physics*, vol. 6, p. 051, Jun. 2006. <http://adsabs.harvard.edu/abs/2006JHEP..06..051S>
- [47] Planck Collaboration, N. Aghanim, Y. Akrami *et al.*, “Planck 2018 results. VI. Cosmological parameters,” *ArXiv e-prints*, Jul. 2018. <http://adsabs.harvard.edu/abs/2018arXiv180706209P>
- [48] R. A. Monsalve, A. E. E. Rogers, J. D. Bowman, and T. J. Mozdzen, “Results from EDGES High-band. I. Constraints on Phenomenological Models for the Global 21 cm Signal,” *Ap. J.*, vol. 847, p. 64, Sep. 2017. <http://adsabs.harvard.edu/abs/2017ApJ...847...64M>
- [49] X. Fan, M. A. Strauss, R. H. Becker *et al.*, “Constraining the Evolution of the Ionizing Background and the Epoch of Reionization with $z \sim 6$ Quasars. II. A Sample of 19 Quasars,” *Astronomical Journal*, vol. 132, pp. 117–136, Jul. 2006. <http://adsabs.harvard.edu/abs/2006AJ....132..117F>
- [50] Planck Collaboration, R. Adam, N. Aghanim *et al.*, “Planck intermediate results. XLVII. Planck constraints on reionization history,” *Astron. Astrophys.*, vol. 596, p. A108, Dec. 2016. <http://adsabs.harvard.edu/abs/2016A%26A...596A.108P>
- [51] V. Miranda, A. Lidz, C. H. Heinrich, and W. Hu, “CMB signatures of metal-free star formation and Planck 2015 polarization data,” *MNRAS*, vol. 467, pp. 4050–4056, Jun. 2017. <http://adsabs.harvard.edu/abs/2017MNRAS.467.4050M>
- [52] E. Calabrese, R. Hložek, N. Battaglia *et al.*, “Precision epoch of reionization studies with next-generation CMB experiments,” *JCAP*, vol. 8, p. 010, Aug. 2014. <http://adsabs.harvard.edu/abs/2014JCAP..08..010C>
- [53] K. M. Smith and S. Ferraro, “Detecting Patchy Reionization in the Cosmic Microwave Background,” *Physical Review Letters*, vol. 119, no. 2, p. 021301, Jul. 2017. <http://adsabs.harvard.edu/abs/2017PhRvL.119b1301S>
- [54] C. Dvorkin and K. M. Smith, “Reconstructing patchy reionization from the cosmic microwave background,” *Phys. Rev. D.*, vol. 79, no. 4, p. 043003, Feb. 2009. <http://adsabs.harvard.edu/abs/2009PhRvD..79d3003D>
- [55] Planck Collaboration, N. Aghanim, Y. Akrami *et al.*, “Planck 2018 results. VIII. Gravitational lensing,” *ArXiv e-prints*, Jul. 2018. <http://adsabs.harvard.edu/abs/2018arXiv180706210P>
- [56] U. Seljak, “Extracting Primordial Non-Gaussianity without Cosmic Variance,” *Physical Review Letters*, vol. 102, no. 2, p. 021302, Jan. 2009. <http://adsabs.harvard.edu/abs/2009PhRvL.102b1302S>
- [57] M. Schmittfull and U. Seljak, “Parameter constraints from cross-correlation of CMB lensing with galaxy clustering,” *Phys. Rev. D.*, vol. 97, no. 12, p. 123540, Jun. 2018. <http://adsabs.harvard.edu/abs/2018PhRvD..97l3540S>
- [58] LSST Science Collaboration, P. A. Abell, J. Allison *et al.*, “LSST Science Book, Version 2.0,” *arXiv e-prints*, Dec. 2009. <http://adsabs.harvard.edu/abs/2009arXiv0912.0201L>
- [59] B. Yu, R. Z. Knight, B. D. Sherwin, S. Ferraro, L. Knox, and M. Schmittfull, “Towards Neutrino Mass from Cosmology without Optical Depth Information,” *arXiv e-prints*, Sep. 2018. <http://adsabs.harvard.edu/abs/2018arXiv180902120Y>
- [60] J. S. Dunlop, “Observing the First Galaxies,” in *The First Galaxies*, ser. Astrophysics and Space Science Library, T. Wiklind, B. Mobasher, and V. Bromm, Eds., vol. 396, 2013, p. 223. <http://adsabs.harvard.edu/abs/2013ASSL..396..223D>
- [61] M. Schmittfull and U. Seljak, “Parameter constraints from cross-correlation of CMB lensing with galaxy

- clustering,” *Phys. Rev. D.*, vol. 97, no. 12, p. 123540, Jun. 2018. <http://adsabs.harvard.edu/abs/2018PhRvD..97l3540S>
- [62] Y. Ono, M. Ouchi, Y. Harikane *et al.*, “Great Optically Luminous Dropout Research Using Subaru HSC (GOLDRUSH). I. UV luminosity functions at $z = 4\text{-}7$ derived with the half-million dropouts on the 100 deg^2 sky,” *Publications of the Astronomical Society of Japan*, vol. 70, p. S10, Jan. 2018. <http://adsabs.harvard.edu/abs/2018PASJ...70S..10O>
- [63] Y. Harikane, M. Ouchi, Y. Ono *et al.*, “GOLDRUSH. II. Clustering of galaxies at $z = 4\text{-}6$ revealed with the half-million dropouts over the 100 deg^2 area corresponding to 1 Gpc^3 ,” *Publications of the Astronomical Society of Japan*, vol. 70, p. S11, Jan. 2018. <http://adsabs.harvard.edu/abs/2018PASJ...70S..11H>
- [64] J.-B. Melin, J. G. Bartlett, Z.-Y. Cai, G. De Zotti, J. Delabrouille, M. Roman, and A. Bonaldi, “Dust in galaxy clusters: Modeling at millimeter wavelengths and impact on Planck cluster cosmology,” *Astron. Astrophys.*, vol. 617, p. A75, Sep. 2018.
- [65] E. J. Baxter, R. Keisler, S. Dodelson *et al.*, “A Measurement of Gravitational Lensing of the Cosmic Microwave Background by Galaxy Clusters Using Data from the South Pole Telescope,” *Ap. J.*, vol. 806, p. 247, Jun. 2015. <http://adsabs.harvard.edu/abs/2015ApJ...806..247B>
- [66] M. Madhavacheril, N. Sehgal, R. Allison *et al.*, “Evidence of lensing of the cosmic microwave background by dark matter halos,” *Phys. Rev. Lett.*, vol. 114, p. 151302, Apr 2015. <https://link.aps.org/doi/10.1103/PhysRevLett.114.151302>
- [67] Planck Collaboration, P. A. R. Ade, N. Aghanim *et al.*, “Planck 2015 results. XXIV. Cosmology from Sunyaev-Zeldovich cluster counts,” *Astron. Astrophys.*, vol. 594, p. A24, Sep. 2016. <http://adsabs.harvard.edu/abs/2016A%26A...594A..24P>
- [68] J.-B. Melin and J. G. Bartlett, “Measuring cluster masses with CMB lensing: a statistical approach,” *Astron. Astrophys.*, vol. 578, p. A21, Jun. 2015. <http://adsabs.harvard.edu/abs/2015A%26A...578A..21M>
- [69] Y. B. Zeldovich and R. A. Sunyaev, “The Interaction of Matter and Radiation in a Hot-Model Universe,” *ApSS*, vol. 4, pp. 301–316, Jul. 1969. <http://adsabs.harvard.edu/abs/1969Ap%26SS...4..301Z>
- [70] R. A. Sunyaev and Y. B. Zeldovich, “The Observations of Relic Radiation as a Test of the Nature of X-Ray Radiation from the Clusters of Galaxies,” *Comments on Astrophysics and Space Physics*, vol. 4, p. 173, Nov. 1972. <http://adsabs.harvard.edu/abs/1972CoASP..4..173S>
- [71] J. L. Sievers, R. A. Hlozek, M. R. Nolta *et al.*, “The Atacama Cosmology Telescope: cosmological parameters from three seasons of data,” *JCAP*, vol. 10, p. 060, Oct. 2013. <http://adsabs.harvard.edu/abs/2013JCAP..10..060S>
- [72] E. M. George, C. L. Reichardt, K. A. Aird *et al.*, “A Measurement of Secondary Cosmic Microwave Background Anisotropies from the 2500 Square-degree SPT-SZ Survey,” *Ap. J.*, vol. 799, p. 177, Feb. 2015. <http://adsabs.harvard.edu/abs/2015ApJ...799..177G>
- [73] J. Delabrouille, J.-F. Cardoso, M. Le Jeune, M. Betoule, G. Fay, and F. Guilloux, “A full sky, low foreground, high resolution CMB map from WMAP,” *Astron. Astrophys.*, vol. 493, pp. 835–857, Jan. 2009. <http://adsabs.harvard.edu/abs/2009A%26A...493..835D>
- [74] J. Delabrouille, M. Betoule, J. B. Melin *et al.*, “The pre-launch Planck Sky Model: a model of sky emission at submillimetre to centimetre wavelengths,” *Astron. Astrophys.*, vol. 553, p. A96, May 2013. <https://ui.adsabs.harvard.edu/#abs/2013A&A...553A..96D>
- [75] Planck Collaboration, Y. Akrami, F. Arroja *et al.*, “Planck 2018 results. I. Overview and the cosmological legacy of Planck,” *arXiv e-prints*, Jul. 2018. <http://adsabs.harvard.edu/abs/2018arXiv180706205P>
- [76] A. G. Riess, S. Casertano, W. Yuan *et al.*, “Milky Way Cepheid Standards for Measuring Cosmic Distances and Application to Gaia DR2: Implications for the Hubble Constant,” *Ap. J.*, vol. 861, p. 126, Jul. 2018. <http://adsabs.harvard.edu/abs/2018ApJ...861..126R>
- [77] C. J. Copi, D. Huterer, D. J. Schwarz, and G. D. Starkman, “Lack of large-angle TT correlations persists in WMAP and Planck,” *MNRAS*, vol. 451, pp. 2978–2985, Aug. 2015. <http://adsabs.harvard.edu/abs/2015MNRAS.451.2978C>
- [78] S. Joudaki, C. Blake, C. Heymans *et al.*, “CFHTLenS revisited: assessing concordance with Planck including astrophysical systematics,” *MNRAS*, vol. 465, pp. 2033–2052, Feb. 2017. <http://adsabs.harvard.edu/abs/2017MNRAS.465.2033J>
- [79] T. M. C. Abbott, F. B. Abdalla, A. Alarcon *et al.*, “Dark Energy Survey year 1 results: Cosmological

- constraints from galaxy clustering and weak lensing," *Phys. Rev. D.*, vol. 98, no. 4, p. 043526, Aug. 2018. <http://adsabs.harvard.edu/abs/2018PhRvD..98d3526A>
- [80] C. Hikage, M. Oguri, T. Hamana *et al.*, "Cosmology from cosmic shear power spectra with Subaru Hyper Suprime-Cam first-year data," *arXiv e-prints*, Sep. 2018. <http://adsabs.harvard.edu/abs/2018arXiv180909148H>
- [81] E. van Uitert, B. Joachimi, S. Joudaki *et al.*, "KiDS+GAMA: cosmology constraints from a joint analysis of cosmic shear, galaxy-galaxy lensing, and angular clustering," *MNRAS*, vol. 476, pp. 4662–4689, Jun. 2018. <http://adsabs.harvard.edu/abs/2018MNRAS.476.4662V>
- [82] Planck Collaboration, P. A. R. Ade, N. Aghanim *et al.*, "Planck 2015 results. XXIV. Cosmology from Sunyaev-Zeldovich cluster counts," *Astron. Astrophys.*, vol. 594, p. A24, Sep. 2016. <http://adsabs.harvard.edu/abs/2016A%26A...594A..24P>
- [83] S. Bocquet, J. P. Dietrich, T. Schrabback *et al.*, "Cluster Cosmology Constraints from the 2500 deg² SPT-SZ Survey: Inclusion of Weak Gravitational Lensing Data from Magellan and the Hubble Space Telescope," *arXiv e-prints*, Dec. 2018. <http://adsabs.harvard.edu/abs/2018arXiv181201679B>
- [84] E. Di Valentino, T. Brinckmann, M. Gerbino *et al.*, "Exploring cosmic origins with CORE: Cosmological parameters," *JCAP*, vol. 4, p. 017, Apr. 2018. <http://adsabs.harvard.edu/abs/2018JCAP...04..017D>
- [85] Y. Wang, "Figure of merit for dark energy constraints from current observational data," *Phys. Rev. D.*, vol. 77, no. 12, p. 123525, Jun. 2008. <http://adsabs.harvard.edu/abs/2008PhRvD..77l3525W>
- [86] M. Tanabashi, K. Hagiwara, K. Hikasa *et al.*, "Review of Particle Physics*," *Phys. Rev. D.*, vol. 98, no. 3, p. 030001, Aug. 2018. <http://adsabs.harvard.edu/abs/2018PhRvD..98c0001T>
- [87] T. Namikawa, S. Saito, and A. Taruya, "Probing dark energy and neutrino mass from upcoming lensing experiments of CMB and galaxies," *JCAP*, vol. 12, p. 027, Dec. 2010. <http://adsabs.harvard.edu/abs/2010JCAP...12..027N>
- [88] PICO website, "Testing Λ CDM." <https://sites.google.com/umn.edu/picomission/home/testlcdm>
- [89] Planck Collaboration, N. Aghanim, Y. Akrami *et al.*, "Planck 2018 results. XII. Galactic astrophysics using polarized dust emission," *ArXiv e-prints*, Jul. 2018. <https://ui.adsabs.harvard.edu/#abs/2018arXiv180706212P>
- [90] D. T. Chuss, B.-G. Andersson, J. Bally *et al.*, "HAWC+/SOFIA Multiwavelength Polarimetric Observations of OMC-1," *ArXiv e-prints*, Oct. 2018. <https://ui.adsabs.harvard.edu/#abs/2018arXiv181008233C>
- [91] F. Bacciotti, J. M. Girart, M. Padovani *et al.*, "ALMA Observations of Polarized Emission toward the CW Tau and DG Tau Protoplanetary Disks: Constraints on Dust Grain Growth and Settling," *Ap. J.*, vol. 865, p. L12, Oct. 2018. <https://ui.adsabs.harvard.edu/#abs/2018ApJ...865L..12B>
- [92] C. H. Smith, C. M. Wright, D. K. Aitken, P. F. Roche, and J. H. Hough, "Studies in mid-infrared spectropolarimetry - II. An atlas of spectra," *MNRAS*, vol. 312, pp. 327–361, Feb. 2000. <http://adsabs.harvard.edu/abs/2000MNRAS.312..327S>
- [93] J. E. Chiar, A. J. Adamson, D. C. B. Whittet *et al.*, "Spectropolarimetry of the 3.4 μ m Feature in the Diffuse ISM toward the Galactic Center Quintuplet Cluster," *Ap. J.*, vol. 651, pp. 268–271, Nov. 2006. <http://adsabs.harvard.edu/abs/2006ApJ...651..268C>
- [94] R. E. Mason, G. S. Wright, A. Adamson, and Y. Pendleton, "Spectropolarimetry of the 3.4 μ m Absorption Feature in NGC 1068," *Ap. J.*, vol. 656, pp. 798–804, Feb. 2007. <http://adsabs.harvard.edu/abs/2007ApJ...656..798M>
- [95] Planck Collaboration, P. A. R. Ade, M. I. R. Alves *et al.*, "Planck intermediate results. XXII. Frequency dependence of thermal emission from Galactic dust in intensity and polarization," *Astron. Astrophys.*, vol. 576, p. A107, Apr. 2015. <http://adsabs.harvard.edu/abs/2015A%26A...576A.107P>
- [96] P. C. Ashton, P. A. R. Ade, F. E. Angilè *et al.*, "First Observation of the Submillimeter Polarization Spectrum in a Translucent Molecular Cloud," *Ap. J.*, vol. 857, p. 10, Apr. 2018. <http://adsabs.harvard.edu/abs/2018ApJ...857...10A>
- [97] A. M. Meisner and D. P. Finkbeiner, "Modeling Thermal Dust Emission with Two Components: Application to the Planck High Frequency Instrument Maps," *Ap. J.*, vol. 798, p. 88, Jan. 2015. <https://ui.adsabs.harvard.edu/#abs/2015ApJ...798...88M>
- [98] B. T. Draine and A. A. Fraisse, "Polarized Far-Infrared and Submillimeter Emission from Interstellar Dust," *Ap. J.*, vol. 696, pp. 1–11, May 2009. <http://adsabs.harvard.edu/abs/2009ApJ...696....1D>
- [99] V. Guillet, L. Fanciullo, L. Verstraete *et al.*, "Dust models compatible with Planck intensity and polarization data in translucent lines of sight," *Astron. Astrophys.*, vol. 610, p. A16, Feb. 2018.

<http://adsabs.harvard.edu/abs/2018A%26A...610A..16G>

- [100] B. T. Draine and B. Hensley, “Magnetic Nanoparticles in the Interstellar Medium: Emission Spectrum and Polarization,” *Ap. J.*, vol. 765, p. 159, Mar. 2013. <http://adsabs.harvard.edu/abs/2013ApJ...765..159D>
- [101] C. Dickinson, Y. Ali-Haïmoud, A. Barr *et al.*, “The State-of-Play of Anomalous Microwave Emission (AME) research,” *New Ast. Rev.*, vol. 80, pp. 1–28, Feb. 2018. <http://adsabs.harvard.edu/abs/2018NewAR..80....1D>
- [102] C. Dickinson, A. Barr, H. C. Chiang *et al.*, “The C-Band All-Sky Survey (C-BASS): Constraining diffuse Galactic radio emission in the North Celestial Pole region,” *ArXiv e-prints*, Oct. 2018. <https://ui.adsabs.harvard.edu/#abs/2018arXiv181011681D>
- [103] S. E. Clark, J. E. G. Peek, and M. E. Putman, “Magnetically Aligned H I Fibers and the Rolling Hough Transform,” *Ap. J.*, vol. 789, p. 82, Jul. 2014. <http://adsabs.harvard.edu/abs/2014ApJ...789..82C>
- [104] S. E. Clark, J. C. Hill, J. E. G. Peek, M. E. Putman, and B. L. Babler, “Neutral Hydrogen Structures Trace Dust Polarization Angle: Implications for Cosmic Microwave Background Foregrounds,” *Physical Review Letters*, vol. 115, no. 24, p. 241302, Dec. 2015. <http://adsabs.harvard.edu/abs/2015PhRvL.115x1302C>
- [105] P. M. W. Kalberla, J. Kerp, U. Haud, B. Winkel, N. Ben Bekhti, L. Flöer, and D. Lenz, “Cold Milky Way HI Gas in Filaments,” *Ap. J.*, vol. 821, p. 117, Apr. 2016. <http://adsabs.harvard.edu/abs/2016ApJ...821..117K>
- [106] P. M. W. Kalberla and J. Kerp, “Anisotropies in the HI gas distribution toward 3C 196,” *Astron. Astrophys.*, vol. 595, p. A37, Oct. 2016. <http://esoads.eso.org/abs/2016A%26A...595A..37K>
- [107] R. M. Crutcher, B. Wandelt, C. Heiles, E. Falgarone, and T. H. Troland, “Magnetic Fields in Interstellar Clouds from Zeeman Observations: Inference of Total Field Strengths by Bayesian Analysis,” *Ap. J.*, vol. 725, pp. 466–479, Dec. 2010. <http://adsabs.harvard.edu/abs/2010ApJ...725..466C>
- [108] HI4PI Collaboration, “HI4PI: A full-sky H I survey based on EBHIS and GASS,” *Astron. Astrophys.*, vol. 594, p. A116, Oct. 2016. <http://adsabs.harvard.edu/abs/2016A%26A...594A.116H>
- [109] J. E. G. Peek, B. L. Babler, Y. Zheng *et al.*, “The GALFA-H I Survey Data Release 2,” *Ap. J. Suppl.*, vol. 234, p. 2, Jan. 2018. <http://adsabs.harvard.edu/abs/2018ApJS..234....2P>
- [110] N. M. McClure-Griffiths, S. Stanimirovic, C. Murray *et al.*, “Galactic and Magellanic Evolution with the SKA,” in *Advancing Astrophysics with the Square Kilometre Array (AASKA14)*, Apr. 2015, p. 130. <https://ui.adsabs.harvard.edu/#abs/2015aska.confE.130M>
- [111] T. P. Ellsworth-Bowers, E. Rosolowsky, J. Glenn, A. Ginsburg, N. J. Evans, II, C. Battersby, Y. L. Shirley, and B. Svoboda, “The Bolocam Galactic Plane Survey. XII. Distance Catalog Expansion Using Kinematic Isolation of Dense Molecular Cloud Structures with $^{13}\text{CO}(1\text{-}0)$,” *Ap. J.*, vol. 799, p. 29, Jan. 2015. <http://adsabs.harvard.edu/abs/2015ApJ...799..29E>
- [112] Planck Collaboration, P. A. R. Ade, N. Aghanim *et al.*, “Planck intermediate results. XXXV. Probing the role of the magnetic field in the formation of structure in molecular clouds,” *Astron. Astrophys.*, vol. 586, p. A138, Feb. 2016. <http://adsabs.harvard.edu/abs/2016A%26A...586A.138P>
- [113] A. Allen, Z.-Y. Li, and F. H. Shu, “Collapse of Magnetized Singular Isothermal Toroids. II. Rotation and Magnetic Braking,” *Ap. J.*, vol. 599, pp. 363–379, Dec. 2003. <http://adsabs.harvard.edu/abs/2003ApJ...599..363A>
- [114] Z.-Y. Li, R. Krasnopolsky, H. Shang, and B. Zhao, “On the Role of Pseudodisk Warping and Reconnection in Protostellar Disk Formation in Turbulent Magnetized Cores,” *Ap. J.*, vol. 793, p. 130, Oct. 2014. <http://adsabs.harvard.edu/abs/2014ApJ...793..130L>
- [115] D. A. Harper, M. C. Runyan, C. D. Dowell *et al.*, “Hawc+, the far-infrared camera and polarimeter for sofia,” *Journal of Astronomical Instrumentation*, vol. 07, no. 04, p. 1840008, 2018. <https://doi.org/10.1142/S2251171718400081>
- [116] A. Lazarian, “Enhancement and Suppression of Heat Transfer by MHD Turbulence,” *Ap. J. Lett.*, vol. 645, pp. L25–L28, Jul. 2006. <http://adsabs.harvard.edu/abs/2006ApJ...645L..25L>
- [117] A. Lazarian, “Damping of Alfvén Waves by Turbulence and Its Consequences: From Cosmic-ray Streaming to Launching Winds,” *Ap. J.*, vol. 833, p. 131, Dec. 2016. <http://adsabs.harvard.edu/abs/2016ApJ...833..131L>
- [118] A. Lazarian and E. T. Vishniac, “Reconnection in a Weakly Stochastic Field,” *Ap. J.*, vol. 517, pp. 700–718, Jun. 1999. <http://adsabs.harvard.edu/abs/1999ApJ...517..700L>
- [119] S. Xu and A. Lazarian, “Magnetohydrodynamic turbulence and turbulent dynamo in partially ionized plasma,” *New Journal of Physics*, vol. 19, no. 6, p. 065005, 2017. <http://stacks.iop.org/1367-2630/19/i=6/a=065005>
- [120] T. J. Jones, C. D. Dowell, E. Lopez Rodriguez *et al.*, “SOFIA Far Infrared Imaging Polarimetry of M82

- and NGC 253: Exploring the Super-Galactic Wind,” *arXiv e-prints*, p. arXiv:1812.06816, Dec. 2018. <https://ui.adsabs.harvard.edu/#abs/2018arXiv181206816J>
- [121] J. Silk and G. A. Mamon, “The current status of galaxy formation,” *Research in Astronomy and Astrophysics*, vol. 12, pp. 917–946, Aug. 2012. <http://adsabs.harvard.edu/abs/2012RAA....12..917S>
- [122] R. S. Somerville and R. Davé, “Physical Models of Galaxy Formation in a Cosmological Framework,” *ARA&A*, vol. 53, pp. 51–113, Aug. 2015. <http://adsabs.harvard.edu/abs/2015ARA%26A..53...51S>
- [123] S. Fujimoto, M. Ouchi, K. Kohno *et al.*, “ALMA 26 Arcmin² Survey of GOODS-S at One Millimeter (ASAGAO): Average Morphology of High-z Dusty Star-forming Galaxies in an Exponential Disk ($n \simeq 1$)”, *Ap. J.*, vol. 861, p. 7, Jul. 2018. <http://adsabs.harvard.edu/abs/2018ApJ...861....7F>
- [124] R. Cañameras, N. Nesvadba, R. Kneissl *et al.*, “Planck’s dusty GEMS. IV. Star formation and feedback in a maximum starburst at $z = 3$ seen at 60-pc resolution,” *Astron. Astrophys.*, vol. 604, p. A117, Aug. 2017. <http://adsabs.harvard.edu/abs/2017A%26A...604A.117C>
- [125] A. King and K. Pounds, “Powerful Outflows and Feedback from Active Galactic Nuclei,” *ARA&A*, vol. 53, pp. 115–154, Aug. 2015. <http://adsabs.harvard.edu/abs/2015ARA%26A..53..115K>
- [126] J. S. Spilker, M. Aravena, M. Béthermin *et al.*, “Fast molecular outflow from a dusty star-forming galaxy in the early Universe,” *Science*, vol. 361, pp. 1016–1019, Sep. 2018. <http://adsabs.harvard.edu/abs/2018Sci...361.1016S>
- [127] S. Dye, C. Furlanetto, L. Dunne *et al.*, “Modelling high-resolution ALMA observations of strongly lensed highly star-forming galaxies detected by Herschel,” *MNRAS*, vol. 476, pp. 4383–4394, Jun. 2018. <http://adsabs.harvard.edu/abs/2018MNRAS.476.4383D>
- [128] C. Lamarche, A. Verma, A. Vishwas *et al.*, “Resolving Star Formation on Subkiloparsec Scales in the High-redshift Galaxy SDP.11 Using Gravitational Lensing,” *Ap. J.*, vol. 867, p. 140, Nov. 2018. <http://adsabs.harvard.edu/abs/2018ApJ...867..140L>
- [129] P. Sharda, C. Federrath, E. da Cunha, A. M. Swinbank, and S. Dye, “Testing star formation laws in a starburst galaxy at redshift 3 resolved with ALMA,” *MNRAS*, vol. 477, pp. 4380–4390, Jul. 2018. <http://adsabs.harvard.edu/abs/2018MNRAS.477.4380S>
- [130] M. Negrello, S. Amber, A. Amvrosiadis *et al.*, “The Herschel-ATLAS: a sample of 500 μm -selected lensed galaxies over 600 deg²,” *MNRAS*, vol. 465, pp. 3558–3580, Mar. 2017. <http://adsabs.harvard.edu/abs/2017MNRAS.465.3558N>
- [131] T. Treu, “Strong Lensing by Galaxies,” *Ann. Rev. Astr. Ap.*, vol. 48, pp. 87–125, Sep. 2010. <http://adsabs.harvard.edu/abs/2010ARA%26A..48...87T>
- [132] M. Negrello, R. Hopwood, G. De Zotti *et al.*, “The Detection of a Population of Submillimeter-Bright, Strongly Lensed Galaxies,” *Science*, vol. 330, p. 800, Nov. 2010. <http://adsabs.harvard.edu/abs/2010Sci...330..800N>
- [133] A. M. Swinbank, I. Smail, S. Longmore *et al.*, “Intense star formation within resolved compact regions in a galaxy at $z = 2.3$,” *Nature*, vol. 464, pp. 733–736, Apr. 2010. <http://adsabs.harvard.edu/abs/2010Natur.464..733S>
- [134] F. Combes, M. Rex, T. D. Rawle *et al.*, “A bright $z = 5.2$ lensed submillimeter galaxy in the field of Abell 773. HLSJ091828.6+514223,” *Astron. Astrophys.*, vol. 538, p. L4, Feb. 2012. <http://adsabs.harvard.edu/abs/2012A%26A...538L...4C>
- [135] Planck Collaboration, P. A. R. Ade, N. Aghanim *et al.*, “Planck 2015 results. XXVI. The Second Planck Catalogue of Compact Sources,” *Astron. Astrophys.*, vol. 594, p. A26, Sep. 2016. <http://adsabs.harvard.edu/abs/2016A%26A...594A..26P>
- [136] M. Negrello, J. Gonzalez-Nuevo, G. De Zotti *et al.*, “On the statistics of proto-cluster candidates detected in the Planck all-sky survey,” *MNRAS*, vol. 470, pp. 2253–2261, Sep. 2017. <http://adsabs.harvard.edu/abs/2017MNRAS.470.2253N>
- [137] R. A. Overzier, “The realm of the galaxy protoclusters. A review,” *Astron. Astrophys. Rev.*, vol. 24, p. 14, Nov. 2016. <http://adsabs.harvard.edu/abs/2016A%26ARv..24...14O>
- [138] Planck Collaboration, P. A. R. Ade, N. Aghanim *et al.*, “Planck intermediate results. XXXIX. The Planck list of high-redshift source candidates,” *Astron. Astrophys.*, vol. 596, p. A100, Dec. 2016. <http://adsabs.harvard.edu/abs/2016A%26A...596A.100P>
- [139] C.-Y. Chen, P. K. King, and Z.-Y. Li, “Change of Magnetic Field-gas Alignment at the Gravity-driven Alfvénic Transition in Molecular Clouds: Implications for Dust Polarization Observations,” *Ap. J.*, vol. 829, p. 84, Oct.

2016. <http://adsabs.harvard.edu/abs/2016ApJ...829...84C>
- [140] R. J. Ivison, A. M. Swinbank, I. Smail *et al.*, “Herschel-ATLAS: A Binary HyLIRG Pinpointing a Cluster of Starbursting Protoellipticals,” *Ap. J.*, vol. 772, p. 137, Aug. 2013. <http://adsabs.harvard.edu/abs/2013ApJ...772..137I>
- [141] T. Wang, D. Elbaz, E. Daddi *et al.*, “Discovery of a Galaxy Cluster with a Violently Starbursting Core at $z = 2.506$,” *Ap. J.*, vol. 828, p. 56, Sep. 2016. <http://adsabs.harvard.edu/abs/2016ApJ...828...56W>
- [142] I. Oteo, R. J. Ivison, L. Dunne *et al.*, “An Extreme Protocluster of Luminous Dusty Starbursts in the Early Universe,” *Ap. J.*, vol. 856, p. 72, Mar. 2018. <http://adsabs.harvard.edu/abs/2018ApJ...856...72O>
- [143] B. D. Metzger, P. K. G. Williams, and E. Berger, “Extragalactic Synchrotron Transients in the Era of Wide-field Radio Surveys. I. Detection Rates and Light Curve Characteristics,” *Ap. J.*, vol. 806, p. 224, Jun. 2015. <http://adsabs.harvard.edu/abs/2015ApJ...806..224M>
- [144] Planck Collaboration, P. A. R. Ade, N. Aghanim *et al.*, “Planck 2013 results. XXX. Cosmic infrared background measurements and implications for star formation,” *Astron. Astrophys.*, vol. 571, p. A30, Nov. 2014. <http://adsabs.harvard.edu/abs/2014A%26A...571A..30P>
- [145] P. Collaboration, P. A. R. Ade, N. Aghanim *et al.*, “Planck 2013 results. XVIII. The gravitational lensing-infrared background correlation,” *Astron. Astrophys.*, vol. 571, p. A18, Nov. 2014. <http://adsabs.harvard.edu/abs/2014A%26A...571A..18P>
- [146] P. Madau and M. Dickinson, “Cosmic Star-Formation History,” *ARA&A*, vol. 52, pp. 415–486, Aug. 2014. <http://adsabs.harvard.edu/abs/2014ARA%26A..52..415M>
- [147] H.-Y. Wu and O. Doré, “Optimizing future experiments of cosmic far-infrared background: a principal component approach,” *MNRAS*, vol. 467, pp. 4150–4160, Jun. 2017. <http://adsabs.harvard.edu/abs/2017MNRAS.467.4150W>
- [148] B. D. Sherwin and M. Schmittfull, “Delensing the CMB with the cosmic infrared background,” *Phys. Rev. D.*, vol. 92, no. 4, p. 043005, Aug. 2015. <http://adsabs.harvard.edu/abs/2015PhRvD..92d3005S>
- [149] M. Tucci, V. Desjacques, and M. Kunz, “Cosmic infrared background anisotropies as a window into primordial non-Gaussianity,” *MNRAS*, vol. 463, pp. 2046–2063, Dec. 2016. <http://adsabs.harvard.edu/abs/2016MNRAS.463.2046T>
- [150] Planck Collaboration, R. Adam, P. A. R. Ade *et al.*, “Planck intermediate results. XXX. The angular power spectrum of polarized dust emission at intermediate and high Galactic latitudes,” *Astron. Astrophys.*, vol. 586, p. A133, Feb. 2016. <http://adsabs.harvard.edu/abs/2016A%26A...586A.133P>
- [151] N. Krachmalnicoff, E. Carretti, C. Baccigalupi *et al.*, “S-PASS view of polarized Galactic synchrotron at 2.3 GHz as a contaminant to CMB observations,” *Astron. Astrophys.*, vol. 618, p. A166, Oct. 2018. <http://adsabs.harvard.edu/abs/2018A%26A...618A.166K>
- [152] U. Fuskeland, I. K. Wehus, H. K. Eriksen, and S. K. Næss, “Spatial Variations in the Spectral Index of Polarized Synchrotron Emission in the 9 yr WMAP Sky Maps,” *Ap. J.*, vol. 790, p. 104, Aug. 2014. <https://ui.adsabs.harvard.edu/#abs/2014ApJ...790..104F>
- [153] Planck Collaboration, A. Abergel, P. A. R. Ade *et al.*, “Planck 2013 results. XI. All-sky model of thermal dust emission,” *Astron. Astrophys.*, vol. 571, p. A11, Nov. 2014. <https://ui.adsabs.harvard.edu/#abs/2014A&A..571A..11P>
- [154] J. Chluba, J. C. Hill, and M. H. Abitbol, “Rethinking CMB foregrounds: systematic extension of foreground parametrizations,” *MNRAS*, vol. 472, pp. 1195–1213, Nov. 2017. <http://adsabs.harvard.edu/abs/2017MNRAS.472.1195C>
- [155] Y. Fantaye, F. Stivoli, J. Grain, S. M. Leach, M. Tristram, C. Baccigalupi, and R. Stompor, “Estimating the tensor-to-scalar ratio and the effect of residual foreground contamination,” *JCAP*, vol. 8, p. 1, Aug. 2011. <http://adsabs.harvard.edu/abs/2011JCAP..08..001F>
- [156] C. Armitage-Caplan, J. Dunkley, H. K. Eriksen, and C. Dickinson, “Impact on the tensor-to-scalar ratio of incorrect Galactic foreground modelling,” *MNRAS*, vol. 424, pp. 1914–1924, Aug. 2012. <http://adsabs.harvard.edu/abs/2012MNRAS.424.1914A>
- [157] A. Kogut and D. J. Fixsen, “Foreground Bias from Parametric Models of Far-IR Dust Emission,” *Ap. J.*, vol. 826, p. 101, Aug. 2016. <http://adsabs.harvard.edu/abs/2016ApJ...826..101K>
- [158] M. Remazeilles, C. Dickinson, H. K. K. Eriksen, and I. K. Wehus, “Sensitivity and foreground modelling for large-scale cosmic microwave background B-mode polarization satellite missions,” *MNRAS*, vol. 458, pp.

2032–2050, May 2016. <http://adsabs.harvard.edu/abs/2016MNRAS.458.2032R>

- [159] R. Stompor, J. Errard, and D. Poletti, “Forecasting performance of CMB experiments in the presence of complex foreground contaminations,” *Phys. Rev. D.*, vol. 94, no. 8, p. 083526, Oct. 2016. <http://adsabs.harvard.edu/abs/2016PhRvD..94h3526S>
- [160] C. Dickinson, Y. Ali-Haïmoud, A. Barr *et al.*, “The State-of-Play of Anomalous Microwave Emission (AME) research,” *New Astronomy Reviews*, vol. 80, pp. 1–28, Feb. 2018. <http://adsabs.harvard.edu/abs/2018NewAR..80....1D>
- [161] M. Remazeilles, C. Dickinson, H. K. K. Eriksen, and I. K. Wehus, “Sensitivity and foreground modelling for large-scale cosmic microwave background B-mode polarization satellite missions,” *MNRAS*, vol. 458, pp. 2032–2050, May 2016. <http://adsabs.harvard.edu/abs/2016MNRAS.458.2032R>
- [162] J. S. Greaves, W. S. Holland, P. Friberg, and W. R. F. Dent, “Polarized CO Emission from Molecular Clouds,” *Ap. J. Lett.*, vol. 512, pp. L139–L142, Feb. 1999. <http://adsabs.harvard.edu/abs/1999ApJ...512L.139G>
- [163] G. Puglisi, G. Fabbian, and C. Baccigalupi, “A 3D model for carbon monoxide molecular line emission as a potential cosmic microwave background polarization contaminant,” *MNRAS*, vol. 469, pp. 2982–2996, Aug. 2017. <http://adsabs.harvard.edu/abs/2017MNRAS.469.2982P>
- [164] L. Bonavera, J. González-Nuevo, F. Argüeso, and L. Toffolatti, “Statistics of the fractional polarization of compact radio sources in Planck maps,” *MNRAS*, vol. 469, pp. 2401–2411, Aug. 2017. <http://adsabs.harvard.edu/abs/2017MNRAS.469.2401B>
- [165] G. Puglisi, V. Galluzzi, L. Bonavera *et al.*, “Forecasting the Contribution of Polarized Extragalactic Radio Sources in CMB Observations,” *Ap. J.*, vol. 858, p. 85, May 2018. <http://adsabs.harvard.edu/abs/2018ApJ...858...85P>
- [166] T. Trombetti, C. Burigana, G. De Zotti, V. Galluzzi, and M. Massardi, “Average fractional polarization of extragalactic sources at Planck frequencies,” *Astron. Astrophys.*, vol. 618, p. A29, Oct. 2018. <http://adsabs.harvard.edu/abs/2018A%26A...618A..29T>
- [167] L. Toffolatti, C. Burigana, F. Argüeso, and J. Mariño Diego, “Extragalactic compact sources in the planck sky and their cosmological implications,” in *Open Questions in Cosmology, first edition*. InTech Open, 11 2012, pp. 57–86. <http://adsabs.harvard.edu/abs/2013arXiv1302.3355T>
- [168] M. Remazeilles, A. J. Banday, C. Baccigalupi *et al.*, “Exploring cosmic origins with CORE: B-mode component separation,” *JCAP*, vol. 4, p. 023, Apr. 2018. <http://adsabs.harvard.edu/abs/2018JCAP..04..023R>
- [169] J. Errard, S. M. Feeney, H. V. Peiris, and A. H. Jaffe, “Robust forecasts on fundamental physics from the foreground-obscured, gravitationally-lensed CMB polarization,” *JCAP*, vol. 3, p. 052, Mar. 2016. <http://adsabs.harvard.edu/abs/2016JCAP..03..052E>
- [170] H. K. Eriksen, J. B. Jewell, C. Dickinson, A. J. Banday, K. M. Górski, and C. R. Lawrence, “Joint Bayesian Component Separation and CMB Power Spectrum Estimation,” *Ap. J.*, vol. 676, pp. 10–32, Mar. 2008. <http://adsabs.harvard.edu/abs/2008ApJ...676...10E>
- [171] J. Delabrouille, J.-F. Cardoso, and G. Patanchon, “Multidetector multicomponent spectral matching and applications for cosmic microwave background data analysis,” *MNRAS*, vol. 346, pp. 1089–1102, Dec. 2003. <http://adsabs.harvard.edu/abs/2003MNRAS.346.1089D>
- [172] J.-F. Cardoso, M. Le Jeune, J. Delabrouille, M. Betoule, and G. Patanchon, “Component Separation With Flexible Models - Application to Multichannel Astrophysical Observations,” *IEEE Journal of Selected Topics in Signal Processing*, vol. 2, pp. 735–746, Nov. 2008. <http://adsabs.harvard.edu/abs/2008JSTSP...2..735C>
- [173] S. Basak and J. Delabrouille, “A needlet ILC analysis of WMAP 9-year polarization data: CMB polarization power spectra,” *MNRAS*, vol. 435, pp. 18–29, Oct. 2013. <http://adsabs.harvard.edu/abs/2013MNRAS.435...18B>
- [174] M. Remazeilles, J. Delabrouille, and J.-F. Cardoso, “Foreground component separation with generalized Internal Linear Combination,” *MNRAS*, vol. 418, pp. 467–476, Nov. 2011. <http://adsabs.harvard.edu/abs/2011MNRAS.418.467R>
- [175] PICO website, “Foreground Separation with GNILC.” <https://sites.google.com/umn.edu/picomission/home/gnilc>
- [176] K. M. Górski, E. Hivon, A. J. Banday, B. D. Wandelt, F. K. Hansen, M. Reinecke, and M. Bartelmann, “HEALPix: A Framework for High-Resolution Discretization and Fast Analysis of Data Distributed on the Sphere,” *Ap. J.*, vol. 622, pp. 759–771, Apr. 2005. <http://adsabs.harvard.edu/abs/2005ApJ...622..759G>
- [177] B. Thorne, J. Dunkley, D. Alonso, and S. Næss, “The Python Sky Model: software for simulating the Galactic

- microwave sky,” *MNRAS*, vol. 469, pp. 2821–2833, Aug. 2017. <http://adsabs.harvard.edu/abs/2017MNRAS.469.2821T>
- [178] W. Hu, M. M. Hedman, and M. Zaldarriaga, “Benchmark parameters for CMB polarization experiments,” *Phys. Rev. D.*, vol. 67, pp. 043 004–+, Feb. 2003, astro-ph/0210096. http://adsabs.harvard.edu/cgi-bin/nph-bib_query?bibcode=2003PhRvD..67d3004H&db_key=AST
- [179] M. Shimon, B. Keating, N. Ponthieu, and E. Hivon, “CMB polarization systematics due to beam asymmetry: Impact on inflationary science,” *Phys. Rev. D.*, vol. 77, no. 8, pp. 083 003–+, Apr. 2008. <http://adsabs.harvard.edu/abs/2008PhRvD..77h3003S>
- [180] A. P. S. Yadav, M. Su, and M. Zaldarriaga, “Primordial B-mode diagnostics and self-calibrating the CMB polarization,” *Phys. Rev. D.*, vol. 81, no. 6, pp. 063 512–+, Mar. 2010. <http://adsabs.harvard.edu/abs/2010PhRvD..81f3512Y>
- [181] L. M. Griffiths and C. H. Lineweaver, “Testing the Cosmic Microwave Background Data for Systematic Effects,” *Ap. J.*, vol. 603, pp. 371–382, Mar. 2004. <http://adsabs.harvard.edu/abs/2004ApJ...603..371G>
- [182] Planck Collaboration, P. A. R. Ade, J. Aumont *et al.*, “Planck 2015 results. III. LFI systematic uncertainties,” *Astron. Astrophys.*, vol. 594, p. A3, Sep. 2016. <http://adsabs.harvard.edu/abs/2016A%26A...594A..3P>
- [183] J. Kaplan and J. Delabrouille, “Some sources of systematic errors on CMB polarized measurements with bolometers,” in *Astrophysical Polarized Backgrounds*, ser. American Institute of Physics Conference Series, S. Cecchini, S. Cortiglioni, R. Sault, and C. Sbarra, Eds., vol. 609, Mar. 2002, pp. 209–214. <http://adsabs.harvard.edu/abs/2002AIPC..609..209K>
- [184] N. J. Miller, M. Shimon, and B. G. Keating, “CMB polarization systematics due to beam asymmetry: Impact on cosmological birefringence,” *Phys. Rev. D.*, vol. 79, no. 10, p. 103002, May 2009. <http://adsabs.harvard.edu/abs/2009PhRvD..79j3002M>
- [185] L. Pagano, P. de Bernardis, G. de Troia *et al.*, “CMB polarization systematics, cosmological birefringence, and the gravitational waves background,” *Phys. Rev. D.*, vol. 80, no. 4, p. 043522, Aug. 2009. <http://adsabs.harvard.edu/abs/2009PhRvD..80d3522P>
- [186] P. A. Gallardo, J. Gudmundsson, B. J. Koopman *et al.*, “Systematic uncertainties in the Simons Observatory: optical effects and sensitivity considerations,” in *Millimeter, Submillimeter, and Far-Infrared Detectors and Instrumentation for Astronomy IX*, ser. Society of Photo-Optical Instrumentation Engineers (SPIE) Conference Series, vol. 10708, Jul. 2018, p. 107083Y. <http://adsabs.harvard.edu/abs/2018SPIE10708E..3YG>
- [187] K. T. Crowley, S. M. Simon, M. Silva-Feaver *et al.*, “Studies of systematic uncertainties for Simons Observatory: detector array effects,” in *Millimeter, Submillimeter, and Far-Infrared Detectors and Instrumentation for Astronomy IX*, ser. Society of Photo-Optical Instrumentation Engineers (SPIE) Conference Series, vol. 10708, Jul. 2018, p. 107083Z. <http://adsabs.harvard.edu/abs/2018SPIE10708E..3ZC>
- [188] BICEP2 Collaboration, P. A. R. Ade, R. W. Aikin *et al.*, “BICEP2 III: Instrumental Systematics,” *Ap. J.*, vol. 814, p. 110, Dec. 2015. <http://adsabs.harvard.edu/abs/2015ApJ...814..110B>
- [189] C. J. MacTavish, P. A. R. Ade, E. S. Battistelli *et al.*, “Spider Optimization: Probing the Systematics of a Large-Scale B-Mode Experiment,” *Ap. J.*, vol. 689, pp. 655–665, Dec. 2008. <http://adsabs.harvard.edu/abs/2008ApJ...689..655M>
- [190] Planck Collaboration, P. A. R. Ade, N. Aghanim *et al.*, “Planck 2015 results. XII. Full focal plane simulations,” *Astron. Astrophys.*, vol. 594, p. A12, Sep. 2016. <http://adsabs.harvard.edu/abs/2016A%26A...594A..12P>
- [191] P. Natoli, M. Ashdown, R. Banerji *et al.*, “Exploring cosmic origins with CORE: Mitigation of systematic effects,” *Journal of Cosmology and Astro-Particle Physics*, vol. 2018, p. 022, Apr. 2018. <https://ui.adsabs.harvard.edu/#abs/2018JCAP..04..022N>
- [192] J. Aumont, J. F. Macías-Pérez, A. Ritacco, N. Ponthieu, and A. Mangilli, “Absolute calibration of the polarisation angle for future CMB B-mode experiments from current and future measurements of the Crab nebula,” *ArXiv e-prints*, May 2018. <http://adsabs.harvard.edu/abs/2018arXiv180510475A>
- [193] PICO website, “Simulating dipole calibration for PICO.” https://sites.google.com/umn.edu/picomission/home/simulating_dipole_pico
- [194] Planck Collaboration, P. A. R. Ade, N. Aghanim *et al.*, “Planck 2013 results. XV. CMB power spectra and likelihood,” *Astron. Astrophys.*, vol. 571, p. A15, Nov. 2014. <http://adsabs.harvard.edu/abs/2014A%26A...571A..15P>
- [195] G. Forma, D. Dubruel, J. Marti-Canales *et al.*, “Radiation-Pattern Measurements and Predictions of the

- PLANCK RF Qualification Model,” in *IEEE Antennas and Propagation Magazine*, vol. 51, no. 6, Dec. 2009, pp. 213–219. <https://ieeexplore.ieee.org/abstract/document/5433156>
- [196] J. H. Kang, P. A. R. Ade, Z. Ahmed *et al.*, “2017 upgrade and performance of BICEP3: a 95GHz refracting telescope for degree-scale CMB polarization,” in *Millimeter, Submillimeter, and Far-Infrared Detectors and Instrumentation for Astronomy IX*, ser. Society of Photo-Optical Instrumentation Engineers (SPIE) Conference Series, vol. 10708, Jul. 2018, p. 107082N. <http://adsabs.harvard.edu/abs/2018SPIE10708E..2NK>
- [197] Private communication.
- [198] K. Young, M. Alvarez, N. Battaglia *et al.*, “Optical design of PICO: a concept for a space mission to probe inflation and cosmic origins,” in *Society of Photo-Optical Instrumentation Engineers (SPIE) Conference Series*, vol. 10698, Aug. 2018, p. 1069846. <https://ui.adsabs.harvard.edu/#abs/2018SPIE10698E..46Y>
- [199] P. de Bernardis, P. A. R. Ade, J. J. A. Baselmans *et al.*, “Exploring cosmic origins with CORE: The instrument,” *Journal of Cosmology and Astro-Particle Physics*, vol. 2018, p. 015, Apr. 2018. <https://ui.adsabs.harvard.edu/#abs/2018JCAP..04..015D>
- [200] C. Dragone, “Offset Multireflector Antennas with Perfect Pattern Symmetry and Polarization Discrimination,” *Bell Syst. Tech. J.*, vol. 57, pp. 2663–2684, 178. <http://adsabs.harvard.edu/abs/1978ATTTJ..57.2663D>
- [201] C. Granet, “Designing classical Dragonian offset dual-reflector antennas from combinations of prescribed geometric parameters,” *IEEE Antennas and Propagation Magazine*, vol. 43, pp. 100–107, Dec. 2001. <https://ui.adsabs.harvard.edu/#abs/2001IAPM..43..100G>
- [202] S. M. Duff, J. Austermann, J. A. Beall *et al.*, “Advanced ACTPol Multichroic Polarimeter Array Fabrication Process for 150 mm Wafers,” *Journal of Low Temperature Physics*, vol. 184, pp. 634–641, Aug. 2016. <https://ui.adsabs.harvard.edu/#abs/2016JLTP..184..634D>
- [203] BICEP2 Collaboration, Keck Array Collaboration, SPIDER Collaboration *et al.*, “Antenna-coupled TES Bolometers Used in BICEP2, Keck Array, and Spider,” *Ap. J.*, vol. 812, p. 176, Oct. 2015. <https://ui.adsabs.harvard.edu/#abs/2015ApJ...812..176B>
- [204] J. M. Edwards, R. O’Brient, A. T. Lee, and G. M. Rebeiz, “Dual-Polarized Sinuous Antennas on Extended Hemispherical Silicon Lenses,” *IEEE Transactions on Antennas and Propagation*, vol. 60, pp. 4082–4091, Sep. 2012. <https://ui.adsabs.harvard.edu/#abs/2012ITAP..60.4082E>
- [205] A. Suzuki, K. Arnold, J. Edwards *et al.*, “Multi-Chroic Dual-Polarization Bolometric Detectors for Studies of the Cosmic Microwave Background,” *Journal of Low Temperature Physics*, vol. 176, pp. 650–656, Sep. 2014. <https://ui.adsabs.harvard.edu/#abs/2014JLTP..176..650S>
- [206] R. O’Brient, P. Ade, K. Arnold *et al.*, “A dual-polarized broadband planar antenna and channelizing filter bank for millimeter wavelengths,” *Applied Physics Letters*, vol. 102, p. 063506, Feb. 2013. <https://ui.adsabs.harvard.edu/#abs/2013ApPhL.102f3506O>
- [207] E. D. Shirokoff, “The South Pole Telescope bolometer array and the measurement of secondary Cosmic Microwave Background anisotropy at small angular scales,” Ph.D. dissertation, University of California, Berkeley, Jan. 2011. <https://ui.adsabs.harvard.edu/#abs/2011PhDT.....383S>
- [208] L. Bleem, P. Ade, K. Aird *et al.*, “An Overview of the SPTpol Experiment,” *Journal of Low Temperature Physics*, vol. 167, pp. 859–864, Jun. 2012. <https://ui.adsabs.harvard.edu/#abs/2012JLTP..167..859B>
- [209] A. D. Turner, J. J. Bock, J. W. Beeman *et al.*, “Silicon nitride Micromesh Bolometer Array for Submillimeter Astrophysics,” *Appl. Optics*, vol. 40, pp. 4921–4932, Oct. 2001. <https://ui.adsabs.harvard.edu/#abs/2001ApOpt..40.4921T>
- [210] PICO website, “Q/U Pixel Layout for PICO.” https://sites.google.com/umn.edu/picomission/home/qu_pixels
- [211] A. D. Beyer, M. E. Kenyon, P. M. Echternach *et al.*, “Ultra-sensitive Transition-Edge Sensors for the Background Limited Infrared/Sub-mm Spectrograph (BLISS),” *Journal of Low Temperature Physics*, vol. 167, pp. 182–187, May 2012. <http://adsabs.harvard.edu/abs/2012JLTP..167..182B>
- [212] A. S. Rahlin, P. A. R. Ade, M. Amiri *et al.*, “Pre-flight integration and characterization of the SPIDER balloon-borne telescope,” in *Millimeter, Submillimeter, and Far-Infrared Detectors and Instrumentation for Astronomy VII*, vol. 9153, Jul. 2014, p. 915313. <https://ui.adsabs.harvard.edu/#abs/2014SPIE.9153E..13R>
- [213] S. W. Henderson, R. Allison, J. Austermann *et al.*, “Advanced ACTPol Cryogenic Detector Arrays and Readout,” *Journal of Low Temperature Physics*, vol. 184, pp. 772–779, Aug. 2016. <https://ui.adsabs.harvard.edu/#abs/2016JLTP..184..772H>
- [214] H. Hui, P. A. R. Ade, Z. Ahmed *et al.*, “BICEP Array: a multi-frequency degree-scale CMB polarimeter,”

- in *Society of Photo-Optical Instrumentation Engineers (SPIE) Conference Series*, vol. 10708, Jul. 2018, p. 1070807. <https://ui.adsabs.harvard.edu/#abs/2018SPIE10708E..07H>
- [215] M. C. Runyan, P. A. R. Ade, M. Amiri *et al.*, “Design and performance of the SPIDER instrument,” in *Millimeter, Submillimeter, and Far-Infrared Detectors and Instrumentation for Astronomy V*, vol. 7741, Jul. 2010, p. 77411O. <https://ui.adsabs.harvard.edu/#abs/2010SPIE.7741E..10R>
- [216] Z. D. Kermish, “The POLARBEAR Experiment: Design and Characterization,” Ph.D. dissertation, University of California, Berkeley, 2012. <http://adsabs.harvard.edu/abs/2012PhDT.....145K>
- [217] EBEX Collaboration, A. M. Aboobaker, P. Ade *et al.*, “The EBEX Balloon-borne Experiment: Optics, Receiver, and Polarimetry,” *The Astrophysical Journal Supplement Series*, vol. 239, p. 7, Nov. 2018. <https://ui.adsabs.harvard.edu/#abs/2018ApJS..239....7T>
- [218] BICEP2 Collaboration, P. A. R. Ade, R. W. Aikin *et al.*, “Detection of B-Mode Polarization at Degree Angular Scales by BICEP2,” *Phys. Rev. Lett.*, vol. 112, p. 241101, Jun. 2014. <https://ui.adsabs.harvard.edu/#abs/2014PhRvL.112x1101B>
- [219] F. Pajot, “Planck compression,” Private communication.
- [220] Planck HFI Core Team, P. A. R. Ade, N. Aghanim *et al.*, “Planck early results. IV. First assessment of the High Frequency Instrument in-flight performance,” *Astron. Astrophys.*, vol. 536, p. A4, Dec. 2011. <https://ui.adsabs.harvard.edu/#abs/2011A&A...536A...4P>
- [221] The EBEX Collaboration, A. Aboobaker, P. Ade *et al.*, “The EBEX Balloon-borne Experiment—Gondola, Attitude Control, and Control Software,” *The Astrophysical Journal Supplement Series*, vol. 239, p. 9, Nov. 2018. <https://ui.adsabs.harvard.edu/#abs/2018ApJS..239....9T>
- [222] M. Donabedian, A. I. of Aeronautics, and Astronautics, *Spacecraft Thermal Control Handbook, Vol. 2: Cryogenics*, ser. EngineeringPro collection. Aerospace Press, 2003. <https://books.google.com/books?id=nsLqjwEACAAJ>
- [223] R. G. Ross, “Estimation of thermal conduction loads for structural supports of cryogenic spacecraft assemblies,” *Cryogenics*, vol. 44, pp. 421–424, Jun. 2004. <https://ui.adsabs.harvard.edu/#abs/2004Cryo...44..421R>
- [224] M. Petach and M. Michaelian, “Mid InfraRed Instrument (MIRI) cooler cold head assembly acceptance testing and characterization,” *Cryocoolers*, vol. 18, p. 11, 2014. <https://cryocooler.org.wildapricot.org/resources/Documents/C18/002.pdf>
- [225] P. J. Shirron, M. O. Kimball, D. J. Fixsen, A. J. Kogut, X. Li, and M. J. DiPirro, “Design of the PIXIE adiabatic demagnetization refrigerators,” *Cryogenics*, vol. 52, pp. 140–144, Apr. 2012. <https://ui.adsabs.harvard.edu/#abs/2012Cryo...52..140S>
- [226] P. J. Shirron, M. O. Kimball, B. L. James *et al.*, “Thermodynamic performance of the 3-stage ADR for the Astro-H Soft-X-ray Spectrometer instrument,” *Cryogenics*, vol. 74, pp. 24–30, Mar. 2016. <https://ui.adsabs.harvard.edu/#abs/2016Cryo...74...24S>
- [227] J. Rabb et al, “Ngas scw-4k,” Presentation at the 2013 Space Cryogenics Workshop, 2013.
- [228] D. Durand, R. Colbert, C. Jaco, M. Michaelian, T. Nguyen, M. Petach, and J. Raab, “Mid Infrared Instrument (miri) Cooler Subsystem Prototype Demonstration,” in *Advances in Cryogenic Engineering*, ser. American Institute of Physics Conference Series, J. G. Weisend, J. Barclay, S. Breon *et al.*, Eds., vol. 52, Mar. 2008, pp. 807–814. <https://ui.adsabs.harvard.edu/#abs/2008AIPC..985..807D>
- [229] D. S. Glaister, W. Gully, R. Ross, P. Hendershott, E. Marquardt, and V. Kotsubo, “Ball Aerospace 4-6 K Space Cryocooler,” in *Advances in Cryogenic Engineering: Transactions of the Cryogenic Engineering Conference*, ser. American Institute of Physics Conference Series, I. Weisend, J. G., J. Barclay, S. Breon *et al.*, Eds., vol. 823, Apr. 2006, pp. 632–639. <https://ui.adsabs.harvard.edu/#abs/2006AIPC..823..632G>
- [230] F. Pajot, P. A. R. Ade, J. L. Beney *et al.*, “Planck pre-launch status: HFI ground calibration,” *Astron. Astrophys.*, vol. 520, p. A10, Sep. 2010. <https://ui.adsabs.harvard.edu/#abs/2010A&A...520A..10P>
- [231] C. L. Bennett, M. Bay, M. Halpern *et al.*, “The Microwave Anisotropy Probe Mission,” *Ap. J.*, vol. 583, pp. 1–23, Jan. 2003. <https://ui.adsabs.harvard.edu/#abs/2003ApJ...583....1B>
- [232] J. A. Tauber, N. Mandolcsi, J. L. Puget *et al.*, “Planck pre-launch status: The Planck mission,” *Astron. Astrophys.*, vol. 520, p. A1, Sep. 2010. <https://ui.adsabs.harvard.edu/#abs/2010A&A...520A...1T>
- [233] Space Exploration Technologies Corp., *Falcon 9 Launch Vehicle: Payload User’s Guide, Rev 2*. Space Exploration Technologies Corp., October 2015. https://www.spacex.com/sites/spacex/files/falcon_9_users_guide_rev_2.0.pdf

- [234] W. Hu, M. M. Hedman, and M. Zaldarriaga, “Benchmark parameters for CMB polarization experiments,” *Phys. Rev. D.*, vol. 67, p. 043004, Feb. 2003. <https://ui.adsabs.harvard.edu/#abs/2003PhRvD..67d3004H>
- [235] H. Kurki-Suonio, E. Keihänen, R. Keskitalo, T. Poutanen, A. S. Sirviö, D. Maino, and C. Burigana, “Destriping CMB temperature and polarization maps,” *Astron. Astrophys.*, vol. 506, pp. 1511–1539, Nov. 2009. <https://ui.adsabs.harvard.edu/#abs/2009A&A...506.1511K>
- [236] Deep Space Network, Jet Propulsion Laboratory, California Institute of Technology, “Deep space network services catalog 820-100, rev. f.” February 2015. <https://deepspace.jpl.nasa.gov/files/820-100-F1.pdf>
- [237] Planck Collaboration, R. Adam, P. A. R. Ade *et al.*, “Planck 2015 results. I. Overview of products and scientific results,” *Astron. Astrophys.*, vol. 594, p. A1, Sep. 2016. <https://ui.adsabs.harvard.edu/#abs/2016A&A...594A...1P>
- [238] D. Dutcher, P. A. R. Ade, Z. Ahmed *et al.*, “Characterization and performance of the second-year SPT-3G focal plane,” in *Society of Photo-Optical Instrumentation Engineers (SPIE) Conference Series*, vol. 10708, Jul. 2018, p. 107081Z. <https://ui.adsabs.harvard.edu/#abs/2018SPIE10708E..1ZD>
- [239] The Simons Observatory Collaboration, P. Ade, J. Aguirre *et al.*, “The Simons Observatory: Science goals and forecasts,” *arXiv e-prints*, Aug. 2018. <https://ui.adsabs.harvard.edu/#abs/2018arXiv180807445T>
- [240] H. Hui, P. A. R. Ade, Z. Ahmed *et al.*, “BICEP Array: a multi-frequency degree-scale CMB polarimeter,” in *Millimeter, Submillimeter, and Far-Infrared Detectors and Instrumentation for Astronomy IX*, ser. Society of Photo-Optical Instrumentation Engineers (SPIE) Conference Series, vol. 10708, Jul. 2018, p. 1070807. <http://adsabs.harvard.edu/abs/2018SPIE10708E..07H>
- [241] B. A. Benson, P. A. R. Ade, Z. Ahmed *et al.*, “SPT-3G: a next-generation cosmic microwave background polarization experiment on the South Pole telescope,” in *Society of Photo-Optical Instrumentation Engineers (SPIE) Conference Series*, ser. Society of Photo-Optical Instrumentation Engineers (SPIE) Conference Series, vol. 9153, Jul. 2014, p. 1. <http://adsabs.harvard.edu/abs/2014SPIE.9153E..1PB>
- [242] Y. Li, J. E. Austermann, J. A. Beall *et al.*, “Performance of the advanced ACTPol low frequency array,” in *Society of Photo-Optical Instrumentation Engineers (SPIE) Conference Series*, vol. 10708, Jul. 2018, p. 107080A. <https://ui.adsabs.harvard.edu/#abs/2018SPIE10708E..0AL>
- [243] BICEP2 and Keck Array Collaborations, P. A. R. Ade, Z. Ahmed *et al.*, “BICEP2 / Keck Array X: Constraints on Primordial Gravitational Waves using Planck, WMAP, and New BICEP2/Keck Observations through the 2015 Season,” *arXiv e-prints*, Oct. 2018. <http://adsabs.harvard.edu/abs/2018arXiv181005216A>
- [244] B. Westbrook, A. Cukierman, A. Lee, A. Suzuki, C. Raum, and W. Holzapfel, “Development of the Next Generation of Multi-chroic Antenna-Coupled Transition Edge Sensor Detectors for CMB Polarimetry,” *Journal of Low Temperature Physics*, vol. 184, pp. 74–81, Jul. 2016. <https://ui.adsabs.harvard.edu/#abs/2016JLTP..184...74W>
- [245] S. M. Simon, J. E. Golec, A. Ali *et al.*, “Feedhorn development and scalability for Simons Observatory and beyond,” in *Society of Photo-Optical Instrumentation Engineers (SPIE) Conference Series*, vol. 10708, Jul. 2018, p. 107084B. <https://ui.adsabs.harvard.edu/#abs/2018SPIE10708E..4BS>
- [246] R. O’Brient, J. Edwards, K. Arnold *et al.*, “Sinuous antennas for cosmic microwave background polarimetry,” in *Society of Photo-Optical Instrumentation Engineers (SPIE) Conference Series*, ser. Presented at the Society of Photo-Optical Instrumentation Engineers (SPIE) Conference, vol. 7020, Aug. 2008. <http://adsabs.harvard.edu/abs/2008SPIE.7020E..37O>
- [247] PICO website, “Study on wobble impact for component separation for the LiteBIRD collaboration.” https://sites.google.com/umn.edu/picomission/home/wobble_errard
- [248] J. G. Staguhn, D. J. Benford, C. A. Allen *et al.*, “GISMO: a 2-millimeter bolometer camera for the IRAM 30 m telescope,” in *Society of Photo-Optical Instrumentation Engineers (SPIE) Conference Series*, vol. 6275, Jun. 2006, p. 62751D. <https://ui.adsabs.harvard.edu/#abs/2006SPIE.6275E..1DS>
- [249] M. Ferlet, G. Laurent, B. Swinyard, J. Glenn, J. Bock, and K. Dohlen, “Characterisation of Herschel-SPIRE flight model optical performances,” in *Space Telescopes and Instrumentation 2008: Optical, Infrared, and Millimeter*, ser. Society of Photo-Optical Instrumentation Engineers (SPIE) Conference Series, vol. 7010, Jul. 2008, p. 70102U. <https://ui.adsabs.harvard.edu/#abs/2008SPIE.7010E..2UF>
- [250] J. T. Sayre, P. Ade, K. A. Aird *et al.*, “Design and characterization of 90 GHz feedhorn-coupled TES polarimeter pixels in the SPTPol camera,” in *Millimeter, Submillimeter, and Far-Infrared Detectors and Instrumentation for Astronomy VI*, vol. 8452, Sep. 2012, p. 845239. <https://ui.adsabs.harvard.edu/#abs/2012SPIE.8452E..39S>

- [251] R. Gualtieri, J. P. Filippini, P. A. R. Ade *et al.*, “SPIDER: CMB Polarimetry from the Edge of Space,” *Journal of Low Temperature Physics*, vol. 193, pp. 1112–1121, Dec. 2018. <http://adsabs.harvard.edu/abs/2018JLTP..193.1112G>
- [252] J. P. Filippini et al, in preparation, 2019.
- [253] W. S. Holland, D. Bintley, E. L. Chapin *et al.*, “SCUBA-2: the 10 000 pixel bolometer camera on the James Clerk Maxwell Telescope,” *MNRAS*, vol. 430, pp. 2513–2533, Apr. 2013. <https://ui.adsabs.harvard.edu/#abs/2013MNRAS.430.2513H>
- [254] W. B. Doriese, K. M. Morgan, D. A. Bennett *et al.*, “Developments in Time-Division Multiplexing of X-ray Transition-Edge Sensors,” *Journal of Low Temperature Physics*, vol. 184, pp. 389–395, Jul. 2016. <https://ui.adsabs.harvard.edu/#abs/2016JLTP..184..389D>
- [255] B. Dober, D. T. Becker, D. A. Bennett *et al.*, “Microwave SQUID multiplexer demonstration for cosmic microwave background imagers,” *Applied Physics Letters*, vol. 111, p. 243510, Dec. 2017. <https://ui.adsabs.harvard.edu/#abs/2017ApPhL.111x3510D>
- [256] K. D. Irwin and K. W. Lehnert, “Microwave SQUID multiplexer,” *Applied Physics Letters*, vol. 85, p. 2107, Sep. 2004. <https://ui.adsabs.harvard.edu/#abs/2004ApPhL..85.2107I>
- [257] H. McCarrick, G. Jones, B. R. Johnson *et al.*, “Design and performance of dual-polarization lumped-element kinetic inductance detectors for millimeter-wave polarimetry,” *Astron. Astrophys.*, vol. 610, p. A45, Feb. 2018. <http://adsabs.harvard.edu/abs/2018A%26A...610A..45M>
- [258] B. A. Steinbach, J. J. Bock, H. T. Nguyen, R. C. O’Brient, and A. D. Turner, “Thermal Kinetic Inductance Detectors for Ground-Based Millimeter-Wave Cosmology,” *Journal of Low Temperature Physics*, vol. 193, pp. 88–95, Nov. 2018. <https://ui.adsabs.harvard.edu/#abs/2018JLTP..193..88S>
- [259] B. R. Johnson, D. Flanigan, M. H. Abitbol *et al.*, “Development of Multi-chroic MKIDs for Next-Generation CMB Polarization Studies,” *Journal of Low Temperature Physics*, vol. 193, pp. 103–112, Nov. 2018. <http://adsabs.harvard.edu/abs/2018JLTP..193..103J>
- [260] P. Gloesener, “Large Aluminium Convex Mirror for the Cryo-Optical Test of the Planck Primary Reflector,” in *ESA Special Publication*, vol. 621, Jun. 2006, p. 43. <https://ui.adsabs.harvard.edu/#abs/2006ESASP.621E..43G>
- [261] Y. Toulemont, T. Passvogel, G. Pillbrat, D. de Chambure, D. Pierot, and D. Castel, “The 3.5m all SiC telescope for Herschel,” in *5th International Conference on Space Optics*, B. Warmbein, Ed., vol. 554, Jun. 2004, pp. 341–348. <https://ui.adsabs.harvard.edu/#abs/2004ESASP.554..341T>
- [262] Planck Collaboration, P. A. R. Ade, N. Aghanim *et al.*, “Planck early results. II. The thermal performance of Planck,” *Astron. Astrophys.*, vol. 536, p. A2, Dec. 2011. <https://ui.adsabs.harvard.edu/#abs/2011A&A...536A...2P>
- [263] S. Bard, “Development of a High-Performance Cryogenic Radiator with V-Groove Radiation Shields,” *Journal of Spacecraft and Rockets*, vol. 24, pp. 193–197, May 1987. <https://ui.adsabs.harvard.edu/#abs/1987JSPrRo..24..193B>
- [264] European Space Agency, “Planck cooling system,” September 2009. <http://sci.esa.int/planck/45498-cooling-system/?fbid=longid=2123>
- [265] T. S. Brown, *A GNC Perspective of the Launch and Commissioning of NASA’s New SMAP (Soil Moisture Active Passive) Spacecraft*. American Institute of Aeronautics and Astronautics, 2018/11/19 2016. <https://doi.org/10.2514/6.2016-0479>
- [266] L. E. Z. Jasper and P. Xaypraseuth, “Data production on past and future nasa missions,” in *2017 IEEE Aerospace Conference*, March 2017, pp. 1–11. <https://doi.org/10.1109/AERO.2017.7943918>
- [267] J. Mrozinski and M. DiNicola, “NICM: Cryocooler,” NASA 2017 Cost Symposium Presentations, August 2017. https://www.nasa.gov/offices/ocfo/cost_symposium/2017_presentations
- [268] H. P. Stahl and T. Henrichs, “Multivariable parametric cost model for space and ground telescopes,” in *Modeling, Systems Engineering, and Project Management for Astronomy VI*, ser. Society of Photo-Optical Instrumentation Engineers (SPIE) Conference Series, vol. 9911, Sep. 2016, p. 99110L. <https://ui.adsabs.harvard.edu/#abs/2016SPIE.9911E..0LS>